

POLITECNICO DI MILANO
Facoltà di Ingegneria Industriale
Dipartimento di Scienze e Tecnologie Aerospaziali
Laurea Magistrale in Ingegneria Spaziale



**A multidisciplinary tool for the combined
optimization of manned atmospheric entry
vehicles and their trajectory**

Relatore: Prof. Michèle Lavagna

Co-relatori: Prof. Kenneth D. Mease

Prof. Lorenzo Casalino

Tesi di Laurea di:
Eleonora Marina Botta
Matr. 765365

Anno Accademico 2012 – 2013

*To my parents,
who have done the hardest job.*

Acknowledgements

I would like to thank Professor Lavagna for giving me the opportunity to conduct this project, for enabling a period of research abroad and, especially, for recommending this course of study years ago and instilling in me passion for space.

Special thanks to Professor Mease, who let me join the Flight Dynamics and Control Lab at the University of California, Irvine. I am grateful for his support from both the scientific and the human standpoint.

I am thankful to Professor Casalino, from Politecnico di Torino, for accepting to be my ASP thesis supervisor.

The assistance of Dr. Ebbesen of ETH Zürich was very helpful for solving some problems related to the application of the PSO algorithm.

I am also grateful to Elena and Lella, who assisted me with their design abilities, and to my brother, who helped me with diagrams and tolerated the kidnapping of his laptop.

Thanks to all the colleagues who have shared the fatigues of the study and the relax of the lunch breaks. I cannot forget the group of the Bachelor, with the card games, the tireless study sessions and the holidays to recover from the exam periods. Thanks to Piera, Anna, Lorenzo and the other friends of the Master, companions in the stress of the projects and the thesis. Thanks to Federico, Juhaina and Sophie who have made my stay at Supaero pleasant. Thanks to the colleagues from UCI, especially to Lluís, Alessandro, Navid and the two Erics for their suggestions and support. Finally, thanks to the PoliMi volleyball team, in particular to Sere, Maffe and Mary, for experiencing together a different way to live the Politecnico and for winning a lot.

Thanks to all the friends who care in so many ways. Special gratitude goes to Lella, for being always there; to Alida, Jack and Linda, for their friendship and the study sessions; to my volleyball team, for making me feel younger.

Thanks to Filippo, who put up with me when I was nervous and was there, behind a computer overseas, in my sleepless nights; thanks for supporting me and believing in me even when I don't.

Special thanks to all my family, that makes home a very nice place to live. The highest gratitude to my parents, for teaching me every day, for providing me with education and for standing next to me in the choices that take me far from them.

Sommario

I programmi spaziali prevedono missioni di esplorazione umana verso la Luna e Marte. Per atterrare su un pianeta e per tornare sulla Terra è necessario superare la fase di ingresso atmosferico, particolarmente critica per via degli elevati carichi termici, aerodinamici e strutturali a cui viene sottoposto un veicolo. La progettazione di un sistema per il rientro è generalmente complicata dalla necessità di rispettare vincoli eterogenei; la presenza di un equipaggio la rende ancora più delicata, aggiungendo limitazioni fisiologiche. Il presente lavoro di tesi si propone di realizzare uno strumento di analisi progettuale multidisciplinare che permetta di determinare soluzioni preliminari per la configurazione del sistema di ingresso e per la sua traiettoria, tenendo conto della presenza dell'uomo a bordo. L'approccio utilizzato è quello dell'ottimizzazione multidisciplinare di un sistema complesso sottoposto a dinamiche veloci, in cui la fattibilità della soluzione è garantita dal soddisfacimento di vincoli sulla traiettoria, la struttura, la propulsione, la protezione termica, la velocità di impatto al suolo e la fisiologia umana. Per fare ciò, le varie discipline inerenti al progetto sono modellate separatamente e organizzate in seguito in uno strumento integrato capace di restituire soluzioni di primo tentativo, ma che tengono conto simultaneamente delle diverse problematiche. Il metodo di ottimizzazione prescelto è il Particle Swarm Optimization, capace di trovare soluzioni ottime di sistemi fortemente non lineari. I risultati ottenuti dimostrano l'efficacia dello strumento concepito, permettendo l'analisi delle caratteristiche comuni alle soluzioni trovate e il loro confronto.

Abstract

Space programs foresee human exploration missions to the Moon and Mars. To land on a planet and to come back to the Earth it is necessary to overcome the atmospheric entry phase, which is particularly critical because of the high thermal, aerodynamic and structural loads applied to a vehicle. The design of a reentry system is generally complicated by the need to verify heterogeneous constraints; the presence of a crew makes the design even more delicate, adding physiological limitations. The objective of the present study is the realization of a tool for multidisciplinary design that allows to determine preliminary solutions for the entry system configuration and trajectory, taking into account the presence of man aboard. The various disciplines inherent to the project are separately modeled and later organized in an integrated tool able to identify first guess solutions that simultaneously consider the different problems. The adopted approach is the multidisciplinary optimization of a complex system subject to fast dynamics, for which the feasibility of the solution is guaranteed by the verification of a set of constraints on the trajectory, the structure, the propulsion, the thermal protection, the landing velocity and the human physiology. The chosen optimization method is the Particle Swarm Optimization, able to find optimum solutions for highly nonlinear problems. The obtained results demonstrate the validity of the conceived tool, enabling the comparison of the solutions and the analysis of their common characteristics.

Contents

1	Introduction	1
1.1	Objectives	2
1.2	Structure	3
2	State of the art	5
2.1	EDL vehicles and trajectories	5
2.2	Previous work on multidisciplinary design for space transportation systems	8
3	Space physiology and human factors	9
3.1	Atmosphere	10
3.2	Acceleration	10
3.2.1	Sustained linear accelerations	10
3.2.2	Transient linear accelerations	17
3.2.3	Sustained rotational velocities and accelerations	20
3.2.4	Transient rotational accelerations	21
3.3	Volume	21
3.4	Radiation	25
3.5	Temperature	27
3.6	Noise and vibration	27
4	Disciplinary Models	29
4.1	Dynamics	30
4.1.1	Forces acting on an entry vehicle	30
4.1.2	Equations of motion	31
4.1.3	Bank angle	33
4.1.4	EDL phases	35
4.2	Planetary environments	37
4.3	Vehicle geometry, volume and mass	40
4.3.1	Geometry	40
4.3.2	Volume	42

4.3.3	Mass	43
4.3.4	Launcher capabilities	44
4.4	Aerodynamics	45
4.5	Parachutes	46
4.6	Aerothermodynamics	49
4.7	TPS sizing	52
4.8	Propulsion system sizing	54
4.9	Structure sizing	56
4.9.1	Spacecraft's first natural frequency	57
4.9.2	Static and dynamic loads	58
4.9.3	Structure mass	61
5	Multidisciplinary Optimization	65
5.1	Introduction to MDO	65
5.2	MDO methods and tools	67
5.3	Problem formulation	68
5.4	Optimization architecture	68
5.4.1	Parameters and variables	69
5.4.2	Modules inputs and outputs	70
5.4.3	Objectives	76
5.4.4	Constraints	77
5.4.5	Complete architecture	79
5.5	Optimization methods	79
6	Simulations and results	87
6.1	Simulations	87
6.2	Results	90
6.2.1	Comparison of multiple optimizations	90
6.2.2	A complete optimization	99
6.3	Difficulties and achievements	108
7	Conclusions and future developments	119
7.1	Conclusions	119
7.2	Future developments	121

List of Figures

1.1	EDL fields of study.	4
2.1	Examples of winged vehicles.	6
2.2	Examples of blunt body vehicles.	7
3.1	Sustained linear acceleration limits.	13
3.2	Coordinate system used for the evaluation of the acceleration environment.	14
3.3	Approximation of sustained linear acceleration limits in +Gx direction.	15
3.4	Definition of the critical point.	18
3.5	Sustained rotational velocity limits.	21
3.6	Sherwood and Capps' curves.	24
3.7	Rudisill et al.'s curve.	24
4.1	Forces acting on the vehicle and reference frames.	31
4.2	Spherical coordinates to define the position and the velocity of the vehicle.	32
4.3	MPF altitude profile.	34
4.4	Bank angle.	34
4.5	Atmospheric density interpolation for the Earth.	38
4.6	Speed of sound interpolation for the Earth.	38
4.7	Temperature interpolation for the Earth.	39
4.8	Apollo CM geometry.	41
4.9	Tools used to create Mars Microprobe aerodynamic database.	45
4.10	Aerodynamic coefficients interpolation at $\alpha_{trim} = 160^\circ$	47
4.11	Drogue parachute box.	48
4.12	$f(V)$ interpolation for the Earth.	51
4.13	Propulsion subsystem mass in function of the total impulse.	55
5.1	Planetary environment code inputs and outputs.	72
5.2	Geometry code inputs and outputs.	72

5.3	Mass code inputs and outputs.	72
5.4	Dynamics code inputs and outputs.	73
5.5	Aerodynamics code inputs and outputs.	73
5.6	Drogue parachute code inputs and outputs.	74
5.7	Main parachute code inputs and outputs.	74
5.8	Aerothermodynamics code inputs and outputs.	74
5.9	TPS code inputs and outputs.	74
5.10	Propulsion code inputs and outputs.	75
5.11	Structure code inputs and outputs.	75
5.12	Physiology code inputs and outputs.	75
5.13	Design Structure Matrix for the framework.	76
5.14	Architecture of the software for the optimization of the EDL vehicle and its trajectory.	80
5.15	Schematization of the optimization process.	81
5.16	Visual interpretation of PSO algorithm.	84
5.17	Visual interpretation of PSO constraint handling methods.	85
6.1	Comparison of the objective value for different simulations.	91
6.2	Decomposition of the total mass for different simulations.	92
6.3	Decomposition of the total mass for the CEV.	92
6.4	Comparison of the trajectory for the optimum solutions.	95
6.5	Comparison of the flight path angle for the optimum solutions.	96
6.6	Comparison of the velocity for the optimum solutions.	97
6.7	Variation of the velocity with altitude for the optimum solutions.	98
6.8	Variation of latitude and longitude for the optimum solutions.	99
6.9	Variation of the heading angle for the optimum solutions.	99
6.10	Variation of the Mach number for the optimum solutions.	100
6.11	Variation of the total heat rate for the optimum solutions.	100
6.12	Comparison of the load factor for the optimum solutions.	101
6.13	Variation of acceleration for the optimum solutions.	101
6.14	Variation of the objective function with the number of gener- ations.	102
6.15	Distribution of the fitness function value in the swarm.	103
6.16	Distribution of the particles in the search space for V_1^i and R	104
6.17	Distribution of the particles in the search space for γ_1^i and σ	105
6.18	Distribution of the particles in the search space for h_2^i and h_4^i	106
6.19	Distribution of the particles in the search space for h_6^i and T	107
6.20	Distribution of the particles in the search space for m_s and m_{TPS}	108
6.21	Distribution of the particles in the search space for m_{p1} and m_{p2}	109

6.22	Distribution of the particles in the search space for m_{prop} .	110
6.23	Comparison of the trajectory when using decelerators and in free fall.	110
6.24	Comparison of the velocity when using decelerators and in free fall.	111
6.25	Variation of the altitude in time for the optimum solution.	112
6.26	Variation of the velocity in time for the optimum solution.	112
6.27	Variation of the flight path angle in time for the optimum solution.	113
6.28	Variation of the altitude in time for the optimum solution.	113
6.29	Variation of the velocity in time for the optimum solution.	114
6.30	Variation of the flight path angle in time for the optimum solution.	115
6.31	Variation of the velocity with altitude for the optimum solution.	115
6.32	Variation of the velocity with altitude for the optimum solution.	116
6.33	Acceleration profile for the optimum solution.	116
6.34	Acceleration in body axis.	117

List of Tables

3.1	Observed sustained linear acceleration regimes during various entry histories.	11
3.2	Coefficients for equation 3.3.	19
3.3	Dynamic response limits for equation 3.5	19
3.4	Human spaceflight data as of July 2006.	23
3.5	Quality factors for radiation.	26
3.6	NASA exposure limits for crewmembers on LEO missions (blood-forming organs).	26
4.1	Summary of triggering events and mass and force parameters for EDL phases from 1 to 6.	36
4.2	Speed of sound model coefficients for the Earth.	38
4.3	Temperature model coefficients for the Earth.	39
4.4	Planetary bulk, orbital and atmospheric parameters.	40
4.5	Apollo and Crew Exploration Vehicle (CEV) pressurized and Outer Mold Line (OML) volumes.	42
4.6	Apollo, Soyuz and CEV pressurized and net habitable volumes.	43
4.7	Launchers reference performance.	44
4.8	Typical drag coefficients.	47
4.9	Parachutes deployment constraints.	48
4.10	Convective heat rate constant for the Earth and Mars.	50
4.11	Radiative heat rate constants for the Earth and Mars.	51
4.12	$f(V)$ interpolation coefficients for the Earth.	51
4.13	Avcoat 5029-39 thermophysical properties.	53
4.14	Ariane 5 frequency requirements.	57
4.15	Ariane 5 load factors.	58
4.16	7075 Al properties.	62
4.17	Delta II load factors for a spacecraft of MPF's size.	62
5.1	Search space bounds for the design variables.	71
6.1	PSO settings for the performed simulations.	89

6.2	Computational time for the simulations.	90
6.3	Optimum solutions for different simulations.	93
6.4	Results of different simulations.	94

Chapter 1

Introduction

From the time of our birth, it is our instinct to explore.

To map the lands, we must explore.

To chart the seas, we must explore.

To make new discoveries, we must explore.

Neil Armstrong
Apollo 11 Commander

Human missions have been fundamental in space programs since the first launch of Vostok, in 1961, which made Gagarin the first man to journey into space. Past orbital manned programs also include the Soviet Voskhod and Soyuz, the American Mercury, Gemini, Apollo and Space Shuttle and the Chinese Shenzhou. Space stations allowed men and women to live and work in space for long periods: Salyut and Skylab in the Seventies and Eighties, Mir from the middle Eighties to 2001 and the International Space Station (ISS) from 1998 to present. In the last decades we have been developing technologies that allow man to live in space for months, but Apollo is the only true experience we have gained beyond Low Earth Orbits (LEO). Even though current budgets for space research are decreased in reason of governmental financial constraints, human exploration of space remains a primary objective. Robotic missions are extremely valuable for collecting information on distant celestial bodies, but exploration is not complete until human beings reach those targets. Even the most definite images or the most complete set of data cannot satisfy the pursue of knowledge of man, who needs to see, touch and examine in person. Moreover, manned missions contribute to unite nations in the porsue of knowledge, making space research an opportunity for international cooperation. In the future of space exploration man will return to the Moon, in prepara-

tion for expeditions to Mars and the asteroids [1] [2] [3]. In order to reach the surface of a planet or to come back to the Earth, it is necessary to descend through an atmosphere dissipating the energy that characterizes an orbiting object. The Entry Descent and Landing (EDL) phase is extremely critical, since it combines the effects of various events and presents many complications. The severe heating loads and accelerations deriving from the aerodynamic braking threaten the crew survival. Mistakes in the planning or in the operation of a planetary entry can lead to tragic events such as the well-known Space Shuttle Columbia accident on February 1, 2003 when seven astronauts died while re-entering the Earth's atmosphere, due to a failure in the heat shield in proximity of the wing's leading edge. An attentive study of the final phase of a mission is necessary to avoid loss of human lives, because entry vehicles undergo multiple critical events.

1.1 Objectives

The objective of the present work is the creation of an optimization tool that could help identifying good solutions for manned atmospheric EDL systems. A preliminary analysis, useful in the first stage of a project, requires an integrated tool that exploits simple but effective models of the various concurring disciplines, defines parameters and objectives and combines them in an optimization routine.

Many features are worth the attention of EDL system engineers who want to consider the couplings between configuration and trajectory, and among the different subsystems of the vehicle. The interesting fields of study inherent to the project of a space transportation system with human beings onboard are depicted in figure 1.1. As it is evident, the problem is intrinsically multidisciplinary and, for an accurate study, the design should consider all these components. The present work takes into account the fields of study highlighted in the scheme, with the aim of developing a preliminary design tool.

Given the multidisciplinary nature of reentry vehicles design, the adopted point of view will be global. The model will be sufficiently articulated to represent the complexity of the problem, but will include approximations that allow its inclusion in an optimization process. The optimal solutions will be researched with state-of-the-art global optimization algorithms and will represent first guess solutions for more accurate disciplinary designs.

The project's ambition is to overcome the lack of integrated tools for the preliminary design of vehicles and trajectories for manned missions. Fundamental in the framework of the project is that the presence of man is

considered since the very beginning of the preliminary design phase.

1.2 Structure

Chapter 2 reviews the vehicles and trajectories designed and used for atmospheric entries up to the time of writing. After the presentation of the typical configurations with their characteristics, the first high level choices are made. The chapter then deals with the state of the art in the simulation of EDL. The focus is on the integration of the multiple disciplines involved and on Multidisciplinary Optimization (MDO) tools.

Chapter 3 describes the complications deriving from the presence of human beings onboard an EDL vehicle, particularly examining atmospheric and volume requirements and acceleration physiology.

In chapter 4 the models used to simulate the descent of the vehicle are detailed. First, the dynamic equations are presented and the descent is divided in six phases. After approximating planetary atmospheres and gravity fields, the configuration is treated and the guidelines for the evaluation of the mass are given. Disciplines as aerodynamics and aerothermodynamics are then addressed, together with the sizing of the different subsystems: parachutes, TPS, propulsion, structure. For each model, the validation is shown.

Chapter 5 covers MDO in general and in the case at hand. After an introduction of the methods and tools for MDO, the general formulation of the optimization problem is presented. The variables of the problem are then selected and the objective and constraint functions are defined. The disciplinary modules are revised from an input-output point of view and the scheme of the complete optimization architecture is proposed. Finally, some global optimization methods are discussed.

Chapter 6 presents the performed simulations and analyzes the obtained results, verifying the validity of the conceived tool. Three levels of analysis are proposed: a comparison of multiple optimal solutions, the characteristics of a complete optimization process, the optimal solution of this simulation. Finally, the difficulties encountered in the search of the results are briefly discussed.

Chapter 7 concludes recalling the principal aspects of the present work, stressing its achievements and its limitations and proposing some future studies and investigations.

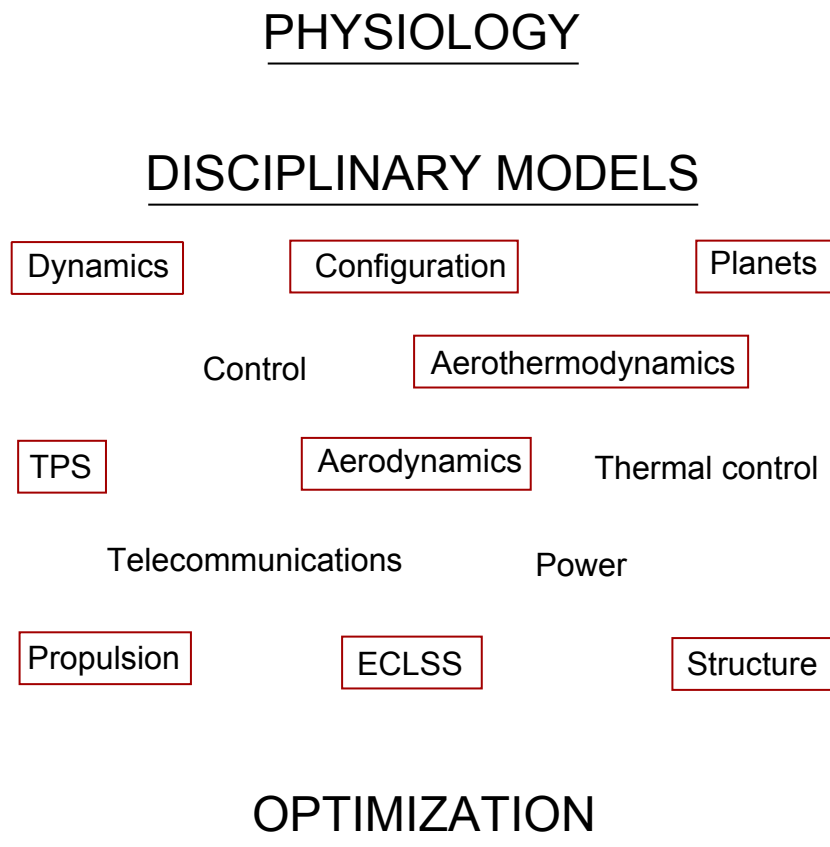


Figure 1.1: EDL fields of study.

Chapter 2

State of the art

Here I am at the turn of the millennium and I'm still the last man to have walked on the Moon, somewhat disappointing. It says more about what we have not done than about what we have done.

*Gene Cernan
Apollo 17 Commander*

Man has not returned beyond Low Earth Orbits since 1972, when the last man walked on the Moon. Forty years have passed and much of the competence that was acquired to bring the man to the Moon has gone lost. Robotic planetary missions have continued and travels to and from the ISS are regularly performed, but new interest has grown lately in the project of space vehicles for the transportation of human beings beyond LEO, helped by the Space Shuttle retirement. This section first presents the state of the art in planetary exploration and atmospheric entry vehicles. Second, it briefly reviews the literature on MDO studies for space transportation vehicles.

2.1 EDL vehicles and trajectories

Many different types of vehicles have been studied and used for atmospheric entry purposes. The two main categories for entry vehicle shapes are blunt bodies and lifting bodies. The principal difference between these groups of vehicles is their manoeuvrability, that is the ability to control the trajectory. This property depends on the vehicle's aerodynamic efficiency, which is indicated by the ratio L/D or C_L/C_D .

Lifting vehicles benefit from L/D ratios bigger than 1, which are provided by the significant aerodynamic surface of the wings and allow a good manoeuvrability. On the other hand, the presence of the wings' sharp leading edges and of control surfaces exacerbates the structural and thermal loads. The quintessential example of this type of vehicles is the NASA's Space Shuttle orbiter, which followed a gliding trajectory in the Earth's atmosphere, performing a lengthy and shallow hypersonic descent [4]. In the Eighties, the French Centre National d'Études Spatiales (CNES) and the European Space Agency (ESA) also began a study on a reusable lifting vehicle, called Hermes; nonetheless, due to the cost of the project and the low performance achieved, the program was cancelled [5]. More recent studies on winged gliders concepts include National Aeronautics and Space Administration (NASA)'s HL-20 [6] and X-38 [7]. Some winged vehicles used or just designed for space missions are displayed in figure 2.1.

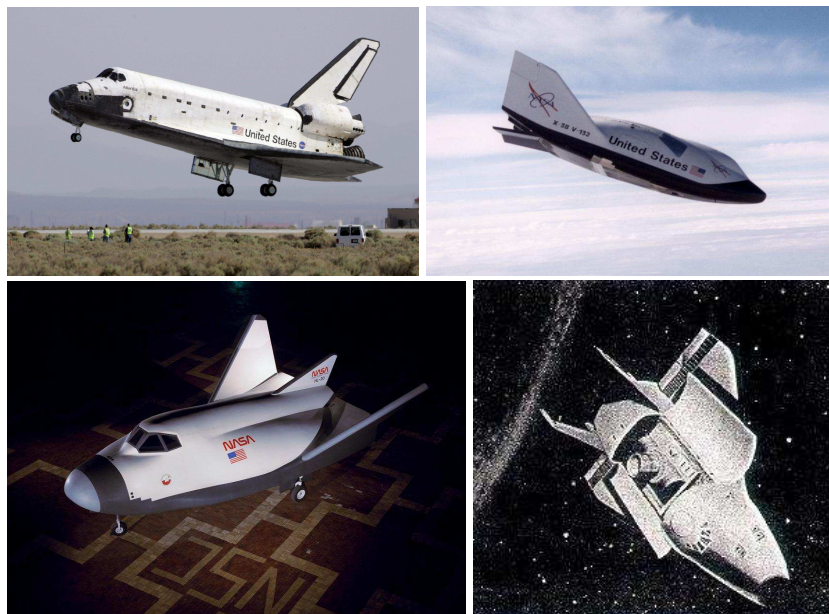


Figure 2.1: Examples of winged vehicles.

Vehicles belonging to the blunt body category do not present control surfaces; therefore, their ability to manoeuvre to control the descent is far more limited and their entry trajectory is almost ballistic. The only control during the descent is provided by a modulation of aerodynamic forces, obtained through attitude control. If a symmetric capsule flown at zero angle of attack follows a nominally ballistic trajectory, some lift can be produced by changing the attitude in order to gain some control over the trajectory. Typical values of the lift-to-drag ratio for this class of vehicles are lower than

0.5 [8]. Advantages of blunt body configurations are a better distribution of thermal and structural loads due to the absence of sharp edges and the efficient energy dissipation deriving from high drag coefficients. Blunt body shapes have been used for both manned vehicles and autonomous probes and include spheres, sphere-cones (spherical section forebody and blunted conical afterbody) and biconics (sphere-cone with additional frustum). The early manned Vostok and Voskhod capsules were spheric, as well as the Venera probes, which entered Venus atmosphere. Spere-cone examples are the Apollo Command Module (CM) and Viking, Huygens and Mars Exploration Rover (MER) planetary probes. Biconic geometries have been studied for years, but just some prototypes have been flown. Examples of blunt geometries used for space missions can be seen in figure 2.2.

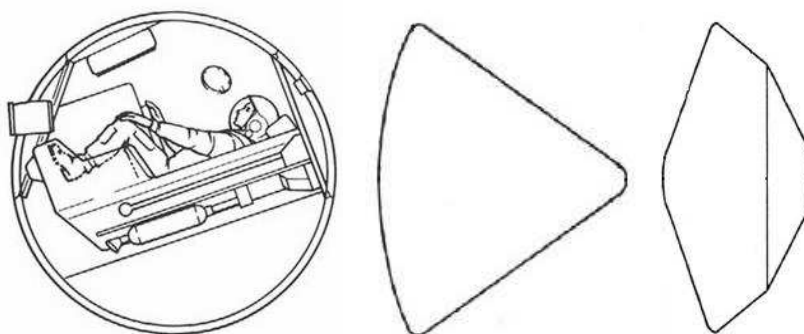


Figure 2.2: Examples of blunt body vehicles.

The present work explores the atmospheric entry of manned sphere-cone capsules. Among this class of vehicles, the choice was made of adopting the Apollo configuration, mainly because of data availability considerations; however, this class of vehicles is suitable to parametrized studies (as done by Samareh [9]). Winged vehicles are deliberately disregarded since the study of their trajectory would be completely different, in reason of their manoeuvrability capabilities, explained above. Skip trajectories, in which a vehicle enters the atmosphere, skips out and re-enters after performing some keplerian motion, are neglected too. This technique has never been used for manned entries, although it was studied within the Apollo program; lately, some studies for the CEV are evaluating this possibility for lunar return. In the light of the presented choices, the investigated descent in the atmosphere is controlled by modulation of the aerodynamic forces and is simply marked by a sequence of events, such as the deployment of a drogue and a main parachute, the release of the drogue parachute and of the heat shield and the firing of some retrorockets.

2.2 Previous work on multidisciplinary design for space transportation systems

Numerous studies have addressed the integration issues of the disciplines involved in EDL. NASA's Langley Research Center [10] and Ames Research Center [11] developed an integrated analysis environment exploiting a Web-based graphical user interface; their work replied to the need of sharing design information within a geographically dispersed team of discipline experts. Papadopoulos and Subrahmanyam [12] proposed another Web-based entry vehicle design framework focusing on aerothermodynamics. The Planetary Entry System Synthesis Tool (PESST) framework, developed at the Georgia Institute of Technology and described in references [13] and [14], exploited Matlab capabilities to integrate the modules for a wider spectrum of disciplines, including also some terminal guidance. Another multidisciplinary tool developed by NASA is SAPE [9], that relies on the object-oriented programming capabilities of Python to integrate some open-source softwares, can be operated cross-platform and performs low-fidelity system analysis. An optimization tool for the entry system configuration and the EDL trajectory of robotic probes in Martian atmosphere was formulated by Parigini [15]. Armellin et al. published a dual work on aero-gravity assist maneuvers [16]. A multidisciplinary optimization tool addressing the design of launchers was developed by Castellini and Lavagna [17]. Years before, the use of collaborative optimization as a MDO method for launcher design was envisaged by Braun et al. [18].

Chapter 3

Space physiology and human factors

They say any landing you can walk away from is a good one.

Alan Shepard
Apollo 14 Commander

The presence of humans aboard a vehicle profoundly influences its design. Crewmembers are precious operators who can construct, maintain and repair a vehicle and are able to sense situations of danger, make decision and implement solutions. On the other hand, it is of primary importance to guarantee their safety and avoid any threat to the crew survival and operational capability. The sizing of the subsystems and components for safety and the possibility to abort the mission are just examples of the impact that the crew presence has on the design. As Larson and Pranke emphasize, the implication of the presence of human beings must be taken into account as soon as possible in space systems design. This is necessary to avoid the manifestation of problems later in the process, which increases the overall cost of the design [19].

Human physiology in space is not fully understood yet. Bedrest studies have been used since the advent of human spaceflight to induce and study the effects of prolonged weightlessness [20]. In the effort to collect information to plan future lengthy manned missions, many studies are still ongoing at research institutions and space agencies [21] [22].

This section deals with the main physiological issues related to the presence of human beings aboard a vehicle for Entry Descent and Landing. Paramount environmental factors are atmosphere, radiation protection, temperature and

acceleration: the failure to comply with requirements on these environmental conditions jeopardizes the crew survival. Other conditions that may affect the crewmembers' performance are noise, vibration and illumination. For the scope of this work, only the environmental factors that relate to the CM and the trajectory design are considered.

3.1 Atmosphere

Thanks to the adaptability¹ of human body, many design options exist for the internal atmospheric pressure and composition. Internal total pressure must be kept between 14.7 and 3.6 *psia* for crew survival. Only at pressures higher than 7.3 *psia*, however, it is possible to dilute oxygen with some inert gas to reduce fire hazards; a 100% O_2 atmosphere is not acceptable for uses other than Extra-Vehicular Activities (EVAs) [23]. In this work, an internal pressure of 14.7 *psia* (Earth's surface atmospheric pressure, about 101300 *Pa*) is considered.

3.2 Acceleration

EDL acceleration environments are extremely challenging for human beings. During an atmospheric entry astronauts are subject to hypergravity conditions, rotations, parachute deployments and the impact with the planetary surface. Different accelerations cause different effects on the crewmembers, depending on their type, duration and direction. The purpose of this section is to give an idea of the main physiological constraints on planetary entry and to explain the model built for the project. Design considerations can be found in NASA's Human Integration Design Handbook (HIDH) [24], Space Flight Human System Standard (SFHSS) [25] and Man-Systems Integration Standards (MSIS) [23]; an extensive and precise source for human physiology in space is the joint U.S. and Russian publication [26].

3.2.1 Sustained linear accelerations

Sustained accelerations are defined as events with a duration of 0.5 seconds or more. Examples of typical sustained accelerations during entry are in table 3.1. Accelerations are usually expressed in multiples of the Earth's gravity magnitude g . The values in the table make it clear that the entry

¹Capacity to maintain a dynamic equilibrium of body conditions within a range of environmental changes.

Table 3.1: Observed sustained linear acceleration regimes during various entry histories.

Entry	Acceleration regimes [g]
Mercury	7.6 – 11.1
Gemini	4.3 – 7.7
Apollo	8
Shuttle	1.5

phase is characterized by high sustained linear accelerations, especially as far as capsules are concerned; shuttles undergo much lower maximum values but for a longer time.

A number of factors affect human tolerance to acceleration: magnitude, duration, direction and rate of onset and decline of the applied force; age, training, physical conditions and extent of microgravity adaptation of the crewmembers; type of seats, body restraints and body positioning; emotional and environmental conditions. The effects of acceleration on human physiology are more or less serious, depending on the particular combination of these conditions. Of primary concern is the possible occurrence of Gravity-induced Loss Of Consciousness (G-LOC), that hampers the ability to maneuver the vehicle if needed and jeopardizes the safety of the astronauts. Due to gravity, the body's blood is drawn towards the legs; if the body has adapted to 0g environments, the blood volume and the cardiovascular capacity are reduced: this can result in hypotension, leading to tunnel vision² or even the complete blackout. These problems are often combined with disorienting sensations (together with neusea and vertigo) when the subject moves his or her head in hypergravity. Adaptation to 0g environments also causes orthostatic intolerance during the return to gravity or in hypergravity conditions; most notably, this makes a rapid egress from the vehicle difficult. Injuries can also ensue from a particularly severe reentry, for example in case of a minor failure. All of the aforementioned threats should be taken into account when planning planetary entries, most importantly when designing interplanetary missions, which are likely to expose the crew to higher g-loads than the ones that are typical for orbital missions. A weak point in the evaluation of human tolerance to acceleration during interplanetary missions is the lack of data: the effects of adaptation to partial gravity (that may be experienced when on the Moon or Mars surface) on levels of tolerance are still obscure.

²Loss of peripheral vision, resulting in a constricted tunnel-like visual field.

Figure 3.1, built thanks to the data provided by the SFHSS[25], presents the requirements of NASA Standards on sustained linear acceleration exposure limits. The character G in the titles refers to the direction of the inertial resultant to whole body acceleration. For axes definition the reader should refer to the coordinate system in figure 3.2. The origin of the system of axes is in a body organ and will be assumed to be in the heart. The graphs point out how exposure limits vary in different directions and are higher in x-direction: the presence of the rib cage protects the internal organs from accelerations in the perpendicular direction better than from accelerations in the other two directions. Nonetheless, the curves show a similar decreasing trend with respect to acceleration duration. For example, it is possible to withstand an acceleration of $10g$ in $+G_x$ direction for 10 seconds, but the same acceleration would be fatal if it lasted 100 seconds.

Limits for nominal reentry are lower than those valid for launch or for abort and emergency entry. As stated before, exposure to reduced gravity degrades human physiological capabilities and exposes crewmembers to injuries and G-LOC even for relatively less severe deceleration profiles. During the launch crewmembers are not deconditioned and can withstand higher loads. During the extreme conditions of a launch abort or an emergency entry it may be necessary to accept higher accelerations to have the crew return on Earth alive; anyway, exceeding the depicted limits may result in the loss of the crew. It is worth noting that, in order to check that the experienced accelerations are within the tolerance limits, linear accelerations induced by rotations must be accounted for.

The constraints on maximum sustained linear accelerations are modeled separately for the different axes, deriving some analytical expression of the curves in figure 3.1. A straight line in a logarithmic graph can be approximated by a generic polynomial of the type:

$$y = n x^m \tag{3.1}$$

If t is the duration, in seconds, and a is the acceleration, in multiples of the Earth's gravity, the approximating equations for piecewise linear curves

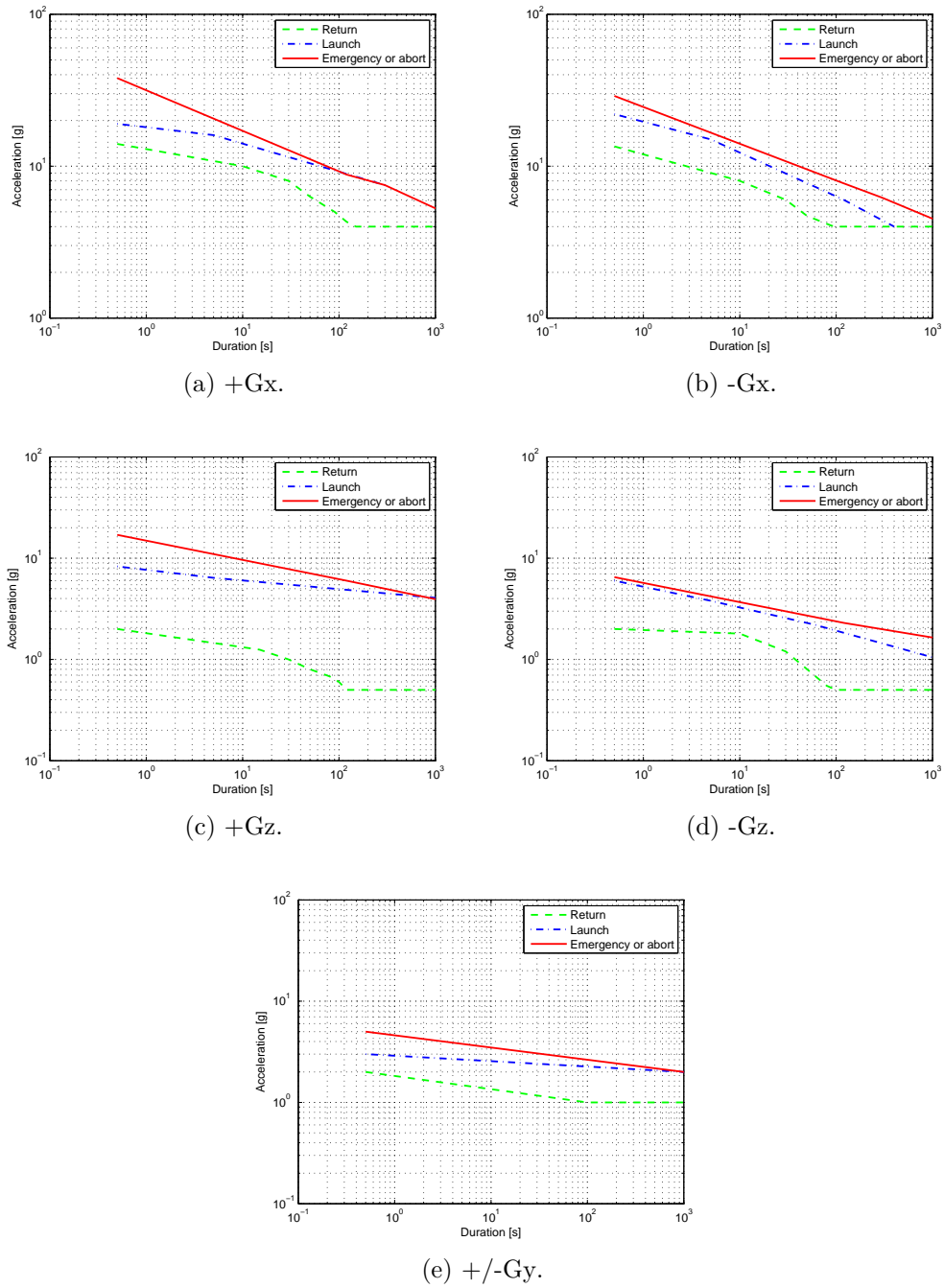


Figure 3.1: Sustained linear acceleration limits.

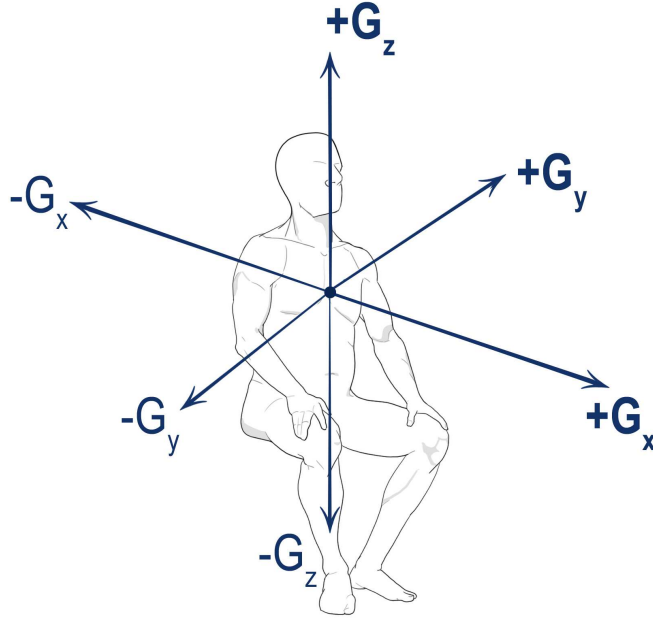


Figure 3.2: Coordinate system used for the evaluation of the acceleration environment.

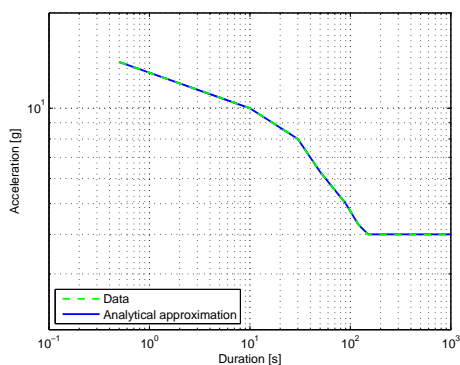
describing the upper limits in $+G_x$ direction are:

$$\text{For a nominal return: } a = \begin{cases} 12.9514 t^{(-0.1123)}, & \text{if } 0.5 \leq t \leq 10, \\ 15.963 t^{(-0.2031)}, & \text{if } 10 \leq t \leq 30, \\ 39.2535 t^{(-0.4677)}, & \text{if } 30 \leq t \leq 50, \\ 29.3331 t^{(-0.3932)}, & \text{if } 50 \leq t \leq 90, \\ 52.9078 t^{(-0.5243)}, & \text{if } 90 \leq t \leq 120, \\ 20.2922 t^{(-0.3241)}, & \text{if } 120 \leq t \leq 150, \\ 4, & \text{if } 150 \leq t \leq 10000. \end{cases}$$

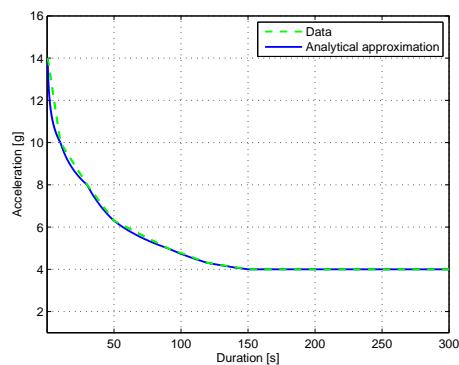
$$\text{For an emergency return: } a = \begin{cases} 31.5817 t^{(-0.2669)}, & \text{if } 0.5 \leq t \leq 120, \\ 20.2862 t^{(-0.1745)}, & \text{if } 120 \leq t \leq 300, \\ 39.7716 t^{(-0.2925)}, & \text{if } 300 \leq t \leq 1200. \end{cases}$$

By drawing on the same plot the data from tables and the approximating

functions, as in figure 3.3, it is possible to compare the curves. On a logarithmic graph the approximating functions overlies on the curves from the data; on a simple plot the extremes coincide and the other points are lower than the ones from the data. This suggests that an approximation of this type is conservative, therefore acceptable.



(a) Logarithmic plot.



(b) Normal plot.

Figure 3.3: Approximation of sustained linear acceleration limits in +G_x direction.

For sake of completeness, the approximating curves for the limits in the other directions are reported below.

In $-G_x$ direction:

$$\text{For a nominal return: } a = \begin{cases} 11.9606 t^{(-0.1747)}, & \text{if } 0.5 \leq t \leq 10, \\ 14.6201 t^{(-0.2619)}, & \text{if } 10 \leq t \leq 30, \\ 30.4986 t^{(-0.478)}, & \text{if } 30 \leq t \leq 50, \\ 12.657 t^{(-0.2532)}, & \text{if } 50 \leq t \leq 90, \\ 6.8845 t^{(-0.1179)}, & \text{if } 90 \leq t \leq 100, \\ 4, & \text{if } 100 \leq t \leq 10000. \end{cases}$$

$$\text{For an emergency return: } a = \begin{cases} 24.5223 t^{(-0.242)}, & \text{if } 0.5 \leq t \leq 120, \\ 23.8861 t^{(-0.2365)}, & \text{if } 120 \leq t \leq 300, \\ 27.9426 t^{(-0.264)}, & \text{if } 300 \leq t \leq 1200. \end{cases}$$

In $+G_z$ direction:

$$\text{For a nominal return: } a = \begin{cases} 1.8173 t^{(-0.1382)}, & \text{if } 0.5 \leq t \leq 15, \\ 2.989 t^{(-0.3219)}, & \text{if } 15 \leq t \leq 30, \\ 4.4182 t^{(-0.4368)}, & \text{if } 30 \leq t \leq 50, \\ 3.0943 t^{(-0.3458)}, & \text{if } 50 \leq t \leq 80, \\ 7.9427 t^{(-0.5609)}, & \text{if } 80 \leq t \leq 100, \\ 60 t^{(-1)}, & \text{if } 100 \leq t \leq 120, \\ 0.5, & \text{if } 120 \leq t \leq 10000. \end{cases}$$

$$\text{For an emergency return: } a = \begin{cases} 14.902 t^{(-0.19)}, & \text{if } 0.5 \leq t \leq 120, \\ 15.5093 t^{(-0.1984)}, & \text{if } 120 \leq t \leq 1200. \end{cases}$$

In $-G_z$ direction:

$$\text{For a nominal return: } a = \begin{cases} 1.9518 t^{(-0.0352)}, & \text{if } 0.5 \leq t \leq 10, \\ 4.2106 t^{(-0.3691)}, & \text{if } 10 \leq t \leq 30, \\ 17.85 t^{(-0.7937)}, & \text{if } 30 \leq t \leq 50, \\ 18.0939 t^{(-0.7972)}, & \text{if } 50 \leq t \leq 80, \\ 3.5745 t^{(-0.4271)}, & \text{if } 80 \leq t \leq 100, \\ 0.5, & \text{if } 100 \leq t \leq 10000. \end{cases}$$

$$\text{For an emergency return: } a = \begin{cases} 5.6997 t^{(-0.1896)}, & \text{if } 0.5 \leq t \leq 120, \\ 4.8913 t^{(-0.1576)}, & \text{if } 120 \leq t \leq 1200. \end{cases}$$

In $+G_y$ and $-G_y$ direction:

$$\text{For a nominal return: } a = \begin{cases} 1.8266 t^{(-0.1308)}, & \text{if } 0.5 \leq t \leq 100, \\ 1, & \text{if } 100 \leq t \leq 10000. \end{cases}$$

$$\text{For an emergency return: } a = 4.5992 t^{(-0.1206)}, \text{ if } 0.5 \leq t \leq 1000.$$

To make sure that the crew can survive the planetary entry, the experienced acceleration profile for each direction should always be lower than the maximum acceleration limits as modeled above.

An additional consideration is on the admissible rate of change of linear sustained acceleration: to minimize the risk of incapacitation of the crew,

this value should not exceed 500 g/s .
 This constraint is simply modeled as:

$$\frac{a(t_{i+1}) - a(t_i)}{t_{i+1} - t_i} \leq 500 \quad (3.2)$$

where a is the acceleration in g in a given body direction at t_1 and t_2 are time instants, in seconds.

3.2.2 Transient linear accelerations

Impact accelerations are abrupt onset, short duration and high magnitude acceleration or deceleration events. By definition, transient is any acceleration that lasts less than 0.5 seconds. Typical examples of events that cause transient accelerations during an EDL phase are flight instabilities, air turbulence, parachute openings and crash landings. These events are likely to cause very high accelerations for short times; for example, crash landings generate decelerations from 10 to more than 100 g and parachute deployments cause decelerations of approximately 10 g .

Effects of impacts are commonly measured in terms of skeletal injury occurrences. The most common type of fracture deriving from shocks is to the vertebrae, followed by damage to the head. Tolerance to this type of physical stress is determined by the magnitude of the acceleration, together with the time of exposure and the orientation of the human body. Accelerations whose vector is perpendicular to the spinal axis, passing through the chest, are more easily tolerated also in this case. Moreover, as for sustained accelerations, tolerance diminishes with the deconditioning deriving from 0g adaptation: fractures are more probable, since muscles and bones are seriously reduced in strength.

Injury risk assessment is usually performed with the Brinkley Dynamic Response Model, that provides estimates on physical damage probability for a given acceleration-time history. This model was built on experimental data, adjusted to take into account the physical deconditioning related to prolonged exposure to microgravity, and is validated for accelerations shorter than 0.5 seconds and crewmembers who are restrained (with at least torso and pelvic restraints and anti-submarining restraints) and seated in cushions or seat padding that preclude amplification of the acceleration transmitted to the body. In the following, the method is reviewed and the implemented model is presented.

The Brinkley Dynamic Response Model, formulated by Brinkley et al. [27] and detailed in reference [24], is used to compute the maximum allowable impact accelerations at the body critical point, which corresponds more or less to the midthoracic center of mass. If we use a coordinate system centered in the seat, as in figure 3.4 (source: [24]), the coordinates of the critical point are approximately ³:

$$\begin{aligned}x &= 8.6 \text{ cm} \\y &= 0 \\z &= 46.2 \text{ cm}\end{aligned}$$

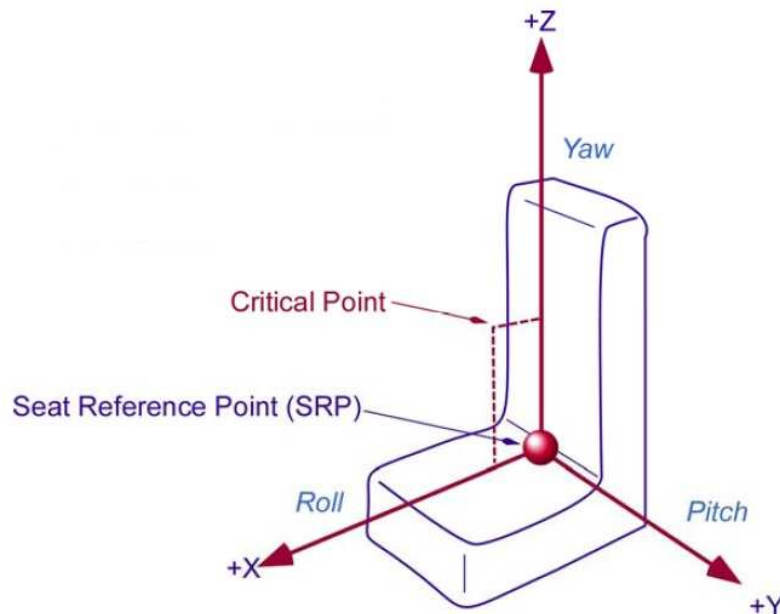


Figure 3.4: Definition of the critical point.

The model assumes that the total mass acting on the vertebrae and causing deformation can be represented by a single mass, so that the dynamic response to a solicitation for each axis is:

$$\ddot{x} + 2\xi\omega_n\dot{x} + \omega_n^2x = A \quad (3.3)$$

where A is the acceleration of the seat at the critical point, for each axis, taking into account the linear components due to angular motion; x , \dot{x} and

³Originally in inches: $x = 3.4 \text{ in}$, $y = 0$, $z = 18.2 \text{ in}$

Table 3.2: Coefficients for equation 3.3.

	$x > 0$	$x < 0$	$y > 0$	$y < 0$	$z > 0$	$z < 0$
ω_n	62.8	60.8	58	58	52.9	47.1
ξ	0.20	0.04	0.09	0.09	0.224	0.24

Table 3.3: Dynamic response limits for equation 3.5

DR level	$DR_x > 0$	$DR_x < 0$	$DR_y > 0$	$DR_y < 0$	$DR_z > 0$	$DR_z < 0$
Low, deconditioned	35	-28	14	-14	13	-11.5
Low, non deconditioned	35	-28	14	-14	15.2	-13.5
Medium, deconditioned	40	-35	17	-17	15.4	-14.1
Medium, non deconditioned	40	-35	17	-17	18	-16.5
High, deconditioned	46	-46	22	-22	19.5	-17.5
High, non deconditioned	46	-46	22	-22	22.8	-20.4

\ddot{x} are, respectively, the subject's displacement, relative velocity and inertial acceleration with respect to the critical point; ξ and ω_n are the damping coefficient ratio and the undamped natural frequency, reported in table 3.2.

Once the acceleration is known, the displacement of the occupant's body can be found by integrating equation 3.3. This allows the computation of the dimensionless dynamic response for each axis, DR , defined as:

$$DR = \omega_n^2(x/g) \quad (3.4)$$

where g is the gravity acceleration. Finally, the injury risk criterion, β is computed as:

$$\beta = \sqrt{\left(\frac{DR_x(t)}{DR_x^{lim}}\right)^2 + \left(\frac{DR_y(t)}{DR_y^{lim}}\right)^2 + \left(\frac{DR_z(t)}{DR_z^{lim}}\right)^2} \quad (3.5)$$

where DR_x^{lim} , DR_y^{lim} and DR_z^{lim} are the dynamic response limits reported in table 3.3.

The maximum allowable β value is 1; nonetheless, the objective is to achieve lower values, for the *low, deconditioned* level of the dynamic response

limits. This provides a margin of safety for healthy deconditioned crewmembers.

A consideration must be made on the crew positioning inside the vessel: since impact accelerations through the chest are better tolerated, it is preferable to have the crewmembers land and experience parachute deployments while on their back.

3.2.3 Sustained rotational velocities and accelerations

Some level of rotation is inevitable during spacecraft atmospheric entry. Typically, angular velocities exceed $360^\circ/s$ and angular accelerations are more severe than $10^\circ/s^2$ [24]. Human tolerance to rotation is, once again, limited and variable according to duration, center of rotation with respect to the body and axis of rotation. Effects range from disorientation to nausea, headache and numbness in the legs; random tumbles and high rotation rates degrade reach and manipulative abilities, thus interfering with the maneuvering performance of the crewmembers, and may lead to unconsciousness.

Suggested limits for angular velocity are depicted in figure 3.5, built with data provided by the SFHSS [25]. These restrictions apply for any axis and for any center of rotation; as already said in paragraph 3.2.1, the linear accelerations generated at the heart by angular velocities and accelerations centered outside the heart must be included in the linear accelerations evaluation. As for the linear case, limits for reentry are the lowest since the crewmembers are deconditioned by their travel in space. Limits for launch are somewhat higher, while abort or emergency entries may require exposure to very severe conditions. In any case should rotational acceleration exceed this upper limit, as this would seriously threaten the crew's survival.

Indicating duration with t , in seconds, and rotational velocity with ω , in *rpm*, the following are the analytical expressions used to approximate the piecewise linear curves for nominal and emergency return:

$$\text{For a nominal return: } \omega = \begin{cases} 37.5 t^{(-0.3258)}, & \text{if } 0.5 \leq t \leq 1, \\ 37.5 t^{(-0.3237)}, & \text{if } 1 \leq t \leq 700. \end{cases}$$

$$\text{For an emergency return: } \omega = \begin{cases} 120 t^{(-0.1043)}, & \text{if } 0.5 \leq t \leq 1, \\ 120 t^{(-0.1058)}, & \text{if } 1 \leq t \leq 700. \end{cases}$$

According to NASA's Standards, sustained rotational accelerations (whose duration is greater than 0.5 seconds) should never be greater than $115^\circ/s^2$ in yaw, pitch or roll, to avoid incapacitating discomfort and disorientation.

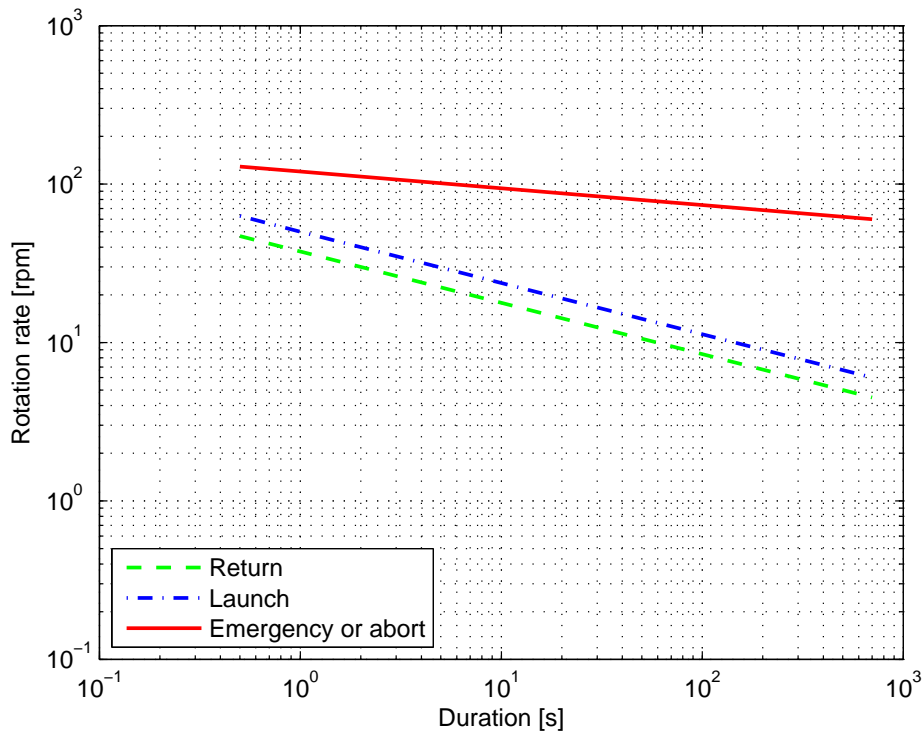


Figure 3.5: Sustained rotational velocity limits.

3.2.4 Transient rotational accelerations

With respect to the $115^\circ/s^2$ limit for sustained rotational acceleration, much higher levels may be tolerable for very short exposures; for example, some studies indicate that $10000 \text{ rad}/s^2$ can be withstood for less than 10 ms . Anyway, no theory comparable to Brinkley's model exists for transient rotational accelerations; NASA proposes the use of a $1800^\circ/s^2$ limit [25].

3.3 Volume

To ensure that the crewmembers can perform their tasks in an efficient, effective and, most importantly, safe way, the design must provide sufficient habitable volume. The minimum acceptable volume generally depends on several factors, among which:

- crew size;
- physical dimensions of the crewmembers' bodies;
- mission duration;
- mission tasks;
- gravitational environment.

First of all, the design of a habitable module must accommodate the expected crew size for a certain mission: a larger crew necessitates of increased room for itself and the collateral resources (hygiene, living and sleeping capabilities). In the same way, it must comfortably house the smallest and largest crewmember, suited or unsuited as dictated by the mission profile. The psychological and physical stress of a space mission typically increases with its duration, because of confinement and isolation of the crew; the main consequence is the crew's urgency for increased habitable volume. Mission tasks influence the required volume in reason of the movements that the astronauts perform to accomplish their duties. Finally, body postures and movements to perform a certain task are different for each orientation and gravity condition of the vehicle.

In the framework of this project, only the crew size and mission duration dependencies were considered. In fact, during a planetary atmospheric entry the crewmembers are seated and restrained and their tasks are very limited. Crewmembers physical dimensions are mostly influent on the design of the seats and restraints, which are indeed customized for better protection, but these aspects are outside the purpose of the current study. Finally, according to the HIDH [24], given a ceiling that accommodates stature, the required volume in 1g and 0g conditions is roughly equivalent and the dependency on mission duration is likely to be similar in any gravitational environment.

The HIDH presents two methods to define the required Net Habitable Volume (NHV) early in the project. A first possibility is to analyze the combination of tasks to be performed during the mission, but this method was judged too time-consuming for the aim of the present study; moreover, the tasks of the crew during the EDL phase are limited and require little movements. The alternative approach for the required NHV evaluation is based on previous experience in space crew transportation. The HIDH suggests the use of the following relation, derived from an undersea habitat habitable volume study:

$$NHV \text{ per crewmember} = 6.67 \ln(T_{mission}) - 7.79 \quad (3.6)$$

Table 3.4: Human spaceflight data as of July 2006.

Spacecraft type	Category	Mission duration [days]	Volume per crew [m^3]	Crew [-]
Mecury	Capsule	0.02 – 1.43	1.70	1
Gemini	Capsule	0.21 – 14	1.28	1 – 2
Apollo CM	Capsule	6 – 12.75	2.22 – 4.27	3
Apollo LM	Capsule	1 – 3.21	3.33	2
Apollo-Soyuz	Capsule	9.04	3.33	5
Vostok	Capsule	1.04 – 5	5.73	1
Voskhok	Capsule	1 – 1.08	1.91 – 2.87	2 – 3
Soyuz	Capsule	0.43 – 14	1.28	2
Shenzhou	Capsule	1 – 5	8.50 – 17	1 – 2
Space Shuttle	Shuttle	2.25 – 17.67	8.94 – 35.75	2 – 8
Shuttle-Spacelab	Shuttle	4 – 16.9	14.66 – 42.7	5 – 8
Skylab	Station	28 – 84	120.33	3
Skalyut	Station	16 – 237	33.5 – 55.25	2 – 3
Mir	Station	72.82 – 437.75	45 – 181.35	2 – 3
ISS	Station	128.86 – 195.82	85.17 – 201.13	2 – 3

The NHV per crewmember, in m^3 , shows a logarithmic dependence on the duration, expressed in days. The fact that this relation gives negative volumes for short durations, however, prevents its use for the present investigation.

A comprehensive survey on regression curves for the spacecraft volume dependence on mission duration was made by Cohen [28]. The summary of the human spaceflight data that were collected for Cohen’s study is partially reported in table 3.4. Although the critical volumetric quantity in the design of crew transportation vehicles is the NHV, regressions on historical data are typically performed considering pressurized volumes. Among the studies on the subject, the author judged it was useful to recall Sherwood and Capps’ curves (in figure 3.6 [28]), which distinguish entry capsules from the other habitable vehicles, such as space stations and Shuttles. The authors’ explanation for this distinction was double: astronauts do not need to have a lot of room when they endure a few hours-trip; moreover, atmospheric entry vehicles geometry, dictated by heating constraints, has a bad packaging efficiency. Rudisill et al. identified two mission type categories as well: *transportation-like* and *station-like* spacecrafts. They explained that this is reasonable since the functions served by the vehicles are profoundly different. The result of their study is in figure 3.7 [29].

No analytical relation was found in the literature for these curves, so it was derived with the same approximation used for the acceleration limits. If

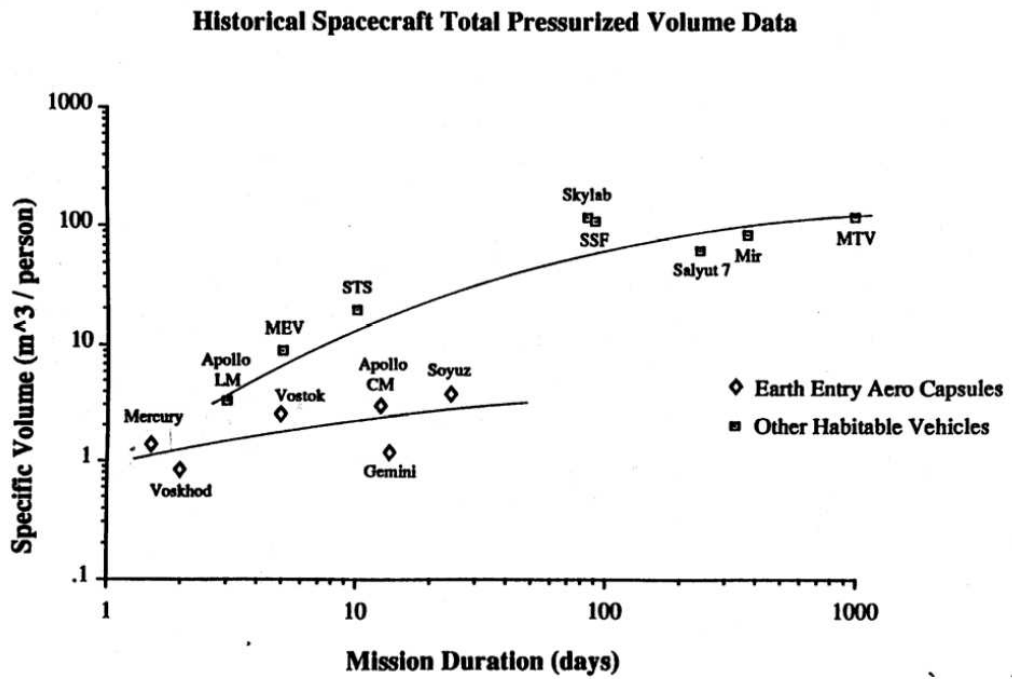


Figure 3.6: Sherwood and Capps' curves.

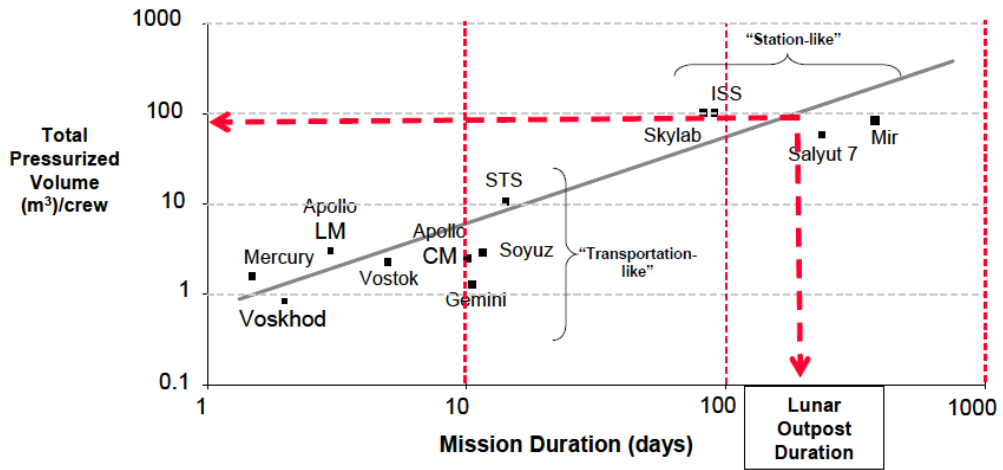


Figure 3.7: Rudisill et al.'s curve.

$T_{mission}$ is the duration of the mission in *days*, the pressurized volume per crewmember in m^3 follows more or less the relation:

$$V_p \text{ per crewmember} = 1.12 (T_{mission})^{0.25} \tag{3.7}$$

The total required pressurized volume is just computed by multiplying the volume per capita for the expected number of crewmembers N_{crew} :

$$V_p = (V_p \text{ per crewmember}) * N_{crew} \quad (3.8)$$

3.4 Radiation

The radiation environment in space entails high immediate and delayed risks. Outside the atmosphere and magnetosphere, no protection from radiation exists other than space vehicles and space suits; crewmembers are exposed to important radiation amounts, especially if they perform interplanetary space flights. Ionizing radiation, coming from Galactic Cosmic Rays (GCRs), Solar Particle Events (SPEs) and trapped belt radiation, is particularly dangerous for humans' health. Late effects, manifested months or years after exposure, range from DNA damage and cancer induction to impairment of fertility. Early effects include nausea, insomnia, headache, altered motor and cognitive abilities, behavioural changes and even death [30]. Even though any tissue and organ is threatened by radiation, of highest concern is the Central Nervous System (CNS), for which damage to small groups of cells can lead to irreversible physiological effects [31].

Radiation coming from different sources (GCRs, radiation belts, SPEs) entails various effects on the organism. The biological effect for any kind of radiation can be compared on a common scale by defining the *dose equivalent*, measured in Sieverts (Sv). This quantity is found by weighting the absorbed dose with a quality factor Q . The *absorbed dose* is the amount of energy per unit mass deposited by ionizing particles, measured in Grays (Gy); the quality factors account for the Relative Biological Effectiveness (RBE) of radiations and are shown in table 3.5 [19].

The effects of radiation exposure vary with sex, age and health conditions; exposure limits also vary according to these parameters. Maximum allowable doses were defined by NASA according to risk-based evaluations: astronauts were considered as workers with occupational hazards and the acceptable risk was set to be comparable to that of other *less-safe* but common occupations (3% augmentation in risk of cancer mortality). Table 3.6 shows the limits for radiation in LEO missions to blood-forming organs (source: [30]).

To contain the threats to the astronauts' CNS and organs, a certain level of radiation protection is needed. The doses encountered during long-duration interplanetary missions are likely to be above the guidelines in table 3.6 (see reference [31] for evaluations of the expected equivalent doses). To minimize the risk during remote missions it will be necessary to make a revision of the maximum dose limits and a dedicated study of radioprotection

Table 3.5: Quality factors for radiation.

Radiation type	Q [-]
x-rays and γ -rays	1
β particles, electrons	1
α particles, 1 MeV	20
α particles, 5 MeV	15
Heavy nuclei	20
Neutrons, thermal to 10 keV	2 – 3
Neutrons, 20 keV	5
Neutrons, 0.1 MeV to 20 MeV	7 – 11
Protons, 0.1 MeV	10
Protons, 1 MeV	8.5
Protons, > 100 MeV	1 – 2

Table 3.6: NASA exposure limits for crewmembers on LEO missions (blood-forming organs).

Exposure period	Maximum allowable dose [<i>Sv</i>]
30 days	0.25
1 year	0.5
Career, from age 25	1.5 (Male) 1.0 (Female)
Career, from age 35	2.5 (Male) 1.75 (Female)
Career, from age 45	3.2 (Male) 2.5 (Female)
Career, from age 55	4.0 (Male) 3.0 (Female)

through the combination of shielding, chemicals, onboard measurements and maybe therapies. For the moment, the author feels she does not have sufficient information to size the radiation shielding of the transportation vehicle.

3.5 Temperature

Internal temperature must be maintained in a quite limited range for the whole duration of the mission, to ensure both comfort and a safe body core temperature. For example, the temperature in the ISS is kept between 18.3 and 26.7°C with a tolerance of $\pm 4^\circ\text{C}$ [32]. This is controlled by the Environmental Control and Life Support System (ECLSS), which also provides waste management, water and food supplies, fire detection and suppression, atmospheric pressure. During a planetary entry, the control of temperature is particularly challenging; in addition to the protection of the heat shield, the astronauts wear special suits that include heat removal devices as the Liquid Cooling Garment (LCG), a fluid circulating loop providing conductive cooling [33]. The sizing of the ECLSS is not considered at the time of writing.

3.6 Noise and vibration

Noise must be limited during a manned mission in order to improve comfort, ease communication and protect hearing. Vibration must be controlled to avoid long durations, high amplitudes and frequencies that are resonant with body systems. These factors are very important for space stations, but are not considered in this project since they scarcely relate to the preliminary design of entry vehicles. If the concept consists in a CM that transports the crew in the final phase of a planetary mission only, these requirements are neglected in the first analysis; the Service Module (SM) determines the noise and vibration environment and provides the Environmental Control and Life Support (ECLS) for most of the mission.

Chapter 4

Disciplinary Models

Coming down under a parachute is quite different as well. You hit the ground pretty hard, but all the systems work very well to keep it from hurting, so it doesn't even hurt when you hit.

Leroy Chiao
Expedition 10 Commander

In space systems design, many disciplines interact and are strictly interdependent. This chapter describes the components of the model that was created to simulate the reentry trajectory and the vehicle during its descent. First, the dynamics of EDL is detailed, introducing the forces acting on a vehicle and some convenient reference frames, reporting the equations of motion, defining the bank angle and dividing the descent into phases. After that, the chapter presents the models employed to simulate the atmosphere of a planet and its gravitational field. The vehicle's geometry, volume and mass are then addressed, together with a short dissertation on launchers capabilities. The method employed to derive the aerodynamic coefficients for the capsule is explained and justified, followed by the definition of the parachutes deployment conditions and the estimation of their mass. After the assessment of the convective and radiative heat loads experienced during the descent, the Thermal Protection System (TPS) mass is evaluated. Finally, the propulsion capability of the retrorockets and the primary structure are sized. During the construction of the model, the different disciplinary tools were validated against mission experience, historical data and results of published works; every section shows how the validation was performed.

4.1 Dynamics

4.1.1 Forces acting on an entry vehicle

To study the dynamics of a body travelling in a planetary atmosphere, it is important to define the forces acting on the vehicle. In fact, the translational motion of an object's center of mass is defined by the Newton's second law of motion:

$$m \mathbf{a} = \sum_{k=1}^n \mathbf{F}_k \quad (4.1)$$

where m is the mass of the vehicle, \mathbf{a} is the acceleration vector and \mathbf{F}_k are the external forces acting on the vehicle. In the case of an unpowered entry, the forces acting on a body in an atmosphere are the gravitational force \mathbf{W} and the aerodynamic force \mathbf{A} :

$$\mathbf{W} = m \mathbf{g} \quad (4.2a)$$

$$\mathbf{A} = \mathbf{D} + \mathbf{L} \quad (4.2b)$$

Equation 4.2b indicates the conventional decomposition of the aerodynamic force in drag and lift. Drag is the component opposed to the velocity vector, while lift is the component perpendicular to it. Figure 4.1 shows these forces in different vehicle-centered reference frames, for which the origin is in the center of mass of the vehicle.

- The local horizon reference frame $\{\mathbf{x}^h, \mathbf{y}^h, \mathbf{z}^h\}$ is such that the $\mathbf{x}^h, \mathbf{y}^h$ plane is tangent to the planetary surface and \mathbf{z}^h is toward the center of the planet.
- The body axes $\{\mathbf{x}^b, \mathbf{y}^b, \mathbf{z}^b\}$ are defined as the longitudinal axis (or roll axis), the lateral axis (or pitch axis) and the normal axis (or yaw axis). For an axisymmetric capsule only the longitudinal axis is uniquely defined; the other two can be chosen as it is more convenient. A good choice for vehicles carrying humans is to position the crew so that the G_x axis is coincident to \mathbf{x}^b and to take \mathbf{z}^b so that it corresponds to the G_z direction; \mathbf{y}^b completes the orthonormal triad and is parallel to the G_y direction. G_x , G_y and G_z were defined in figure 3.2.
- The wind reference frame $\{\mathbf{x}^w, \mathbf{y}^w, \mathbf{z}^w\}$ is such that the \mathbf{x}^w axis is aligned to the relative velocity vector and \mathbf{z}^w lies in the $\mathbf{x}^b, \mathbf{z}^b$ plane, forming an acute angle with \mathbf{z}^b .

Some angles define the rotations between these three reference frames. The angle of attack α is the angle between the relative velocity vector direction \mathbf{x}^w and the longitudinal axis of the vehicle \mathbf{x}^b . The flight path angle γ is the angle between the relative velocity vector and the local horizontal plane $\mathbf{x}^h, \mathbf{y}^h$, positive when the velocity is above this plane. The representation in figure 4.1 is valid if the sideslip angle, the angle between the velocity vector and the $\mathbf{x}^b, \mathbf{z}^b$ plane, is null.

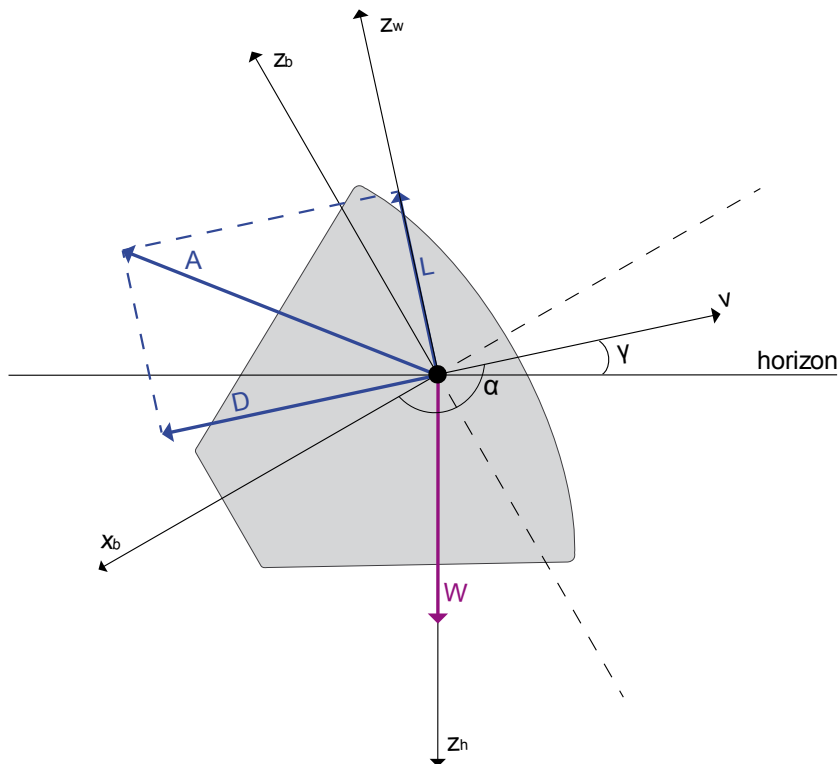


Figure 4.1: Forces acting on the vehicle and reference frames.

4.1.2 Equations of motion

The equations of motion of a vehicle flying inside an atmosphere over a spherical rotating planet were derived by Vinh [34]. If the vehicle is considered to be a point mass, the equations of motion referred to a planet-fixed

coordinate frame are:

$$\dot{R} = V \sin \gamma \quad (4.3a)$$

$$\dot{\varphi} = \frac{V}{R} \cos \gamma \sin \psi \quad (4.3b)$$

$$\dot{\theta} = \frac{V \cos \gamma \cos \psi}{R \cos \varphi} \quad (4.3c)$$

$$\dot{V} = -\frac{D}{m} - g \sin \gamma \quad (4.3d)$$

$$\dot{\gamma} = \frac{L}{mV} \cos \sigma - \frac{g}{V} \cos \gamma + \frac{V}{R} \cos \gamma + C_\gamma \quad (4.3e)$$

$$\dot{\psi} = -\frac{L \sin \sigma}{mV \cos \gamma} - \frac{V}{R} \cos \gamma \cos \psi \tan \varphi + C_\psi \quad (4.3f)$$

where m is the vehicle's mass, R is the radial distance from the center of the planet to the vehicle's center of mass, φ is the latitude, θ is the longitude, V is the vehicle's relative velocity, γ is the flight path angle defined in the previous section and ψ is the heading angle (measured from the East direction). Figure 4.2 represents the coordinates used for the description of the dynamics (source: [15]). σ is the bank angle, while L and D are the

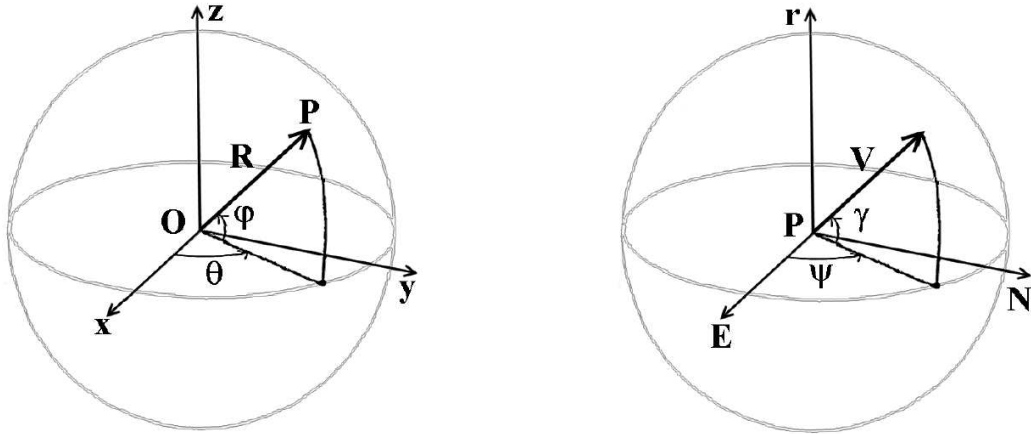


Figure 4.2: Spherical coordinates to define the position and the velocity of the vehicle.

well-known lift and drag forces:

$$L = \frac{1}{2} \rho V^2 S C_L \quad (4.4a)$$

$$D = \frac{1}{2} \rho V^2 S C_D \quad (4.4b)$$

where S is a reference surface, ρ is the atmospheric density and the coefficients C_L and C_D depend on the shape of the vehicle, the Mach number and the attitude.

C_γ and C_ψ are related to the angular velocity of the planet ω_{pl} . They both contain a term proportional to ω_{pl} and a term proportional to ω_{pl}^2 ; in general the rotational velocity of planetary bodies is small and higher order terms can be neglected. Only the Coriolis acceleration component in ω_{pl} survives and C_γ and C_ψ can be approximated as:

$$C_\gamma = 2\omega_{pl} \cos \psi \cos \varphi \quad (4.5a)$$

$$C_\psi = 2\omega_{pl}(\tan \gamma \sin \psi \cos \varphi - \sin \varphi) \quad (4.5b)$$

In order to make the state variables comparable and ease the numerical solution of the equations of motion, it is convenient to derive a non-dimensional system of equations. A suitable change of variables is given by Parigini [15], who suggests to replace R and V with:

$$r = \frac{R}{R_{pl}} \quad (4.6a)$$

$$v = \frac{V}{\sqrt{g_0 R_{pl}}} \quad (4.6b)$$

The point-mass dynamics is therefore described by a set of six state variables:

$$y = \{r \quad \varphi \quad \theta \quad v \quad \gamma \quad \psi\} \quad (4.7)$$

Validation of the equations of motion was obtained by comparing some flight data about Mars Pathfinder (MPF) entry system to the results of the numerical integration. Initial conditions at the entry, vehicle properties and time profiles of some state variables for MPF were collected by Spencer et al. [35]. In figure 4.3 the squares represent the flight data, while the dashed line is obtained with the numerical integration of our equations of motion. The flight data do not always coincide with the numerical integration altitude profile. This difference could be expected and is acceptable when comparing preliminary nominal profiles with flight data.

4.1.3 Bank angle

The bank angle is the angle between the local vertical and the lift vector, as defined in figure 4.4 (positive when it generates a right turn). During the descent, it can be kept fixed or follow a time-varying profile. In any case, it

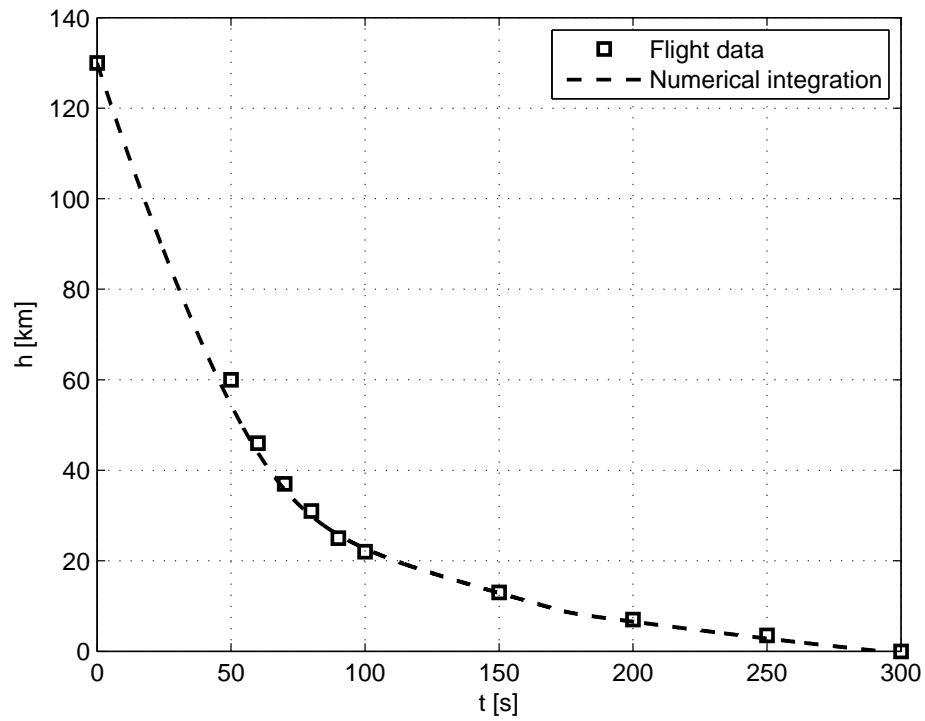


Figure 4.3: MPF altitude profile.

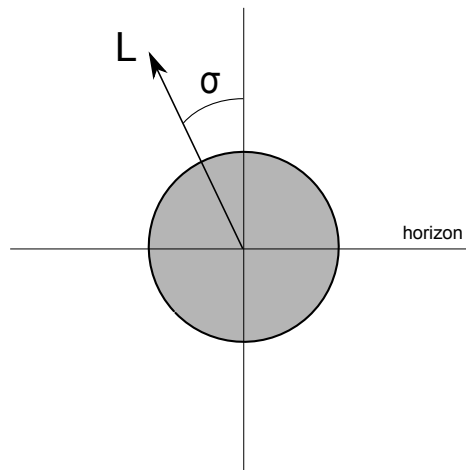


Figure 4.4: Bank angle.

must be kept between -90° and 90° .

If a time-varying bank angle profile is adopted, the capsule must be able

to rotate to modify its attitude in a controlled way. This is possible thanks to the small thrusters of the Reaction Control System (RCS). The rate and acceleration of the bank angle are limited by the RCS capabilities:

$$|\dot{\sigma}| \leq \dot{\sigma}_{max} \quad (4.8)$$

$$|\ddot{\sigma}| \leq \ddot{\sigma}_{max} \quad (4.9)$$

At the time of writing, the bank angle is kept fixed throughout the whole descent.


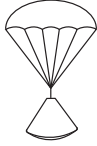

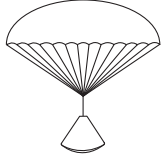
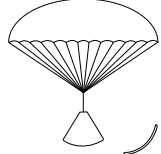

4.1.4 EDL phases

The Entry Descent and Landing of the reentry vehicle is modeled by a sequence of six phases. Each phase is characterized by a different configuration and is initiated and ended by the occurrence of an event:

- Phase 1: the capsule enters the atmosphere and begins dissipating energy through friction;
- Phase 2: the drogue parachute is deployed and the capsule is slowed down by its additional drag;
- Phase 3: the drogue parachute is released and the capsule keeps falling alone;
- Phase 4: the main parachute is deployed and slows down the capsule in its descent;
- Phase 5: when heat rates are low enough, the heat shield is jettisoned, exposing the retrorockets;
- Phase 6: the retrorockets are fired soon before the touchdown.

The simplest way to model this sequential trajectory consists in the consecutive integration of the same set of differential equations 4.3 for any phase. Two parameters only change from a phase to the following one: the vehicle mass, which decreases instantaneously after any component release, and the drag, which increases instantaneously when parachutes are open or retrorockets are fired. Table 4.1 summarizes the triggering events and the mass and force parameters for each phase of the descent. m_{TOT} represents the total mass at entry, m_{P1} and m_{P2} the mass of the drogue and main parachutes respectively and m_{hs} the heat shield mass; D_c is the drag of the capsule, D_{P1} and D_{P2} the drag due to the drogue and main parachutes and T_r the thrust of the retrorockets, which is assumed to be in the direction of motion.

Table 4.1: Summary of triggering events and mass and force parameters for EDL phases from 1 to 6.

Phase 1		
Beginning	Entry	
End	Drogue parachute deployment	
Mass	m_{TOT}	
Force in v-direction	D_c	
Phase 2		
Beginning	Drogue parachute deployment	
End	Drogue parachute release	
Mass	m_{TOT}	
Force in v-direction	$D_c + D_{P1}$	
Phase 3		
Beginning	Drogue parachute release	
End	Main parachute deployment	
Mass	$m_{TOT} - m_{P1}$	
Force in v-direction	D_c	
Phase 4		
Beginning	Main parachute deployment	
End	Heat shield jettisoning	
Mass	$m_{TOT} - m_{P1}$	
Force in v-direction	$D_c + D_{P2}$	
Phase 5		
Beginning	Heat shield jettisoning	
End	Retrorockets ignition	
Mass	$m_{TOT} - m_{P1} - m_{hs}$	
Force in v-direction	$D_c + D_{P2}$	
Phase 6		
Beginning	Retrorockets ignition	
End	Touchdown	
Mass	$m_{TOT} - m_{P1} - m_{hs}$	
Force in v-direction	$D_c + T_r$	

4.2 Planetary environments

Having in mind that the aim of the project is to perform a preliminary optimization of a reentry vehicle and its trajectory, without making computational effort heavier than strictly needed, planetary atmospheres and gravity fields are modeled in the simplest possible way. Atmospheric composition only matters in the definition of stagnation-point convective heat rate (see paragraph 4.6) and is not treated here.

One of the most important features of the atmosphere in EDL dynamics is density. Great simplification is obtained assuming that atmospheric density decreases exponentially with altitude:

$$\rho = \rho_0 e^{-\frac{h}{H}} \quad (4.10)$$

where ρ_0 is the atmospheric density at the planetary surface, h is the altitude and H is the density scale height. As it is evident in figure 4.5 for the Earth, this approximation is good in the whole range of altitudes.

The Mach number is a fundamental quantity for aerodynamic considerations. It is defined as:

$$Ma = \frac{V}{a_0} \quad (4.11)$$

where V is the local flight speed and a_0 is the local speed of sound. In order to determine the Mach number, an evaluation of the local speed of sound is needed. This is obtained by interpolating the values in reference [36] with a polynomial function of altitude:

$$a_0 = \alpha_m h^m + \alpha_{m-1} h^{m-1} + \dots + \alpha_1 h + \alpha_0 \quad (4.12)$$

The experimental speed of sound profile for the Earth and its polynomial fit are shown in figure 4.6.

Atmospheric pressure is evaluated with the perfect gas law:

$$p = \frac{\rho R_0 T}{M} \quad (4.13)$$

where M is the molar mass of the gas, considered constant during the descent, R_0 is the universal gas constant, ρ is the atmospheric density and T is the

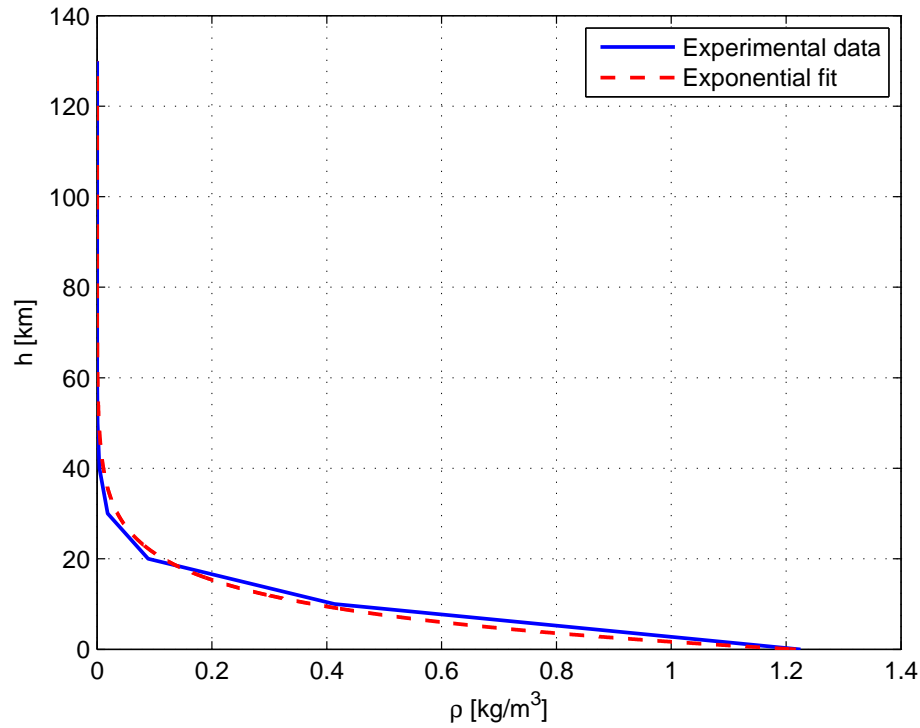


Figure 4.5: Atmospheric density interpolation for the Earth.

Coefficient	Value
α_5	-1.7231×10^{-22}
α_4	6.6573×10^{-17}
α_3	-8.7159×10^{-12}
α_2	4.6202×10^{-7}
α_1	-0.0090437
α_0	348.2

Table 4.2: Speed of sound model coefficients for the Earth.

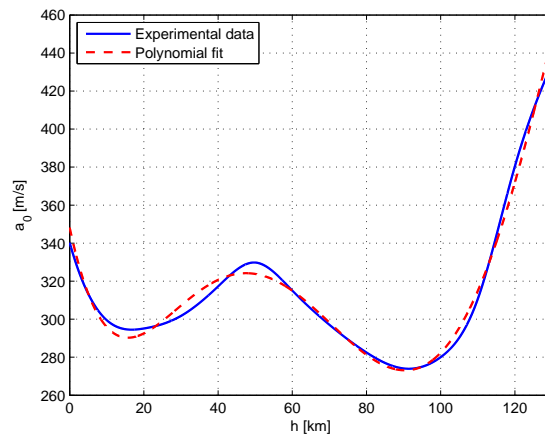


Figure 4.6: Speed of sound interpolation for the Earth.

temperature, which varies with altitude and is found by interpolating the

data in reference [36] with a polynomial function of altitude:

$$T = \tau_m h^m + \tau_{m-1} h^{m-1} + \dots + \tau_1 h + \tau_0 \quad (4.14)$$

The validity of the approximation is shown in figure 4.7.

Coefficient	Value
τ_5	-2.86×10^{-22}
τ_4	1.082×10^{-16}
τ_3	-1.388×10^{-11}
τ_2	7.199×10^{-7}
τ_1	-0.01364
τ_0	292.2

Table 4.3: Temperature model coefficients for the Earth.

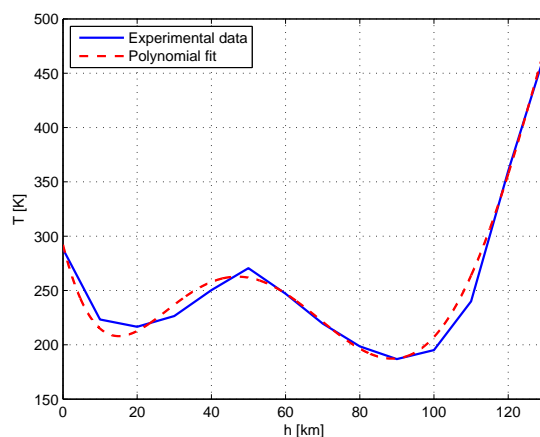


Figure 4.7: Temperature interpolation for the Earth.

According to the same approximating but low-computationally demanding approach, the target planet is assumed to be spherical and its gravity field is simplified as:

$$g = g_0 \left(\frac{R_{pl}}{R_{pl} + h} \right)^2 \quad (4.15)$$

where g_0 is the gravitational acceleration at the planetary surface and R_{pl} is the planetary mean radius.

Useful bulk, orbital and atmospheric parameters for the Earth and Mars derived from NASA Planetary Fact Sheets [37] [38] and from reference [36] are reported in table 4.4. The atmospheric interface is supposed to be at an altitude of 130 km for both planets.

Table 4.4: Planetary bulk, orbital and atmospheric parameters.

			Earth	Mars
Mean radius	R_{pl}	$[km]$	6371	3389.5
Surface gravity	g_0	$[m/s^2]$	9.8	3.71
Surface density	ρ_0	$[kg/m^3]$	1.217	0.02
Scale height	H	$[km]$	8.5	11.1
Sidereal rotation period	T_{rot}	$[hrs]$	23.9345	24.6229
Rotational velocity	ω_{pl}	$[rad/s]$	7.2921×10^{-5}	7.0882×10^{-5}
Atmosphere molar mass	M	$[kg/kmol]$	28.97	43.34
Ratio of specific heats	c_p/c_v	$[-]$	1.4	1.33

4.3 Vehicle geometry, volume and mass

4.3.1 Geometry

Various geometries have been proposed for manned entry vehicles. For sake of simplicity, an Apollo derivative configuration was selected early in this project. The original Apollo CM could host a crew of three; it was 3.9 m in diameter and 32.5° in sidewall angle. The resulting OML volume was of 15.8 m³ and the pressurized volume was of 10.4 m³.

The main reason for the early selection of the configuration is that the author considered it was not beneficial to the aim of the project to spend too much time and energy in the construction of aerodynamic databases for multiple geometries. The reader should refer to section 4.4 for further discussion on the subject. In addition, in the Exploration Systems Architecture Study (ESAS) [39] it was found that an Apollo-style blunt-body capsule is the best approach to the development of a Crew Exploration Vehicle, because this is the safest and the most affordable configuration.

The shape of the reentry vehicle is parametrized on the radius R , keeping the sidewall angle and the proportions fixed with respect to the Apollo CM. In particular, the shape of the vehicle is described by the following dimensions,

which are shown in figure 4.8:

$$\alpha_{sw} = 32.5^\circ \quad (4.16a)$$

$$l = 1.85R \quad (4.16b)$$

$$d = 0.18R \quad (4.16c)$$

$$h_c = l - \frac{R}{\tan(\alpha_{sw})} \quad (4.16d)$$

$$R_n = \frac{R^2 + h_c^2}{2h_c} \quad (4.16e)$$

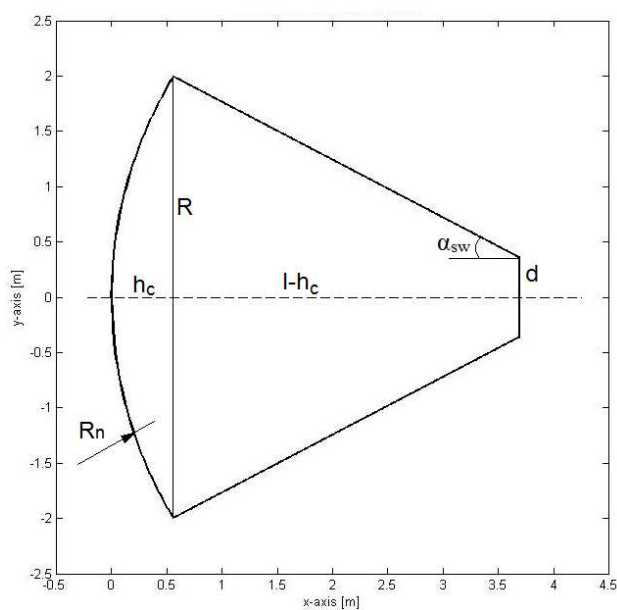


Figure 4.8: Apollo CM geometry.

Useful surface quantities for the subsystems sizing are the frontal section area and the OML surface. The frontal section area is simply computed as:

$$S_c = \pi R^2 \quad (4.17)$$

The OML surface is the sum of the surfaces of the spherical cap and of the lateral and top surfaces of the truncated cone:

$$S_{OML} = 2\pi R h_c + \pi(d + R)a + \pi d^2 \quad (4.18a)$$

$$a = \sqrt{(l - h_c)^2 + (R - d)^2} \quad (4.18b)$$

Table 4.5: Apollo and CEV pressurized and OML volumes.

Configuration	Diameter [m]	V_{OML} [m ³]	V_p [m ³]	V_p/V_{OML} [-]
Apollo	3.9	15.8	10.4	0.66
CEV	5.5	45.9	29.4	0.64

4.3.2 Volume

The OML volume, that is the total encumbrance of the capsule, is computed simply by summation of the truncated cone's and of the spherical cap's volumes:

$$V_{OML} = \frac{\pi h_c}{6}(3R^2 + h_c^2) + \frac{\pi R^2(l + l_1 - h_c)}{3} - \frac{\pi d^2 l_1}{3} \quad (4.19a)$$

$$l_1 = \frac{d}{\tan(\alpha_{sw})} \quad (4.19b)$$

The pressurized volume, that is the total volume within the pressure shell, is estimated as a percentage of the OML volume. In particular, it is assumed to be two-thirds of the OML volume:

$$V_p = \frac{2}{3}V_{OML} \quad (4.20)$$

This result is derived from the values in table 4.5, which collects previous results for Apollo-like capsules (source: ESAS Final Report [39]).

The habitable volume is the space available to the crew accounting for the hardware, the stowage and any other equipment installment. This quantity is sometimes referred to as the *sand volume*; this name makes the nature of this quantity clear: it is the equivalent volume of sand that would fill the pressurized module after the installment of the equipment, including inaccessible corners.

For the design of the manned entry vehicle in the present work a much useful quantity is the NHV, which accounts for the loss of space due to structural inefficiencies that decrease the functional volume, in addition to all the installed equipment. Since the purpose of the work is a preliminary study, the NHV is once again estimated from the historical values reported in table 4.6. The author decided it was reasonable to assume it as the half of the pressurized volume:

$$NHV = \frac{1}{2}V_p \quad (4.21)$$

In tables 4.5 and 4.6, the highlighted columns give the percentage values that were used as a reference for the volumetric estimations. For the creation

Table 4.6: Apollo, Soyuz and CEV pressurized and net habitable volumes.

Configuration	V_p [m^3]	NHV [m^3]	NHV/V_p [-]
Apollo	10.4	6.17	0.59
Soyuz	6.5	3.8	0.58
CEV	29.4	12 – 15	0.41 – 0.51

of these tables, the Soyuz and the Apollo CM facts were derived from NASA [24]; the CEV facts, as well as the Apollo CM pressurized volume, were drawn from reference [39].

4.3.3 Mass

The vehicle's total mass at the entry interface includes the estimated mass of the crew, of the structure, of the propulsion subsystem, of the parachutes and of the heat shield. Components other than those listed above are not modeled at the current state of the project and are taken as parameters or added by means of a percentage increase on the known masses. In particular, the ECLSS mass is assumed to be known, for a certain size of the crew and a certain duration. The mass of the remaining subsystems is estimated as 40 % of the mass of those that are sized. Note that the mass of the subsystems is augmented of 30 % by reason of the fact that the sizing is preliminary. The total mass is given by:

$$m_{TOT} = m_{crew} + 1.3 m_{subsystems} \quad (4.22a)$$

$$m_{subsystems} = 1.4 (m_s + m_{hs} + m_{prop} + m_{P1} + m_{P2} + m_{ECLSS}) \quad (4.22b)$$

where m_{crew} is the term relative to the crew, m_s , m_{hs} and m_{prop} are the masses of the structure, of the heat shield and of the motors, and m_{P1} and m_{P2} are due to the parachutes.

A worse case scenario is considered in the definition of the crew mass, supposing that each crewmember is a male, corresponding to the 95th percentile in height with heavy weight as defined in NASA's HIDH [24]:

$$m_{crew} = 99.157 N_{crew} \quad kg \quad (4.23)$$

Parachute masses are derived as reviewed in section 4.5. TPS, propulsion subsystem and structure masses are computed as explained in sections 4.7, 4.8 and 4.9, which address these subsystems in greater detail.

Table 4.7: Launchers reference performance.

	Fairing diameter [m]	Payload mass to GTO [kg]
Ariane 5	5.4	1000 ÷ 9500
Soyuz	4.11	3250
Vega	2.6	n.a.

4.3.4 Launcher capabilities

Launcher capabilities impose constraints on maximum mass and size of the payload. The present section briefly describes the state-of-the-art launchers and their performance, in order to derive limitations for the capsule in hand.

The European fleet of launch vehicles is composed of Ariane, Soyuz (the Russian launcher) and Vega, which address all the needs for access to space. Ariane 5 is the most powerful launcher, used to deliver heavy satellites to Geostationary Transfer Orbits (GTO); Soyuz is employed for medium mass missions to LEO and Earth Escape Orbits; Vega completes the set, offering easier and cheaper possibility to place small satellites in polar and Low Earth Orbits. Soyuz launcher is the carrier for the eponymous capsule, able to transport a crew of three to the ISS and back on Earth. Additional available launchers are produced by the private space transport company SpaceX (Space Exploration Technologies Corporation); Falcon family of launch vehicles offers light, medium and heavy lift launch capabilities. Other launchers used for NASA missions are ULA's Atlas and Delta.

Launcher performance is typically expressed in terms of payload mass, including the spacecraft's, the adapters' and the dual launch system's mass. Reference performance for European launchers is summarized in table 4.7, together with the fairing diameter. Data were retrieved in publicly available versions of user's manuals [40] [41] [42].

The present work does not envisage the development of a brand new launcher, relying on the ability of the state-of-the-art products to deliver sufficient mass on a transfer orbit. Among the available launchers, the one that seems to suit interplanetary missions best and that grants higher performance is Ariane 5. This is the reason why constraints are derived referring to this vehicle. According to Arianespace [40], Ariane 5 evolutions will provide increased payload capacity, flexibility and reliability. Additional propulsive capabilities could also be provided by a SM linked to the capsule, which is necessary in any case to provide the travelling crew with necessary habitable volume (especially for interplanetary missions), consumables and

environmental support. The present study does not include the SM sizing; therefore, no constraint is imposed on the maximum total mass. The only considered limitation is on the maximum radius of the capsule, that must be lower than the radius of the launcher fairing. For Ariane 5 launcher this results in the following inequality:

$$R \leq 2.7 m \quad (4.24)$$

4.4 Aerodynamics

The knowlegde of the aerodynamic lift and drag coefficients of the capsule is necessary to compute the lift and drag forces acting on the vehicle. These coefficients vary with the object's shape and size, the flow's velocity and direction and the fluid's density and viscosity. Their determination requires a number of techniques for the different flow regimes to which the vehicle is exposed during its descent: a complete study of a vehicle's aerodynamic properties combines numerical simulations and experimental measurements in wind tunnels. An example of the variety of tools that are necessary to assemble a complete aerodynamic database is shown in figure 4.9, which depicts the methods used for the Mars Microprobe aerodynamic design [43]. As it

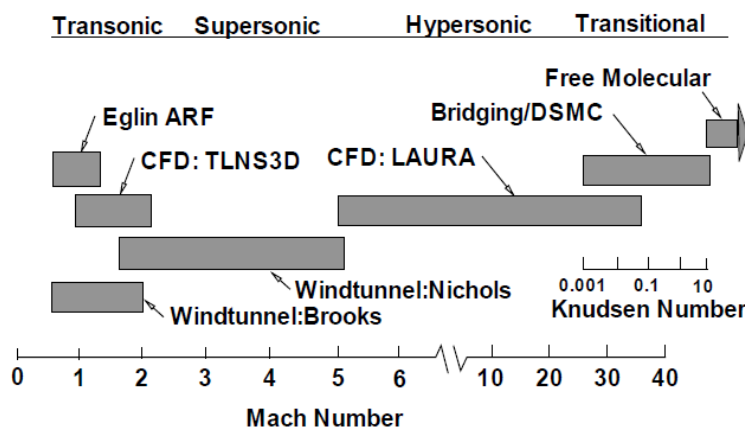


Figure 4.9: Tools used to create Mars Microprobe aerodynamic database.

can be seen in the graph, the aerodynamic characteristics in the rarefied layer of the atmosphere were obtained by means of free molecular and Direct Simulation Monte Carlo (DSMC) analyses. The Langley Aerothermodynamic Upwind Relaxation Algorithm (LAURA) was employed to supplement these results and address the continuum hypersonic flow regime. Supersonic, transonic and subsonic flow regimes were studied with a combination of wind

tunnel tests and numerical simulations.

In the present work, for lack of the time necessary to study the different flow regimes, the choice was made to select the Apollo configuration and refer to an existing database. Usually, C_L and C_D values are tabulated in function of Mach number and angle of attack. For the Apollo CM, aerodynamic data are collected in NASA technical report [44], for Mach numbers ranging from 0.4 and 9 and angles of attack between 0° and 180° . Assuming that the angle of attack is not available as a control and the vehicle keeps travelling at the trim angle of attack α_{trim} , the dependence of the aerodynamic coefficients is reduced to the Mach number alone. The adopted approach is a polynomial fit of the coefficients $C_D(Ma)$ and $C_L(Ma)$ at the trim angle of attack. This angle depends on the position of the center of mass of the capsule; for an Apollo capsule whose center of gravity offset is $z_{CG} = 0.04 D$ (where D is the capsule's diameter), it is $\alpha_{trim} = 160^\circ$, according to Stanley et al. [39]. In order to enhance the accuracy of the interpolation, three different polynomials were used in different Mach number ranges: subsonic and transonic together, supersonic and hypersonic. The result is shown in figure 4.10, where the circles and the squares represent the experimental data and the solid and dashed lines are the interpolation curves.

4.5 Parachutes

Parachutes exploit aerodynamic drag to slow vehicles down to an impact velocity that allows for a safe landing. The drag they produce depends on their shape, by means of the drag coefficient, their size, through the reference area, and the motion in the atmosphere, through air density and velocity:

$$D = \frac{1}{2} \rho V^2 S C_D \quad (4.25)$$

The drag coefficient is supposed to be dependent on the parachute type alone; some typical values are listed in table 4.8 [45]. The present work considers a conical ribbon drogue parachute and a ringsail main parachute.

In order to keep the dynamic model as simple as possible, a parachute deployment is simulated with an instantaneous augmentation in drag and a parachute release corresponds to an instantaneous decrease in mass. The parachutes deployment is subject to constraints that define a *parachute box* of allowable deployment altitude-velocity pairs. The considered limits for the decelerators are shown in table 4.9 and drawn as a parachute box in figure

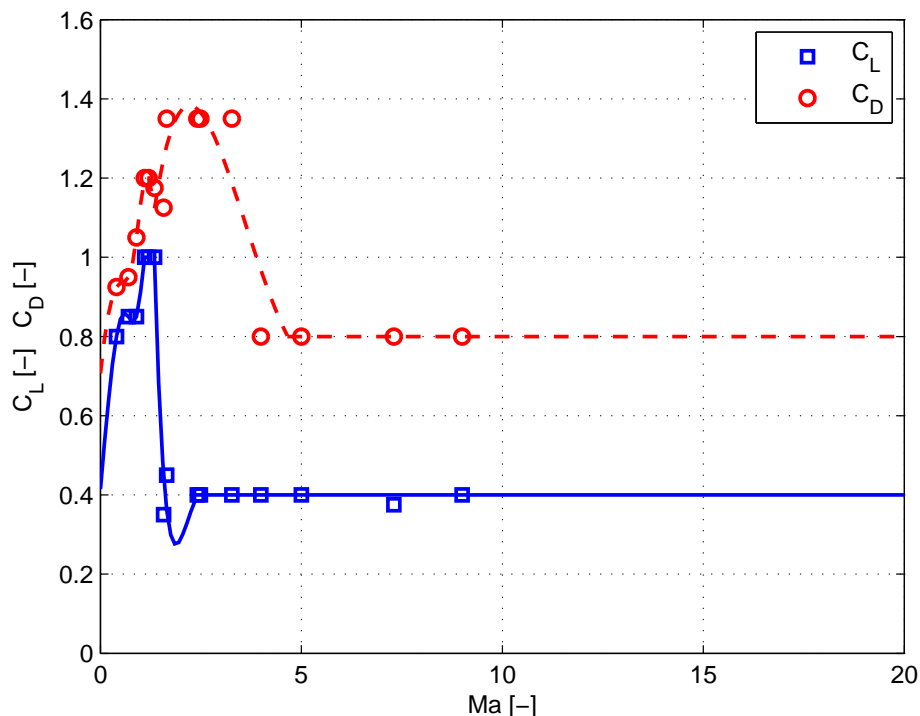


Figure 4.10: Aerodynamic coefficients interpolation at $\alpha_{trim} = 160^\circ$.

4.11, for the drogue parachute alone. Limits on the ringsail parachute deployment dynamic pressure are derived from reference [46]; the considered Mach numbers are in the subsonic range. The Mach number for the deployment of the drogue parachute is assumed to be in the transonic range, since its aim is the stabilization of the capsule in this flight regime; the limits on the dynamic pressure come from the Apollo experience [47]. In the graph, blue and red lines represent constraints on the deployment Mach number and dynamic pressure respectively. The trajectory defined by a vehicle in its descent must pass into this envelope so that the parachutes can physically

Table 4.8: Typical drag coefficients.

Type of parachute	C_D [-]
Conical ribbon	0.50 – 0.55
Ringsail	0.75 – 0.90
Disk-Gap-Band	0.52 – 0.58

Table 4.9: Parachutes deployment constraints.

Type of parachute	Ma [-]	P_{din} [Pa]
Drogue	0.8 – 1.2	480 – 9760
Main	0.2 – 0.75	300 – 5800

open in a correct way.

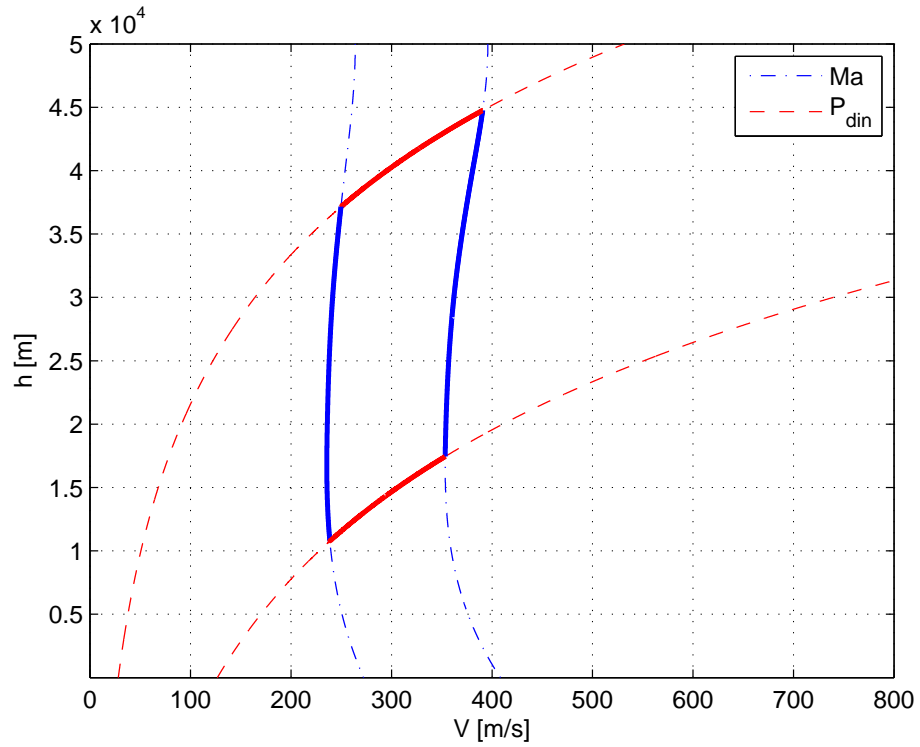


Figure 4.11: Drogue parachute box.

The mass of the parachutes is calculated by applying a modified version of the TWK method outlined by Knacke [48]. According to this procedure, the mass of a parachute can be computed as the sum of the masses of the canopy, of the radial tapes and of the suspension lines:

$$m_{par} = S_0 w_c + \frac{D_0}{2} N_G w_{RT} \frac{F_{RT}}{1000} + N_{SL} L_{SL} w_{SL} \frac{F_{SL}}{1000} \quad (4.26)$$

In this formula, D_0 and S_0 are the diameter and the surface area of the canopy; w_c , w_{RT} and w_{SL} are the specific weights of the canopy, of the radial

tape and of the suspension lines, respectively; N_G and N_{SL} are the number of gores and of suspension lines, respectively; F_{RT} and F_{SL} are the strengths of the radial tape and of the suspension lines; L_S is the length of the suspension lines. A similar approach to the assessment of a parachute's weight was given by French [49], who derived an analytical correlation by comparing the mass and configuration data for 59 parachutes; in this case, the chute mass is proportional to $N_{SL} P_{SL} D_0$, where N_{SL} and D_0 are defined as above and P_{SL} is the rated ultimate strength of a suspension line.

The TWK method was judged to be too accurate for the scope of this work, since the details of the parachutes are not likely to be known in a preliminary phase of the project. Suspension lines and radial tapes masses were not considered and the parachute mass is computed as the sum of those of the canopy and the mortar used to deploy it:

$$m_p = m_{canopy} + m_{mortar} \quad (4.27)$$

To make things simple, the parachutes' canopies are approximated to hemispherical shells and their mass is estimated as suggested by Knacke. Once the radius of a parachute is known, the evaluation of the canopy mass is straightforward:

$$S_0 = 2\pi R_0^2 \quad (4.28a)$$

$$m_{canopy} = S_0 w_c \quad (4.28b)$$

The specific canopy weight for standard design was evaluated by Knacke as $0.105 \text{ lb}/\text{ft}^2$ ($0.5127 \text{ kg}/\text{m}^2$).

The mortar mass is estimated with a correlation derived by Otero and Braun [13]:

$$m_{mortar} = 1.48 m_p^{0.5} \quad (4.29)$$

The parachutes mass validation is performed with respect to data on the Apollo drogue parachute, from Ewing et al. [47]. According to this reference, the drogue parachute assembly weighted 22.6 kg ; the overall mass computed with the present model for the same canopy radius is of 27.0 kg , corresponding to a relative error of about 19%.

4.6 Aerothermodynamics

In the atmospheric phase of the reentry, the vehicle has to dissipate the considerable kinetic and potential energies that are associated to its velocity and altitude on orbit. This happens by means of the aerodynamic friction

Table 4.10: Convective heat rate constant for the Earth and Mars.

	k
Earth	1.74153×10^{-8}
Mars	1.9027×10^{-8}

between the vehicle's walls and the atmosphere, which converts kinetic and potential energies into heat. The convective and radiative thermal loads to which the capsule is subject during its descent can be evaluated by using simple and established analytical expressions for stagnation-point heating. Since worst-case conditions are experienced at the stagnation point and at hypersonic speeds, this type of study is sufficient to provide a first estimate of the heat load to be dissipated by the TPS. In a preliminary analysis, no high-fidelity thermal response model is available nor required; furthermore, in order to perform a large number of preliminary trade studies, low computational effort is wanted.

Sutton and Graves [50] derived a general equation for stagnation-point convective heat transfer for axisymmetric blunt bodies entering planetary atmospheres at high velocities, under the assumption that gas mixtures are in chemical equilibrium. Convective heat rate can be found as:

$$\dot{q}_c = k \sqrt{\frac{\rho}{R_n}} V^3 \quad (4.30)$$

where k is a constant derived for the desired planetary atmosphere composition, ρ is the atmospheric density, R_n is the nose radius of the heat shield and V is the velocity. According to Dec and Braun [51], if \dot{q}_c is in W/cm^2 , k takes the values in table 4.10.

Engineering correlations are available for radiative stagnation-point heat rates. Assuming thermochemical equilibrium, Tauber and Sutton [52] derived correlations in the form:

$$\dot{q}_r = C R_n^a \rho^b f(V) \quad (4.31)$$

where C is a constant that depends on the atmosphere, while a and b are either constants or functions of ρ and V . The values of these quantities for the Earth's and Mars' atmospheres are shown in table 4.11. The value of $f(V)$ for any velocity and for a given atmosphere can be obtained by polynomial interpolation of the values tabulated in reference [52]. Since this quantity is defined only for a limited range of flight velocities, the evaluation of the radiative heat rate is not possible during the whole descent; this leads to

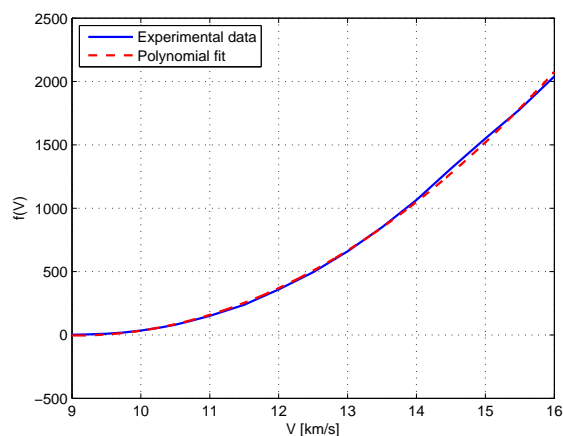
Table 4.11: Radiative heat rate constants for the Earth and Mars.

	a	b	C
Earth	$1.072 \times 10^6 V^{-1.88} \rho^{-0.325}$	1.22	4.736×10^4
Mars	0.526	1.19	2.35×10^4

an underestimation of the total heat load in the stagnation point in certain phases of the flight. However, we expect the peak radiative heating (which is the only value that is considered in the end) to occur in the ranges where $f(V)$ is defined. Moreover, radiative heat rate is two orders of magnitude smaller than convective heat rate and can be reasonably neglected outside its peak range. The polynomial approximation of $f(V)$ for the Earth is shown in figure 4.12, for velocities between 9 and 16 km/s . The polynomial is obviously a function of velocity:

$$f(V) = f_m V^m + f_{m-1} V^{m-1} + \dots + f_1 V + f_0 \quad (4.32)$$

Coefficient	Value
f_2	4.319×10^{-5}
f_1	-0.7824
f_0	3539

Table 4.12: $f(V)$ interpolation coefficients for the Earth.Figure 4.12: $f(V)$ interpolation for the Earth.

Stagnation-point convective and radiative heat rates are finally added to obtain the stagnation-point total heat rate profile along the trajectory:

$$\dot{q}_{tot} = \dot{q}_c + \dot{q}_r \quad (4.33)$$

Validation of the aerothermodynamics code was performed referring to the MPF. According to Dec and Braun [51], the peak convective stagnation-point heat rate for MPF was about $106 W/cm^2$. With the proposed model,

the maximum convective stagnation-point heat rate is of about 107 W/cm^2 , consisting in a relative error of less than 1%. Moreover, comparing the obtained results for maximum total stagnation-point heat rate to the combined peak heat rate used by Dec and Braun in reference [51], the relative error is of about 6%.

4.7 TPS sizing

The Thermal Protection System's aim is to protect the spacecraft's interior from convective and radiative heating during an atmospheric entry. In particular, it is designed to maintain operating temperatures for all the other subsystems and equipments and to preserve comfortable temperatures in the crew compartment. The two main classes of employed systems are radiative and ablative TPS. Radiative TPS dissipate heat by radiating it towards the atmosphere and do not involve mass or shape changes during exposure; ablative TPS, instead, handle heat loads by means of phase change and mass loss. Even though absorptive systems are comparately more complex and heavier, they can accomodate higher heating rates, such as those that are typical of planetary entries.

In the framework of this investigation, the selected TPS is an ablative heat shield. Many protective materials have been produced and used for manned and robotic missions: for example, the Apollo CM was covered with Avcoat 5029-39, while Stardust probe was protected by PICA. An extensive survey on materials that can be used for thermal protection was made in the early Nineties by Williams and Curry [53]. A more recent database could be found on the Internet [54], but was shut down in the period of the present research. In absence of state-of-the-art data on TPS materials, it was chosen to consider Avcoat 5029-39. The thermophysical quantities of interest for this material were collected from Larson and Wertz [19] and from Ko et al. [55] (see table 4.13).

The temperature of the external wall of a vehicle subject to aerodynamic heating can be estimated by means of the local radiative equilibrium equation:

$$T_w = \left(\frac{\dot{q}_{tot}}{\sigma_b \varepsilon} \right)^{1/4} \quad (4.34)$$

where \dot{q}_{tot} is the total heating rate, σ_b represents the Stefan Boltzmann constant and ε is the surface emissivity. In order for the Avcoat to successfully withstand the EDL environment, the maximum wall temperature T_w and the maximum heating rate \dot{q}_{tot} (computed for the whole trajectory with the procedure explained in section 4.6) must be lower than the material's limit

Table 4.13: Avcoat 5029-39 thermophysical properties.

Density	ρ_{TPS}	$[kg/m^3]$	528.6
Conductivity	k_{TPS}	$[W/m^\circ F]$	0.1346
Ablation temperature	T_{abl}	$[^\circ F]$	1200
Limit temperature	T_{lim}	$[K]$	3033
Limit heat flux	\dot{q}_{lim}	$[W/cm^2]$	432
Heat of vaporization	q_{vap}	$[J/kg]$	2.6516×10^7
Heat of decomposition	q_{dec}	$[J/kg]$	1.1630×10^6
Combustion enthalpy	Q_v	$[J/m^3]$	1.4631×10^{10}

temperature and limit heat rate, respectively.

The aim of the TPS sizing is to evaluate the mass of the shield required for the insulation of the interior of the capsule. In this project, the TPS sizing is performed so that the temperature of the OML structure is in the operative limits of the structural material (450 K [39]).

The thermal protection material forming the outer layer is ablated when the wall surface temperature is higher than the characteristic ablation temperature. The total heat of ablation Q_{abl} is the integral of the stagnation point heating rate in time, for the instants of time when this condition is verified:

$$Q_{abl} = \int_{t_i}^{t_f} \dot{q}_{tot}(t) dt \quad (4.35)$$

where t_i and t_f are the initial and final instants of time for which the wall temperature is above the ablation temperature. Once the total heat of ablation is known, the recession layer thickness is estimated in a straightforward way by dividing it by the material's combustion enthalpy:

$$\delta_{abl} = \frac{Q_{abl}}{Q_v} \quad (4.36)$$

When this thickness of material has been ablated, the external wall is at the characteristic temperature of ablation, which would be too high for the structure. Some additional amount of protective material must be present to allow for insulation and prevent the structure from melting. If $\dot{q}_{tot}(t_f)$ is the heating rate once the shield has been ablated, $T_w(t_f)$ is the wall temperature in that moment, T_{max} is the structure's maximum allowable temperature and k_{TPS} is the conductivity of the TPS material, the necessary additional thickness is found by means of a simple conduction equation, assuming that

the material is characterized by uniform properties:

$$\delta_{cond} = k_{TPS} \frac{T_w(t_f) - T_{max}}{\dot{q}_{tot}(t_f)} \quad (4.37)$$

Finally, the TPS mass is estimated as:

$$m_{TPS} = \rho_{TPS}(\delta_{abl} + \delta_{cond})(2\pi R_n h_c) \quad (4.38)$$

where R_n and h_c are geometric quantities defined in section 4.3 and ρ_{TPS} is the TPS material density.

The structural mass of the heat shield is estimated as:

$$m_{TPSstru} = 0.2 m_{TPS} \quad (4.39)$$

Finally, the total heat shield mass is found by adding this to the TPS mass:

$$m_{hs} = m_{TPSstru} + m_{TPS} \quad (4.40)$$

The TPS sizing is once again validated against the Mars Pathfinder entry system. According to Otero and Braun [13], the MPF heat shield flight mass was of 64.4 kg; with the abovedescribed model, the heat shield mass is of 64.3 kg, which corresponds to an error of less than 2% in modulus.

4.8 Propulsion system sizing

The propulsion system onboard an entry capsule includes the retrorockets for a soft landing and the thrusters devoted to attitude control. At the time of writing, the RCS propulsion is not considered in the mass budget.

Since the retrorockets are activated just once, soon before the touchdown, solid propellant thrusters offer the most simple and reliable solution for decelerating the capsule. The landing system used for the Soyuz crew module, composed of six retrorockets, provided the scientific community with valuable experience on this technology.

The preliminary evaluation of the fuel budget is performed by applying the definition of specific impulse. Indicating the thrust with T_r , the propellant flow rate with \dot{m}_p and the gravitational constant with g_0 , the specific impulse is defined as:

$$I_{sp} = \frac{T_r}{\dot{m}_p g_0} \quad (4.41)$$

Supposing that the thrust and the specific impulse are constant in time, equation 4.41 can be integrated over time to obtain the mass of propellant

required to slow the capsule down to the aimed impact velocity:

$$m_p = \frac{T_r}{g_0 I_{sp}} \Delta t \quad (4.42)$$

where Δt is the burning time and the specific impulse I_{sp} , which depends on the type of propellant, is in the range of 200 to 300 s for solid thrusters. To verify the consistency of the aforescribed model, this mass is plot in function of the total impulse $I_{tot} = T_r \Delta t$, in figure 4.13, together with data for solid rocket motors retrieved in reference [56]. As it can be seen, the representative historical data always fall in the area defined by the limiting cases of $I_{sp} = 200$ s and $I_{sp} = 300$ s.

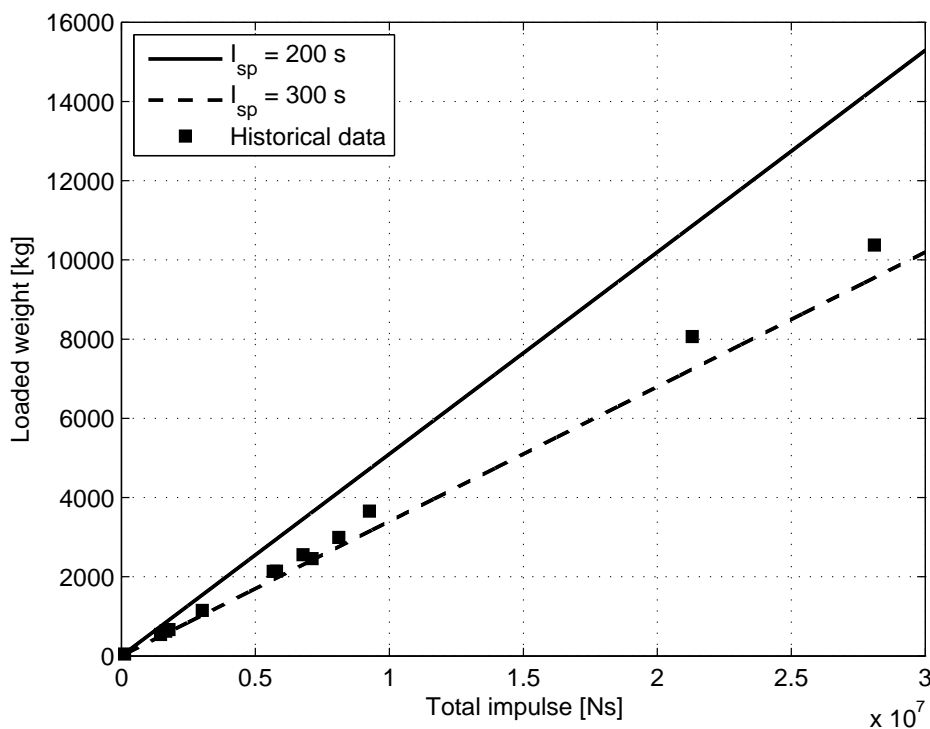


Figure 4.13: Propulsion subsystem mass in function of the total impulse.

Some margin, typically 10 – 25% of nominal, is added to the mass of propellant, in order to account for the residual propellant and the fact that the design is preliminary. To close the propulsion system budget, the mass of the engine itself should be assessed. Larson and Wertz [56] suggest that solid rocket motors mass fractions are as low as 5 – 10% of the total propellant,

including the case and nozzle assembly. Therefore, the total mass allocated for the propulsion subsystem is:

$$m_{prop} = m_p + m_{margin} + m_{engine} = 1.375 m_p \quad (4.43)$$

where the mass of propellant is derived through equation 4.42.

Validation of the propulsion subsystem sizing was performed by comparing the results with those of a study on a retrorocket system for Orion capsule by Jet Propulsion Laboratory (JPL) and NASA Langley Research Center [57]. This study considered a capsule equipped with four 7000 *lbf* (about 31100 *N*) vertical rockets which are fired for 0.5 seconds, starting from a vertical velocity of 25 *ft/s* (7.6 *m/s*) and landing at the nominal velocity of 5 *ft/s* (1.5 *m/s*). The mass obtained for the recommended configuration was of 61 *kg*, including propellant, motor casing, structural attachments, safety devices and cabling. In similar conditions, with the simple model proposed for this work, the estimated mass is of about 47 *kg*. This corresponds to a relative error of nearly -23% . This is acceptable because the present model does not consider the presence of cabling, structural attachments and safety devices. Moreover, a 30% margin should be added to the mass value in a preliminary phase of the project.

4.9 Structure sizing

During the whole mission, the capsule is subject to structural loads. The primary structure must be able to endure any environment that is encountered, from the launch to the atmospheric entry.

Accurate predictions on the behaviour of a structure under static and dynamic loads and precise evaluations of its mode shapes and frequencies are usually obtained by implementing Finite Element Methods (FEMs) and exploiting the possibilities of CAD softwares. Despite their valuable capabilities, these softwares are not well-suited to be inserted into an optimization process. The preliminary sizing of the primary structure for the capsule is here performed by crudely approximating the vehicle to a cylinder with a radius equal to 70% of the capsule's radius, with the same pressurized volume and with an uniform distribution of mass. The height of the equivalent cylinder is determined through simple geometrical considerations:

$$R_{cyl} = 0.7 R \quad (4.44a)$$

$$L_{cyl} = \frac{V_p}{\pi R_{cyl}^2} \quad (4.44b)$$

Table 4.14: Ariane 5 frequency requirements.

S/C mass [kg]	1 st fundamental lateral frequency [Hz]	1 st fundamental longitudinal frequency [Hz]
$M < 4500$	≥ 10	≥ 31
$4500 \leq M \leq 4500$	≥ 8	≥ 27
$M > 6500$	≥ 7.5	≥ 27

4.9.1 Spacecraft's first natural frequency

Ariane 5 User's Manual [40] provides lower limits for the first natural frequency of the payload it carries. If the frequency requirements are not verified, the dangerous dynamic coupling between the launch vehicle and the spacecraft modes can occur. In particular, the spacecraft's stiffness must ensure that the fundamental longitudinal and lateral frequencies are higher than those listed in table 4.14. These values are valid for a spacecraft cantilevered at the launcher interface.

To estimate the first natural frequency, a single-degree-of-freedom spring-mass system adequately idealizes the spacecraft. The natural frequency of a system of this type can be computed as:

$$f_{nat} = \frac{1}{2\pi} \sqrt{\frac{\bar{k}}{\bar{m}}} \quad (4.45)$$

where \bar{m} is the mass and \bar{k} is the stiffness, that is the ratio between an applied load and the resulting deflection. If an equivalent beam is assumed to represent the spacecraft, equation 4.45 takes the following forms for axial and lateral loads [56]:

$$\text{For axial loads: } F_{nat} = 0.25 \sqrt{\frac{A_s E}{m_{TOT} L_{cyl}}}$$

$$\text{For lateral loads: } F_{nat} = 0.56 \sqrt{\frac{E I_s}{m_{TOT} L_{cyl}^3}}$$

where m_{TOT} is the total mass of the spacecraft, L_{cyl} is the height of the equivalent cylinder, $A_s = 2\pi R_{cyl} t_s$ is the section area of the cylinder, $I_s = \pi R_{cyl}^3 t_s$ is the cylinder area moment of inertia and E is the material Young's modulus; t_s indicates the thickness of the structure.

Table 4.15: Ariane 5 load factors.

Type of load	Acceleration [g]
Lateral	2
Longitudinal, tension	2.5
Longitudinal, compression	-6

4.9.2 Static and dynamic loads

The primary structure of a spacecraft must be able to avoid collapsing, rupturing or deforming in function-impairing ways. Two main concerns drive a structural sizing: resistance to compression and resistance to tension. According to Larson and Wertz [56], instability failures due to compression are the most sudden, catastrophic and difficult to predict. Other failure modes as rupture and yield in tension must also be avoided.

The most important static and dynamic loads are encountered during the launch, together with the rest of the spacecraft, and during the descent in the atmosphere. Moreover, the internal pressure necessary to the survival of the crew causes tension in the primary structure, when it is not equilibrated by the presence of an external atmosphere. This section presents the various load environments; the constraints on the primary structure will be imposed considering the worst-case situation and adapting the sizing procedure delineated in reference [56] to an optimization process.

Launcher loads

A payload is subject to varying loads during the different phases of the launch; a complete description for the design load factors that apply for Ariane 5 is given in reference [40]. Table 4.15 summarizes the worst-case conditions due to the launch environments; these load factors represent the Quasi-Static Loads (QSLs), that are the combinations of dynamic and static accelerations, and include the gravity effects.

Pressure

An additional load that must be accounted for while designing habitable modules is the effect of internal pressure, whose value was selected in section 3.1. When the vehicle travels in space, no external atmosphere is present and the pressure loads in tension cannot be equilibrated. According to Larson and Pranke [19], a structure whose failure would jeopardize the crew survival

must not rupture under twice the design internal pressure and must not yield under one and a half times the design internal pressure.

EDL loads

During its descent in an atmosphere a capsule decelerates from velocities on the order of km/s to velocities on the order of m/s in a few minutes, under the effect of aerodynamic forces, which depend on the vehicle configuration and on the trajectory. The representative quantity for the loads to which a structure is subject is the load factor, defined as:

$$\mathbf{n} = \frac{\mathbf{g} - \mathbf{a}}{g} \quad (4.46)$$

In order to evaluate axial and lateral loads, the load factor components in body axes are derived. Since there is no way to distinguish between compression and tension loads, both cases are studied.

To these loads, one should add the contribution of the differential pressure between the interior and the exterior of the capsule:

$$\Delta p = p_{int} - p_{ext} \quad (4.47)$$

A positive Δp results in a tension force, while a negative value indicates some compression. In fact, the contributions of internal and external pressures have opposing behaviors on the capsule's structure: internal pressure creates tension in the walls, while external pressure tends to compress it. It is worth noting that a capsule travelling at supersonic speed causes the generation of a shock wave ahead. Therefore, the external pressure does not depend only on the altitude, but also on the flight regime. From exact normal shock-wave theory:

$$p_{ext}(h, Ma) = \begin{cases} p(h), & \text{if } Ma \leq 1, \\ p(h) \left(1 + \frac{2 \frac{c_p}{c_v}}{\frac{c_p}{c_v} + 1} (Ma^2 - 1) \right), & \text{if } Ma > 1. \end{cases}$$

Sizing for strength

The primary structure has to resist to tension: its thickness must be sufficient to avoid rupture and permanent deformations in the worst-case among the abovementioned environments for tension. The compliance to strength requirements is imposed as follows:

1. The axial load factors in tension are multiplied by the capsule's total weight to obtain the resulting axial load P_{axial} ; the lateral load factors

are multiplied by the capsule's total weight and by the distance from the base of the cylinder to the center of mass to obtain the resulting bending moments M . For pressure, the axial and lateral loads are computed by multiplying the pressure by the base and wall areas respectively; the bending moment is found by multiplying the lateral pressure load by the distance from the base of the cylinder to the center of mass.

2. Equivalent axial loads are found according to the expression:

$$P_{eq} = P_{axial} + \frac{2M}{R_{cyl}} \quad (4.48)$$

3. Each equivalent axial load is multiplied by the ultimate factor of safety FS_u to obtain the ultimate load P_u and by the yield factor of safety FS_y to obtain the yield load P_y . The factors of safety for missions with humans aboard suggested by Larson and Pranke [19] are:

$$\text{For EDL and launch loads: } \begin{cases} FS_u = 1.4 \\ FS_y = 1 \end{cases}$$

$$\text{For internal pressure alone: } \begin{cases} FS_u = 2 \\ FS_y = 1.5 \end{cases}$$

4. Comparing the loads obtained for the different environments, the worst-case conditions for rupture and permanent deformation are indentified.
5. It is imposed that the primary structure does not rupture when subject to the ultimate load P_u , by means of the following inequality:

$$P_u \leq F_{tu} A_s \quad (4.49)$$

where F_{tu} is the ultimate tensile strength of the structural material and A_s is the cross-sectional area of the equivalent cylinder.

6. It is imposed that the primary structure does not yield when subject to the yield load P_y , by means of the following inequality:

$$P_y \leq F_{ty} A_s \quad (4.50)$$

where F_{ty} is the yield tensile strength of the structural material.

Sizing for stability

A fundamental requirement is that the primary structure is not exposed to buckling, a sudden and very dangerous instability failure of a structural member subject to high compressive stress. In compression, we can forget the case of internal pressure alone: worst-case conditions are to be identified among the launch and the EDL load environments for compression. An equivalent axial load is identified by repeating steps 1 and 2, using the maximum load factors in compression. Compliance to stability requirements is then enforced as follows:

- The equivalent axial load is multiplied by the ultimate factor of safety FS_u to obtain the ultimate load P_u .
- The critical buckling load is computed as:

$$P_{cr} = A \sigma_{cr} \quad (4.51)$$

where σ_{cr} is obtained by means of the following expressions:

$$\sigma_{cr} = 0.6\bar{\gamma}\frac{E t_s}{R_{cyl}} \quad (4.52a)$$

$$\bar{\gamma} = 1 - 0.901(1 - e^{-\bar{\phi}}) \quad (4.52b)$$

$$\bar{\phi} = \frac{1}{16}\sqrt{\frac{R_{cyl}}{t_s}} \quad (4.52c)$$

- The structural integrity under compression is imposed by verifying that the the margin of safety is greater than zero:

$$MS = \frac{P_{cr}}{P_u} - 1 > 0 \quad (4.53)$$

4.9.3 Structure mass

As it is usual in spacecraft design, we want to meet the requirements with a structure as lightweight as possible. An aluminum alloy is selected as the material for the primary structure, because it combines strength with a relatively low density. 7075 aluminum alloy properties are shown in table 4.16 [56].

Once the thickness of the primary structure t_s is known, its mass is computed referring to the equivalent cylinder, as:

$$m_{s1} = 2\pi R_{cyl} L_{cyl} \rho_{Al} t_s \quad (4.54)$$

Table 4.16: 7075 Al properties.

Density	ρ_{Al}	$[kg/m^3]$	2.8×10^3
Young's modulus	E	$[N/m^2]$	71×10^9
Poisson's ratio	ν	$[-]$	0.33
Ultimate tensile strength	F_{tu}	$[N/m^2]$	524×10^6
Yield tensile strength	F_{ty}	$[N/m^2]$	448×10^6

Table 4.17: Delta II load factors for a spacecraft of MPF's size.

Type of load	Acceleration $[g]$
Lateral	4.5
Longitudinal, tension	0.2
Longitudinal, compression	-8

An attempt of validation of the structural sizing was made against results for MPF collected in reference [13]. This probe was put on orbit by Delta II launcher, which requires that a payload characterized by a mass similar to that of MPF has a structural stiffness that produces fundamental frequencies higher than $35 Hz$ in axial direction and $15 Hz$ in lateral direction [58]. The load factors to which a spacecraft of that size is subject during a launch with Delta II are approximately those in table 4.17. Reference [13] reports a structural mass of $56.9 kg$, including the backshell mass. According to the formulated model, a spacecraft with the same radius and mass as the MPF, subject to the abovementioned requirements, needs a primary structure mass of $39.7 kg$, which corresponds to a relative error of about -30% . The reasons for this significant difference are to be researched in the limits of the validation in terms of model and scenery. First, the proposed sizing is performed considering a sole degree of freedom, while a complete spacecraft design employs FEM. Second, the fundamental assumption is that the capsule is considered to be cantilevered directly to the launcher, which is not accurate. The probe or the CM is more likely installed on the top of a SM; the way in which this connection is performed influences the structural properties of the capsule. Moreover, this attempt of validation only considers the loads produced during the launch, without taking into account the EDL loads. A final consideration is that, in the preliminar phases of the design, a 30% margin is typically added.

In addition to the pressure vessel structure able to withstand the internal pressure and carry the dynamic loads, a vehicle for the transportation of humans benefits from an OML unpressurized structure that gives it an aerodynamic shape. Supposing that this structure is made of a composite material, as suggested in reference [39], its mass can be estimated by multiplying the OML surface S_{OML} defined by equation 4.18a by a scaling factor of 11.6 kg/m^2 . The total mass of the structure is the sum of the primary and the OML structures:

$$m_s = m_{sOML} + m_{s1} \tag{4.55}$$

Chapter 5

Multidisciplinary Optimization

Be thankful for problems. If they were less difficult, someone with less ability might have your job.

James A. Lovell
Apollo 13 Commander

Chapters 3 and 4 have presented the models for the disciplines involved in the design of a manned vehicle for EDL in a planetary atmosphere. In order to search for an optimal solution of the combined vehicle and EDL trajectory, an integrated tool has to be assembled.

This chapter introduces the MDO, discussing its capabilities and the methods and tools that can be used to perform this type of study. The general optimization problem is then formulated. The variables are chosen and the disciplinary modules are reviewed from an input-output point of view. After the definition of the constraints and the objective of the optimization, the complete architecture is presented. Finally, some methods to find global optimal solutions are reviewed, focusing in particular on the promising Particle Swarm Optimization (PSO) method.

5.1 Introduction to MDO

Engineering systems (aircrafts, ships, spacecrafts, automobiles, etc.) are multidisciplinary in nature and this salient peculiarity has always been taken into account in their design. Nonetheless, the design process has drastically evolved in the last decades. Traditional design was carried out by teams of engineers specialized on a specific discipline, whose goal was generally performance related (minimum weight, minimum drag, etc). The aim was the

satisfaction of requirements, not an optimal solution identification. The optimization process was usually sequential, based on a series of disciplinary simulations. In the final decades of the twentieth century the performance-centered approach gave way to a cost-centered one and computer-aided design made it possible to perform quicker modifications and analyses of a design. In addition to this, globalization and companies decentralization have asked for effortless sharing of design information. The recognition of these advancements and of the new demands has allowed the assertion of numerical optimization techniques and of MDO in particular.

Most authors agree that the roots of the application of MDO are to be found in structural optimization, thanks to the pioneering work by Schmit, who transferred the Nonlinear Programming (NLP) formalism to the structural optimization of a three-bar truss in 1960. This innovative optimization concept rapidly gained the attention of structural engineers and other specialists. It soon attracted the interest of the aerospace community, since in this area the interdisciplinary couplings (to structures in particular) were too strong to be neglected. Even though MDO techniques are exploited in various fields of engineering, most applications have regarded the aerospace engineering domain, for the design of vehicles ranging from aircrafts to launchers and spacecrafts. A extensive review of MDO-related publications in aerospace field was done by Sobieszczanski-Sobieski and Haftka [59].

These authors defined multidisciplinary optimization as *the methodology for the design of systems in which strong interaction between disciplines motivates designers to simultaneously manipulate variables in several disciplines*. The term *multidisciplinary* puts an emphasis on the need to consider a number of different aspects of the design problem. MDO techniques are used to solve design problems dealing with multiple disciplines, since they allow the simultaneous integration of all relevant features.

With respect to a single-discipline optimization, the MDO inherent interdisciplinary coupling increases the complexity of the problem in terms of computational expense and organizational complexity. The advantage deriving from the exploitation of the interactions between the disciplines is that the optimum of the integral problem is superior to the solution of the sequential single-discipline optimizations. MDO has the ability to assist designers by providing them with rapidly generated design solutions and by exploring the design space in an efficient way. According to Alexandrov [60], the potential benefits of MDO are worth the analytical and computational obstacles to its widespread acceptance.

5.2 MDO methods and tools

This paragraph shortly presents the principal tools and methods for MDO, with the aim to provide the reader with an idea of the various possibilities of implementation.

A survey of the MDO state of the art was published by Agte et al. in 2009 [61]. According to this group of professionals, various tools can be exploited for MDO implementation:

- general purpose tools, as Matlab and Excel;
- optimization capabilities embedded in softwares for engineering design and analysis, as CAD Solidworks;
- recently developed dedicated Process Integration and Design Optimization (PIDO) tools.

The main advantage of employing general purpose tools as Matlab is that the model and the optimizer can be captured in the same environment. Two important drawbacks are the uneasiness to integrate high-detail softwares for Computational Fluid Dynamics (CFD) and FEM (which may be useful for the study of aerodynamic and structural behavior) and a low computational performance when the number of design variables increases. The second option is typically efficient for the local optimization of one discipline at a time, while the third focuses on the design process management. In the light of these considerations, the author chose to employ general purpose tools as Matlab, that permit the creation of the model and the exploitation of built-in optimization capabilities in the same environment. A possibility that was also contemplated for MDO purposes was the use of the open-source OpenMDAO framework, developed by NASA Glenn Research Center [62].

Different methods to perform MDO with general purpose softwares exist. The first option is the generation of a monolithic code that includes different disciplinary modules in a single optimization loop; this approach is relatively simple but presents serious limitations if the number of variables is high. Some decomposition methods have been recently developed to overcome these drawbacks, namely Linear Decomposition, Collaborative Optimization, Concurrent Subspace Optimization and Bi-Level Integrated System Synthesis. The objective of these methods is to make large optimization problems more easily manageable by dividing them in smaller tasks related to single disciplines; an optimization at system level coordinates the

process and restores the couplings between the disciplines. The effectiveness of this approach depends on the coupling breadth and strength: for systems that are widely and strongly coupled, decomposition may not improve the optimization process because the dimensionality of the system-level problem may exceed that of the system without decomposition.

5.3 Problem formulation

An optimization problem is formulated mathematically with the NLP formalism. Its general form is:

$$\min f(\mathbf{x}, \mathbf{p}) \quad (5.1)$$

$$\mathbf{x} = [x_1 \dots x_n]^T \quad (5.2)$$

$$\mathbf{p} = [p_1 \dots p_m]^T \quad (5.3)$$

$$x_{i,LB} \leq x_i \leq x_{i,UB}, \quad i = 1, 2, \dots, n \quad (5.4)$$

$$s.t. \quad \mathbf{g}(\mathbf{x}, \mathbf{p}) \leq \mathbf{0} \quad (5.5)$$

$$\mathbf{h}(\mathbf{x}, \mathbf{p}) = \mathbf{0} \quad (5.6)$$

In the optimization problem, the objective is to minimize the cost or fitness function $f(\mathbf{x}, \mathbf{p})$. \mathbf{x} is a vector containing the n design variables, while \mathbf{p} is a vector of m fixed parameters. The first are the degrees of freedom controlled by the designer; the second cannot be chosen but influence the design. In a multidisciplinary optimization, the design space \mathbf{x} includes quantities that are inherent to all the disciplines that are accounted for in the model of the system. Each design variable x_i is subject to lower and upper bounds $x_{i,LB}$ and $x_{i,UB}$. The problem is also subject to inequality and equality constraints \mathbf{g} and \mathbf{h} , which can generally be nonlinear. The satisfaction of the constraints guarantees the feasibility of the solution, in terms of user requirements, resource availability and physical limitations.

5.4 Optimization architecture

Due to the complexity of the problem at hand, the model that was developed is quite articulated. The aim of this section is to build the optimizer, starting from the choice of the design variables, revising the inputs and the outputs of the disciplinary modules, defining the constraints and the objectives and assembling the complete architecture.

5.4.1 Parameters and variables

Many quantities influence the design of a space transportation vehicle and its trajectory. They can be optimized as variables or set as parameters; the designer has freedom on the first, but cannot change the second, which are fixed for the problem.

Parameters in the present investigation are:

- the planet where the entry occurs;
- the duration of the EDL phase $T_{mission}$ and the expected size of the crew N_{crew} ;
- the type of geometry of the capsule, which is described by the sidewall angle α_{sw} ;
- the trim angle of attack α_{trim} at which the vehicle is supposed to fly during the whole descent;
- the material of the structure and of the TPS;
- the type of the parachutes and of the retrorockets propellant;
- the launcher used to put the spacecraft on orbit.

The design variables must reflect the multidisciplinary of the problem. Since the ambition is to optimize the vehicle geometry, mass and trajectory at the same time, the variables will be related to these three domains.

Geometry

In the implemented model, the type of geometry is fixed for the capsule, but its dimensions can be optimized. The only considered variable is the radius of the vehicle R .

Mass

In order to integrate the equations of the dynamics, it is necessary to know the total mass of the object travelling in the atmosphere. For this reason, the mass of the different subsystems and of the parachutes are chosen as variables. Degrees of freedom for the design are the mass of the TPS m_{TPS} , of the structure m_s , of the propulsion subsystem m_{prop} , of the parachutes

m_{P1} and m_{P2} . As it is evident from the discussion of the sizing processes in chapter 4, these variables are not free to vary regardless of the trajectory: they will be subject to feasibility constraints.

Trajectory

Different variables concur in the definition of the trajectory:

- initial conditions: apart from the atmospheric entry altitude, which is fixed, the other initial conditions are variables for the problem. The optimizer can determine the best initial velocity V_1^i , latitude φ_1^i , longitude θ_1^i , flight path angle γ_1^i and heading angle ψ_1^i ;
- altitudes of the events: it is possible to optimize the altitudes at which the drogue parachute is deployed h_2^i and released h_3^i , the altitude at which the main parachute is deployed h_4^i , the altitudes for the jettisoning of the heat shield h_5^i and the ignition of the retrorockets h_6^i ;
- the bank angle σ , which is assumed to be the sole available attitude control;
- the thrust of the retrorockets T_r for the deceleration in the terminal phase.

As mentioned in the previous section, the design variables are subject to lower and upper bounds, exposed in table 5.1.

5.4.2 Modules inputs and outputs

Chapter 3 discussed the models used to set the requirements deriving from the presence of man aboard a reentry vehicle. Chapter 4 presented the domain-specific models and the approximations employed to simulate the environment, the trajectory and the vehicle during the descent in the atmosphere. Before building the complete architecture of the optimizer, it is useful to rethink the models from an input-output point of view, so that the interdependencies become apparent.

A first module derives the planetary quantities of interest for a given planet. Besides defining the constant physical properties of the planet and its atmosphere, it computes gravity, density, temperature, speed of sound and pressure for a certain altitude (see figure 5.1).

Table 5.1: Search space bounds for the design variables.

Variables		Lower bound	Upper bound
Geometry	R [m]	R_{min}^*	2.7
Mass	m_{TPS} [kg]	20	1000
	m_s [kg]	20	1000
	m_{prop} [kg]	20	1000
	m_{P1} [kg]	5	100
	m_{P2} [kg]	10	150
Initial conditions	V_1^i [km/s]	6	12.5
	φ_1^i [°]	-90	90
	θ_1^i [°]	-180	180
	γ_1^i [°]	-90	-2
	ψ_1^i [°]	-90	90
Altitudes of the events	h_2^i [km]	0	50
	h_3^i [km]	0	50
	h_4^i [km]	0	41
	h_5^i [km]	0	10
	h_6^i [km]	0	0.2
Bank angle	σ [°]	-90	90
Thrust of the retrorockets	T_r [kN]	0	70

* Depends on the size of the crew and on the duration of the mission.



Figure 5.1: Planetary environment code inputs and outputs.

Figure 5.2 shows that starting from the value of the capsule radius, the geometry code computes its nose radius, height of the spherical cap, pressurized volume, section area and OML surface, with the equations derived in section 4.3.

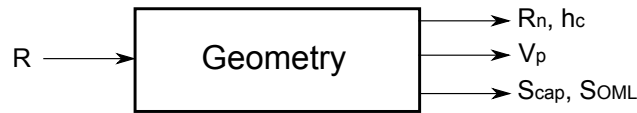


Figure 5.2: Geometry code inputs and outputs.

The mass module represented in figure 5.3 estimates the total mass from the masses of the crew, of the parachutes and of the various subsystems, as stated in paragraph 4.3.

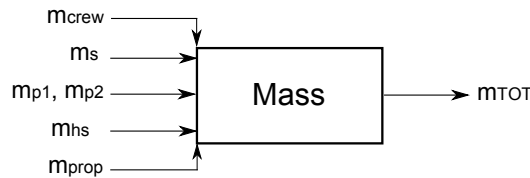


Figure 5.3: Mass code inputs and outputs.

To analyze the EDL trajectory, the equations of motion are numerically integrated from an initial set of state conditions as explained in section 4.1. The required inputs are the section area and the aerodynamic coefficients of the capsule and of the parachutes, the total mass at the entry and those of the heat shield and of the drogue parachute canopy, the bank angle, the initial conditions at the entry interface \mathbf{y}_1^i , the altitudes of the EDL events, the thrust of the retrorockets and some planetary and atmospheric quantities. The integration of the dynamics equation provides the profiles of useful quantities in time: altitude, velocity, Mach number, acceleration and load factor. Moreover, it determines the initial and final instants for the retrorockets burn (see figure 5.4).

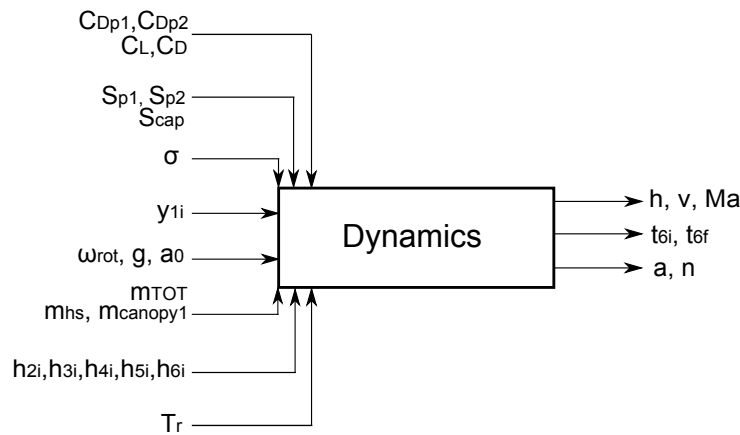


Figure 5.4: Dynamics code inputs and outputs.

The drag and lift coefficients for the capsule at any time are to be defined based on the flight Mach number, if the angle of attack is fixed and constant. This is done by the aerodynamics code, written according to the considerations in section 4.4 and schematized in figure 5.5. Note that the Mach number is an input for the aerodynamics and an output for the dynamics, while the lift and drag coefficients are outputs for the aerodynamics and inputs for the dynamics; this suggests that the aerodynamics code has to be called iteratively in the integration of the equations of motion.

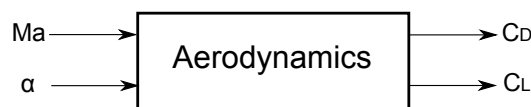


Figure 5.5: Aerodynamics code inputs and outputs.

The modules responsible for the definition of the parachutes drag coefficients, areas and deployment conditions are those in figures 5.6 and 5.7, which derive these quantities according to the relations and remarks in section 4.5, starting from the parachutes mass.

The aerothermodynamics module modeled in section 4.6 and depicted in figure 5.8 is responsible for the definition of the stagnation point heat rate profile during the descent in the atmosphere. The set of required inputs includes the atmospheric density and velocity profiles in time, the heat shield shape (specified by the nose radius) and the planetary constant for the radiative heat rate k .

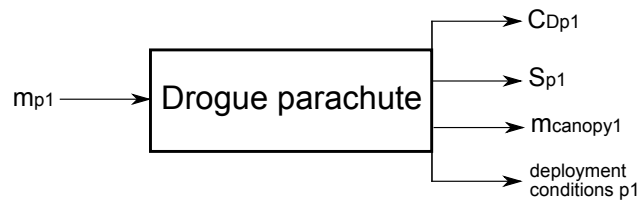


Figure 5.6: Drogue parachute code inputs and outputs.

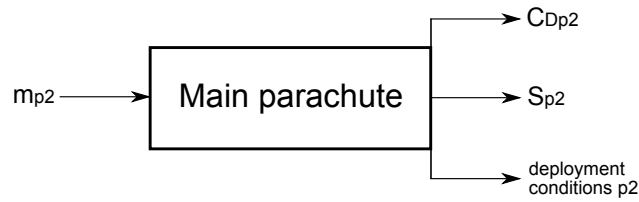


Figure 5.7: Main parachute code inputs and outputs.

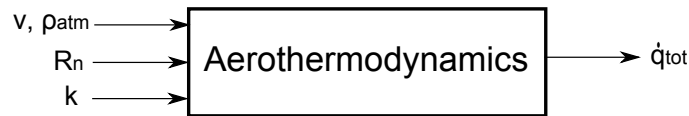


Figure 5.8: Aerothermodynamics code inputs and outputs.

The stagnation point heat rates integrated in time, together with the geometry of the heat shield (described by the nose radius and the height of the spherical cap), determine the minimum mass of the TPS, as it was explained in section 4.7 (see figure 5.9).

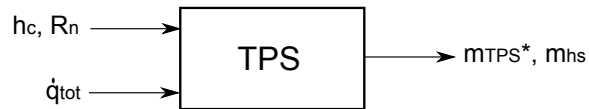


Figure 5.9: TPS code inputs and outputs.

The propulsion subsystem sizing is handled by the eponymous module, which receives as an input the thrust and the initial and final instants for the retrorockets burn and returns the mass of the required solid rocket motors, as indicated in figure 5.10.

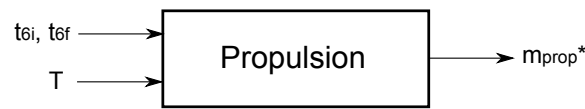


Figure 5.10: Propulsion code inputs and outputs.

The set of inputs for the structure module comprises the pressurized volume and the radius of the capsule, necessary to size the equivalent cylinder, the total mass of the capsule and that of the structure, the OML surface. Moreover, this module needs to know the launcher requirements, the atmospheric pressure and ratio of the specific heats, the profiles of the Mach number and of the load factor. The box in figure 5.11 hides the sizing process established in section 4.9, which allows for the evaluation of the margin of safety for compression, the ultimate and yield loads in tension and the natural frequencies.

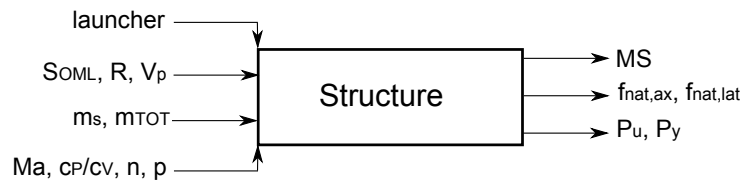


Figure 5.11: Structure code inputs and outputs.

The physiology module verifies the compliance of the acceleration experienced during the descent to the requirements due to the presence of man aboard the reentry vehicle (see figure 5.12).

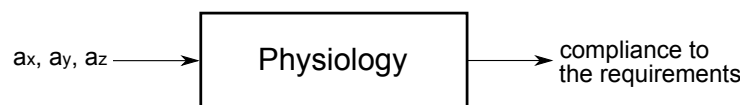


Figure 5.12: Physiology code inputs and outputs.

A complex system is conveniently represented by a Design Structure Matrix (DSM). This analysis tool provides a useful aid to system design, by visualizing in a simple and compact way the relationships between the system components. The present framework is made of eleven core modules responsible for different disciplines; the flow of information between them follows the paths displayed in figure 5.13.

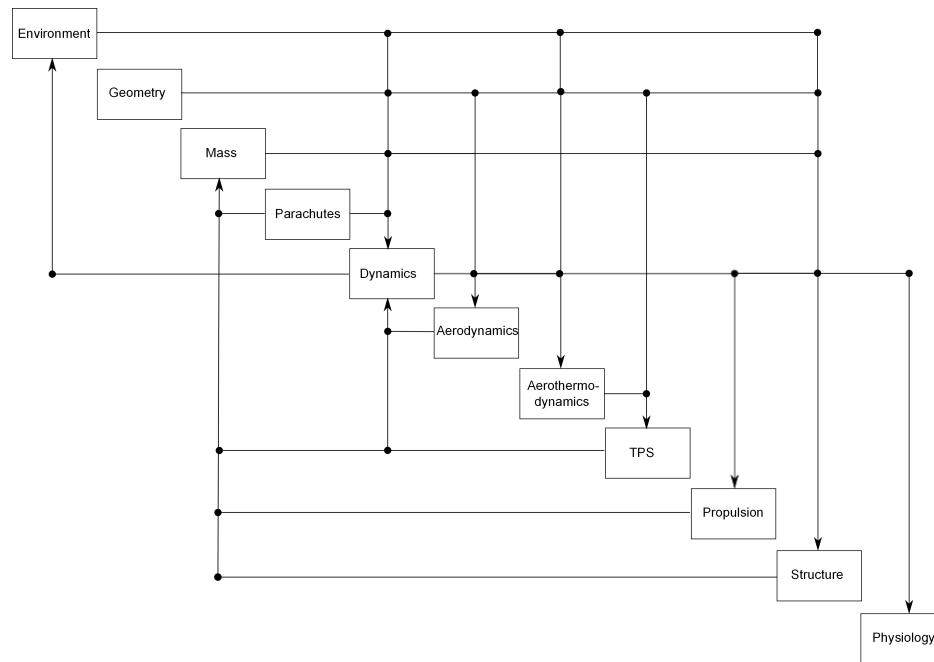


Figure 5.13: Design Structure Matrix for the framework.

5.4.3 Objectives

In complex problems, the distinction between constraints and objectives is not straightforward nor unique. If a single objective function is used, it is possible to insert constraints via Lagrange multipliers. Furthermore, one may think of building a multiobjective optimization architecture, in which some components of the fitness function are *true* objectives, whereas others are conceptually constraints; this is particularly convenient for the constraints that would be less easily satisfied. However, the use of these procedures, especially in the case of a single objective, entails the risk of shifting the focus of the optimization from the attainment of an objective to the simple verification of some constraints.

Typical objectives in EDL vehicle and trajectory design are mass minimization and landing precision. Other optimization objectives may derive from particular demands: for example, a study on Mars entry trajectory planning by Soler et al. aimed at maximizing the parachute deployment altitude while ensuring enough control authority for the last part of the descent, to reach high elevation landing sites [63].

Within the present investigation, the only objective that is considered is the

minimization of the total entry mass:

$$f(\mathbf{x}, \mathbf{p}) = m_{TOT} \quad (5.7)$$

5.4.4 Constraints

The simplest constraint relations impose that the events that mark the six phases of the descent are sequential. Since the triggering quantities are the altitudes, these values must respect the following inequalities, which are suitable to be enforced as linear constraints:

$$h_2^i > h_3^i > h_4^i > h_5^i > h_6^i \quad (5.8)$$

The continuity of the state variables between one phase of the descent and the following one is directly verified, because the integration of the equations of motion for the different phases is performed sequentially. The final state vector of the $i - th$ phase is automatically used as initial condition for the $(i + 1)th$ phase.

In order for the parachutes to deploy and work properly, the Mach number and the dynamic pressure at the deployment have to be within a certain range of values: it is what we defined as *parachute box* in section 4.5. These limits are set as nonlinear constraints, since they do not present a simple linear dependence on the design variables. For each parachute:

$$Ma_{min}^d < Ma^d < Ma_{max}^d \quad (5.9)$$

$$P_{dyn,min}^d < P_{dyn}^d < P_{dyn,max}^d \quad (5.10)$$

where $Ma = \frac{V}{a_0}$ and $P_{dyn} = \frac{1}{2}\rho V^2$ and both a_0 and ρ depend on the deployment altitude. The apex d indicates that the quantities refer to the time when the deployment occurs.

Two constraints are imposed on the TPS and propulsion subsystem masses, to guarantee that the values of the variables are higher than the masses that are actually required. Since the derivation of the needed masses for the TPS and the retrorockets requires the knowledge of some quantities computed by the dynamics module, the dependence of these constraints on the design variables is nonlinear. If m_{TPS}^* and m_{prop}^* are the necessary masses and m_{TPS} and m_{prop} are the problem variables, the constraints can be written as:

$$m_{TPS} > m_{TPS}^* \quad (5.11)$$

$$m_{prop} > m_{prop}^* \quad (5.12)$$

Multiple requirements concern the structure. As it was detailed in section 4.9, the vehicle's primary structure is sized to withstand compression and tension loads and to prevent the dynamic coupling between the launch vehicle and the spacecraft modes. The nonlinear constraints are imposed as:

$$MS > 0 \quad (5.13)$$

$$f_{nat,ax} > f_{nat,ax,min} \quad (5.14)$$

$$f_{nat,lat} > f_{nat,lat,min} \quad (5.15)$$

$$P_u < F_{tu}A \quad (5.16)$$

$$P_y < F_{ty}A \quad (5.17)$$

The impact with the planetary surface must ensure that the crew lands safely. The Brinkley Dynamic Response Model explained in section 3.2.2 is a valuable method to evaluate the risk of injuries deriving from very short duration linear accelerations, as those typical of an impact with a planetary surface. A first version of the optimizer employed this model to impose constraints on impact accelerations, but incurred in computational problems. In fact, in order to compute the injury risk criterion, it is necessary to integrate a set of dynamic equations at each instant of the descent, which is computationally very expensive. In the light of this consideration, an alternative approach was chosen to impose constraints on the impact: the landing velocity must approach a given target V_{end} , which, according to reference [57], is reasonably of 1.5 m/s with a margin of approximately 1.5 m/s ($5.0 \text{ ft/s} + 3/ - 5 \text{ ft/s}$). A nonlinear constraint is therefore imposed on the velocity at the touchdown V_6^f :

$$|V_6^f - V_{end}| < 1.5 \quad (5.18)$$

Sustained linear acceleration should be kept below the physiological limits for nominal reentry at any time during the descent. Preliminary simulations have shown that this is difficult to achieve in absence of the possibility to modulate the bank angle in time. To be able to obtain first guess solutions that take into account the presence of human beings, limitations somewhat higher than the appropriate ones are imposed on maximum acceleration. In particular, it was possible to set the acceleration exposure limits at those valid for emergency entries. Assuming that the sideslip angle is always null, the only components of acceleration in body axes are along G_x and G_z directions. At any instant of time, the descent trajectory has to verify the following relations:

$$a_{x,min}(t) < a_x(t) < a_{x,max}(t) \quad (5.19a)$$

$$a_{z,min}(t) < a_z(t) < a_{z,max}(t) \quad (5.19b)$$

These constraints are enforced only on the first phase of the descent, from the entry in the atmosphere to the deployment of the first parachute. In fact, apart from events as the deployment of the decelerators and the landing, which provoke very high but very short duration accelerations, this is the phase characterized by the higher dynamic loads.

5.4.5 Complete architecture

From the analysis of the input/output structures of the disciplinary modules it is clear that the problem presents many couplings and its solution requires an iterative process. In fact, some disciplines necessitate of inputs that are computed by other disciplines and conversely. An illustrative example of this kind of problems is given by the aerodynamics-dynamics interdependency.

For the present investigation, an all-at-once architecture is embraced. A schematic illustration of the software architecture is offered by figure 5.14. A higher level diagram, in figure 5.15, explains how the optimization process is performed. An initial guess for the design variables \mathbf{x}^0 is given to the analysis code, together with the problem inputs; the objective and constraints are computed and passed to the optimization algorithm, which generates a new vector of design variables. This happens iteratively, until a convergence criterion is met; \mathbf{x}^* represents the optimum solution.

5.5 Optimization methods

Optimization solvers can be distinguished in two main classes: local and global. Local methods work successfully in convex problems, for which a locally optimal solution is also a global optimum. In presence of a function characterized by multiple local minima, it is necessary to apply global optimization techniques. This is the case for hard problems as the one here analyzed, for which we do not know the shape of the objective, probably nonconvex with respect to the problem variables.

The algorithms that enable the solution of optimization problems are multiple. Some require the knowledge of the objective function's gradient while others do not, some take inspiration from nature and some even from technological processes. In the following part of the section, a number of global optimization algorithms are presented; for many of them the documentation source is MathWorks website [64].

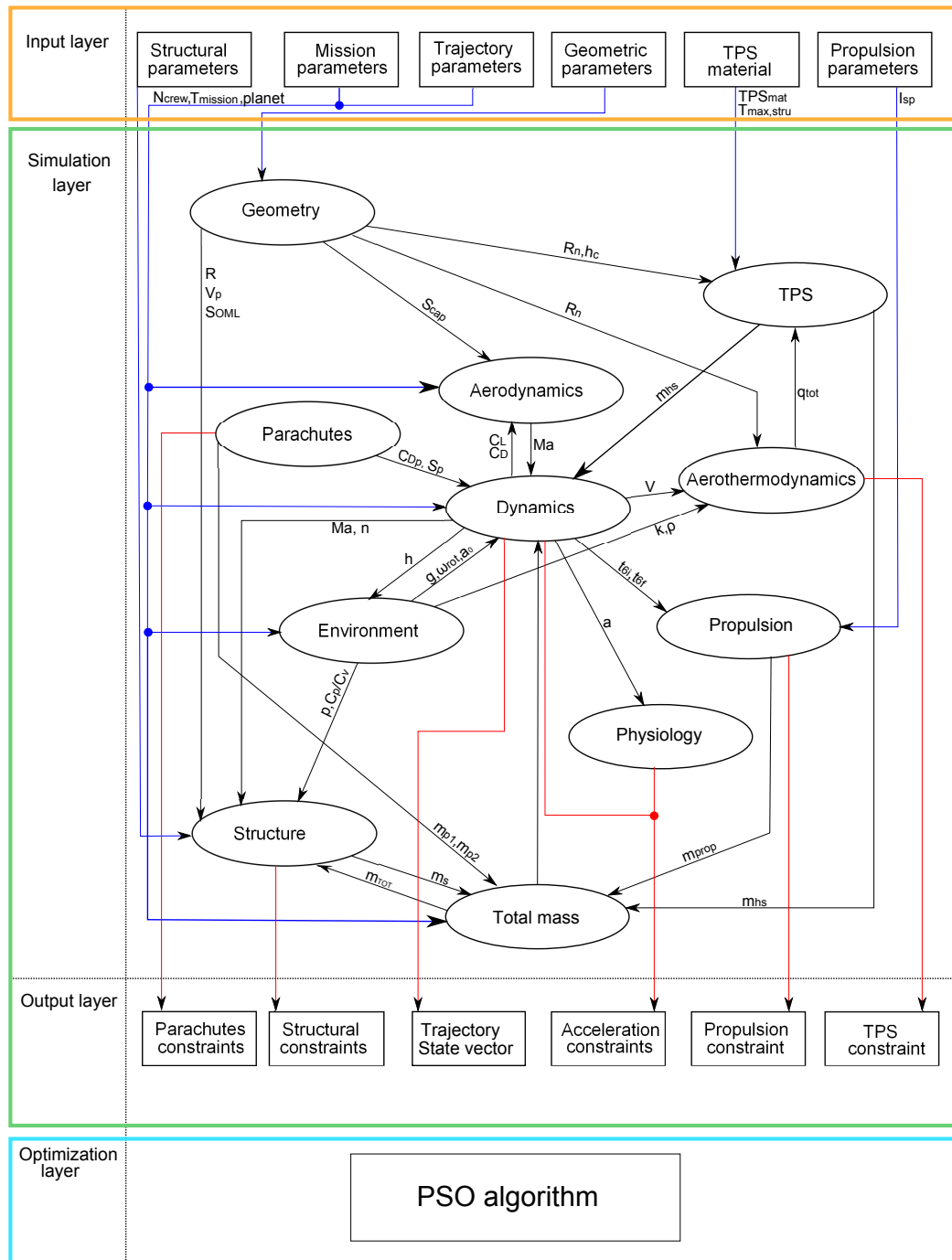


Figure 5.14: Architecture of the software for the optimization of the EDL vehicle and its trajectory.

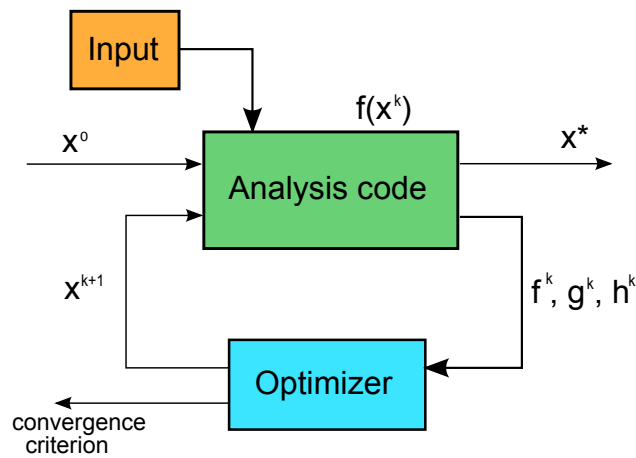


Figure 5.15: Schematization of the optimization process.

Gradient-based methods

Gradient-based global methods exploit gradient-based local methods to find global minima. Global search algorithms run local solvers from multiple start points, in order to explore a wide region of the search space. Some start from uniformly distributed points within given bounds, while others generate initial points by means of the scatter-search algorithm. At any iteration, the points can be filtered to reject those that are unlikely to improve the minimum objective function already found. From each of the remaining points, a local search algorithm is run to find the global optimum (or also multiple local optima). In reason of the structure of the algorithm, these methods are well-suited to parallelization on different processors. The main drawback to their use is that they require the knowledge of the objective function's gradient, which limits substantially their field of application.

Direct search

At each iteration, the direct search algorithm, which is also called *pattern search*, takes into consideration a set of points (called *mesh*) around the current one, according to a *pattern*. This object is a set of vectors \mathbf{v}_j that defines the directions in which the new points are to be selected; it can be fixed or iteratively and randomly determined. The *mesh* is generated by adding to the current point the vector \mathbf{d}_j , obtained by multiplying \mathbf{v}_j by the scalar Δ^m , called *mesh size*. The algorithm then evaluates the objective in the new points, looking for a lower value than that at the current point. If the poll is successful, the point that improves the objective becomes the

current point and the mesh size is multiplied by 2 for the next step; if the poll is unsuccessful, the current point does not change and the mesh size is multiplied by 0.5.

The direct search method can be applied to problems characterized by non-differentiable and even discontinuous objective functions, because it does not need the knowledge of their gradient.

Simulated Annealing

Simulated Annealing (SA) is a probabilistic search algorithm that was inspired by the physical process of annealing, a heat treatment used in metallurgy to decrease defects in a material. When a metal at high temperature is slowly cooled down, its molecules are arranged in a pure crystal, which corresponds to the minimum energy state; if the cooling is too fast, the material ends up in a polycrystalline or amorphous state at higher energy instead.

The SA optimization method was first introduced by Kirkpatrick et al. [65] in 1983 as a method to solve combinatorial optimization problems and has later been extended to continuous global optimization problems, as in Locatelli [66]. At each iteration in the SA algorithm, a candidate point in the search space is generated in a random way. The decision on whether to move to this new position or stay in the current one is driven by a probabilistic mechanism controlled by a parameter called *temperature*, in analogy with the physical process. Although points with lower energies (or values of the objective function) are preferred, points that raise the objective are also accepted with a certain probability to avoid being trapped in a local optimum. The probability of making this transition depends on the energies of the current and new states and on the temperature: $P(e, e', T)$. T is initialized with a high value and is gradually reduced at each step, approaching $T = 0$ towards the end of the optimization: in this way, the state space is extensively explored in the first steps ignoring the details of the objective function; towards the end of the process, the search space exploration narrows and the systems moves to the optimum.

If the SA algorithm is run for a sufficient amount of time, it will ultimately lead to the global optimum of the system. This method does not require that the functions be continuous nor differentiable, therefore it is often used for discrete search spaces. However, SA does not handle constraints other than upper and lower bounds and is therefore not well-suited to the problem at hand.

Genetic Algorithm

Genetic Algorithms (GAs) belong to the class of evolutionary algorithms, which find solutions to optimization problems by using mechanisms inspired by biological evolution, such as reproduction, inheritance, mutation, recombination (also called crossover) and selection. The GA theoretical method was made popular by the work by Holland, summarized in reference [67], and its practical application has been enabled by the increase in computational capabilities of the last decades.

The algorithm starts from a random initial population of candidate solutions (also called *individuals*) and evolves toward better positions in the search space by generating a sequence of new populations. At each step, a pool of *individuals* in the current generation is selected on the basis of their fitness value and a new generation is produced by means of three mechanisms:

- the best *individuals* (*elite*) in the current population are directly passed to the next generation through *selection*;
- *children* are produced through *mutation*, by randomly changing some properties (*genes*) of a single *parent*;
- *children* are produced through *crossover*, by combining the *genes* of a pair of *parents*.

Obtained with this process, the new population is composed of solutions that have sets of properties (*chromosomes*) substantially different from those of the previous generation. Each mechanism is essential for a good exploration of the search space: the first technique enables the algorithm to preserve the best known solutions; *crossover* allows the extraction of the best properties from different *individuals* and their recombination to form better solutions; *mutation* is crucial to maintain a diversified population and search a larger region of the feasibility space.

GAs are well-suited to both constrained and unconstrained optimization problems. They can handle discontinuous, nondifferentiable, stochastic and highly nonlinear functions. The main obstacle to their use is that they are computationally very expensive; moreover, there is the risk to converge to a local optimum instead of the global optimum.

Particle Swarm Optimization

PSO is one of the swarm-based algorithms, which take inspiration from the social behaviour of biological systems as bird flocking, animal herding, fish schooling, ant colonies or bacterial growth. This method was developed

in 1995 by Kennedy and Eberhart, starting from the consideration that social sharing of information among the members of a species provides evolutionary advantages [68]. Since then, it has gained more and more popularity because of its high performance and simple structure. As argued by Eberhart and Shi [69], there are many similarities between PSO and GAs.

In PSO method, a group (called *swarm*) of candidate solutions (called *particles*) moves in the search space with the common intent of finding the most favorable location. The movements of the particles are described by some simple formulae:

$$\mathbf{v}_i^{k+1} = \phi^k \mathbf{v}_i^k + \alpha_1 \gamma_{1,i} (\mathbf{p}_i - \mathbf{x}_i^k) + \alpha_2 \gamma_{2,i} (\mathbf{g} - \mathbf{x}_i^k) \quad (5.20)$$

$$\mathbf{x}_i^{k+1} = \mathbf{x}_i^k + \mathbf{v}_i^{k+1} \quad (5.21)$$

where \mathbf{v}_i^k and \mathbf{x}_i^k are the velocity and position of the particle i at the k -th generation, for $i = 1, 2, \dots, N_p$ where N_p is the number of particles in the swarm; \mathbf{p}_i is the particle's personal best known position while \mathbf{g} is the global best known position; ϕ represents the particle's inertia; α_1 and α_2 are acceleration constants, while $\gamma_{1,i}$ and $\gamma_{2,i}$ are uniformly distributed random values between 0 and 1, for the i -th particle.

As it is evident from equation 5.20, the movement of a particle is driven by three contributions: the inertia that tends to keep the particle on its current path, the attraction toward the individual best known position and the attraction toward the best known position in the swarm. These components are sketched in figure 5.16, respectively referred to as *inertia*, *memory* and *group*.

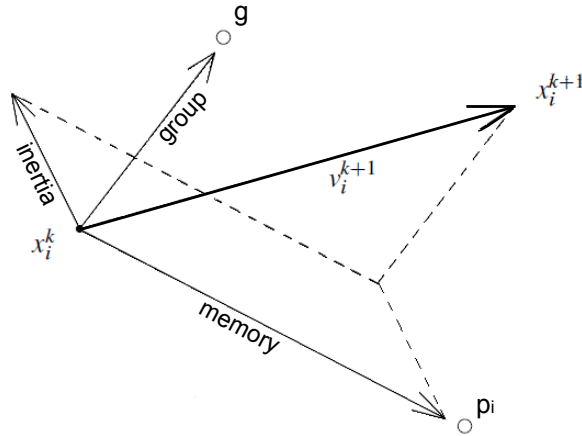


Figure 5.16: Visual interpretation of PSO algorithm.

The constraints can be handled in one of the following ways, illustrated in figure 5.17 [70]:

- the particles that violate a constraint are penalized by being assigned a high objective function value;
- the particles that would exit from the constraint boundaries are absorbed on the boundary of the feasible region;
- the particles that would exit from the constraint boundaries are placed on the nearest constraint.

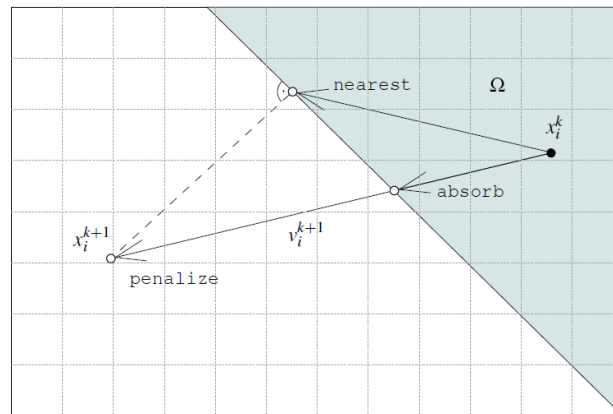


Figure 5.17: Visual interpretation of PSO constraint handling methods.

PSO does not guarantee that an optimal solution is found. On the other hand, it can search very large spaces of candidate solutions and does not require the knowledge of the objective function's gradient. Since it does not need the optimization problem to be differentiable, it can be successfully employed for irregular and noisy problems. Furthermore, this method can handle a nonlinear fitness function and multiple linear and nonlinear constraints.

Chapter 6

Simulations and results

The most important thing we can do is inspire young minds and to advance the kind of science, math and technology education that will help youngsters take us to the next phase of space travel.

John Glenn

First American astronaut in orbit.

This chapter presents the performed simulations and the obtained results. The first section explains the choices made for the software creation and execution and those regarding the optimization algorithm. The results of the simulations are then presented and discussed. Multiple levels of detail are adopted for the analysis: first, the outcome of different optimization runs is reported; second, the general features of a single but complete optimization are examined; third, some details of an optimum solution are analyzed. In the final part of the chapter, some considerations are made on the accomplishments and limitations of the present investigation.

6.1 Simulations

The entire design and analysis tool was developed in Matlab environment, which offers multiple capabilities beneficial to the success of the project. Matlab allows for the generation of the disciplinary models, the integration of Ordinary Differential Equations (ODEs) and the effortless management of the interconnections between the modules. Moreover, it provides accessible optimization capabilities and its use is widespread in the scientific community.

The simulations here presented are the product of multiple intermediate optimizations that allowed to verify the correct operation of the tool progressively built; these preliminary analyses are omitted for shortness sake. All the simulations refer to the Earth as the planet where the reentry occurs, even though the code is conceived as flexible. Many selections have already been made in the conception of the disciplinary modules: the materials for the structure and the TPS, the type of the parachutes and of the retrorockets, the trim angle of attack, the capsule geometry, the employed launcher. Two more important parameters are fixed for these simulations:

$$N_{crew} = 3 \quad (6.1a)$$

$$T_{mission} = 6 \text{ days} \quad (6.1b)$$

The size of the crew is typical of a mission to the Moon or to the ISS; the mission duration is set to six days because an estimation of the needed ECLSS mass for the CM (which has to be known for the computation of the total mass) is given by Larson and Pranke for these specifications. They envisaged a round trip to the Moon and evaluated the ECLSS to be around 600 *kg*.

The lower and upper bounds for the design variables, the chosen objective and the imposed constraints were explained in detail in chapter 5.

The optimization is implemented by means of the PSO algorithm, that combines flexibility with appreciable performance [15]. Although this optimization method is not included in Matlab Global Optimization Toolbox at the time of writing, a generic Particle Swarm Optimization Matlab function is provided by the researchers of the Institute for Dynamic Systems and Control of ETH Zürich [71]. This version of the algorithm is particularly easy to use because its syntax is consistent with that used for Matlab built-in optimization functions; furthermore, it is accompanied by some published documentation presenting the syntax and demonstrating the proficiency of the function [70].

The most important settings used for the PSO algorithm are gathered in table 6.1. Some are kept fixed for all the simulations, while others vary from a simulation to the next one. The selected number of particles N_p is a compromise between the need for a sufficient search of the design space and a reasonable initialization and computational time. The iteration is terminated when some criteria is met, typically when a certain precision in the value of the objective function is reached, or after a given number of generations, or if the process of optimization is stalled. The tolerance on the fitness value

Table 6.1: PSO settings for the performed simulations.

Simulation	N_p	N_{stall}	N_{max}	ε_f	ε_c	Constraints handling method
1	36	150	1000	0.1	1×10^{-6}	Penalize
2	50	200	1000	0.1	1×10^{-6}	Penalize
3	50	200	1000	0.1	1×10^{-6}	Penalize
4	60	200	1000	0.1	1×10^{-6}	Penalize

ε_f is set to 0.1 kg , because we do not need high precision on the value of the total mass of the system at a preliminary stage of the project. On the other hand, the acceptable constraint violation ε_c is very low because we really want the solutions to be feasible. The maximum number of generations N_{max} is fixed while the stall generation limit N_{stall} depends on the simulation. This quantity is the maximum number of generations for which the fitness value is allowed to change less than the admitted tolerance: after this number of generations the algorithm is judged as stalled and is terminated. In the preliminary simulations it was observed that the objective function often reaches a *plateau* and improves again only after a certain number of generations; a sufficiently high value of the stall generation limit prevents the optimizer from stopping too soon. Finally, the method used to handle the constraints is the same for every simulation: a high objective function is assigned to the non feasible particles (those that do not verify the constraints).

The swarm for the first simulation is partially initialized by hand. Even though this does not guarantee a homogeneous distribution of the particles in the search space, it was necessary because of the difficulty of the problem. In fact, the PSO optimizer proved itself unable to find autonomously an acceptable number of feasible initial particles in a reasonable time. A first attempt to overcome this obstacle was to manually select 12 feasible particles. In order to increase the size of the swarm, two vectors δ_1 and δ_2 of small increments or decrements of the design variables were defined and summed to the initial set of 12 particles, so as to create 36 particles that are inside or in the proximity of the feasible space. Simulations number 2 and 3 were initialized by randomly selecting 50 particles among those that the first simulation found to be feasible. For the initialization of simulation number 4, a mixed approach was employed: 36 particles were selected by hand as for simulation number 1, while the remaining amount was composed of random but feasible particles as for the second and third simulations.

Table 6.2: Computational time for the simulations.

Simulations			
1	2	3	4
<i>2 h 1 m</i>	<i>3 h 1 m</i>	<i>3 h 14 m</i>	<i>4 h 6 m</i>

6.2 Results

6.2.1 Comparison of multiple optimizations

The results of the four successive simulations are here presented and discussed. This section compares and critically analyses the values of the objective function, the mass distributions, the optimum solutions and the profiles of the most meaningful quantities in time.

The first difference that can be expected among the performed simulations concerns the computational time. Table 6.2 compares the time that was necessary for the optimizations to converge; these results were obtained with an Intel Core i5-3317U processor. A rough estimation of the computational time required for one integration of the equations of motion from the entry to the touchdown is of 4 seconds. It should be noticed that the optimization process is considerably slowed down by the operation, required for the final critical analysis, of storing many quantities into files at each iteration.

In figure 6.1 the reader can notice that the objective value varies from one optimization to the next one. Generally, one may expect a monotonous improvement of the fitness function as the number of particles of the swarm is increased; in fact the search space can be better explored by a bigger swarm. In the graph it appears that the best solution was found by simulation number 2, which employs 50 particles randomly selected among those found to be feasible by the swarm of simulation number 1. It is interesting to notice that the objective value attained by the third simulation is higher, even though the particles of the initial swarm are found in the same way; this stresses the fact that the outcome of an optimization depends on the individual particles of the initial swarm.

Figure 6.2 details the decomposition of the total mass for the different optimization executions. At a first glance, we can determine the heaviest components: apart from those representing the margin and the sum of the non-modeled subsystems, the ECLSS, the structure and the crew lead the mass budget. While the ECLSS and the crew mass are parameters that re-

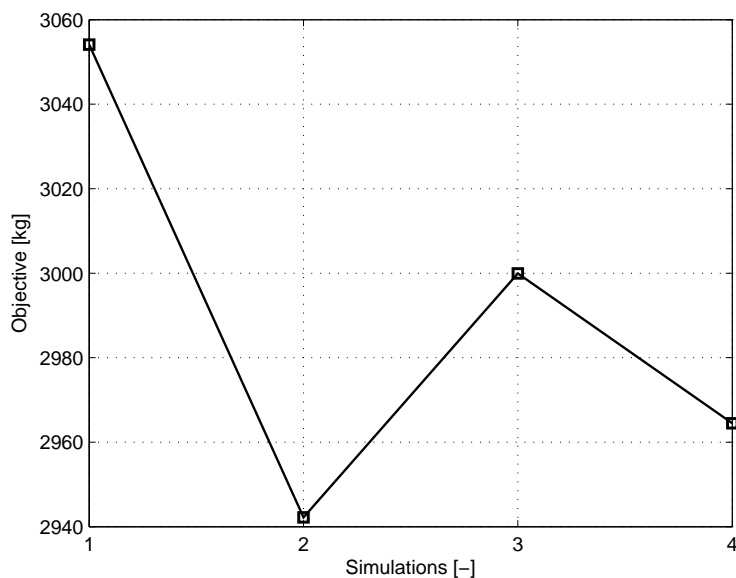


Figure 6.1: Comparison of the objective value for different simulations.

main constant throughout the different simulations, all the remaining components masses vary. The *margin* and *other* components represent the 30 % margin on the total estimated mass and the 40 % increase on the known subsystems that accounts for the non-modeled ones; being originated by percentages, they change coherently. The structural mass is subject to the biggest variation from one solution to the next one; it is the lowest for solution number 2. The main parachute is always more massive than the drogue, and the retrorockets are the heaviest deceleration device. The heat shield is quite lightweight in every solution found.

It is interesting to compare the decomposition of the mass in figure 6.3 to the sizing of the CEV performed by Stanley et al. [39]. The bars in figure 6.3 represent the weights of the subsystems sized for a Lunar CEV CM. The validity of the comparison is limited because the team that designed the CEV considered a bigger vehicle, characterized by a diameter of 5.5 m and a total mass of about 9500 kg , for a crew of four. All the mass quantities are therefore scaled. The margin is in percentage lower for the CEV case, because the designers used 20 %. The non-distincted subsystems form the higher portion of the total mass, followed by the structure. The most visible difference between the two sizings consists in the ECLSS, that was set as a parameter in this study. The structure is correctly higher than the other subsystems, while the heat shield appears to be underestimated. The *decelerators* bar

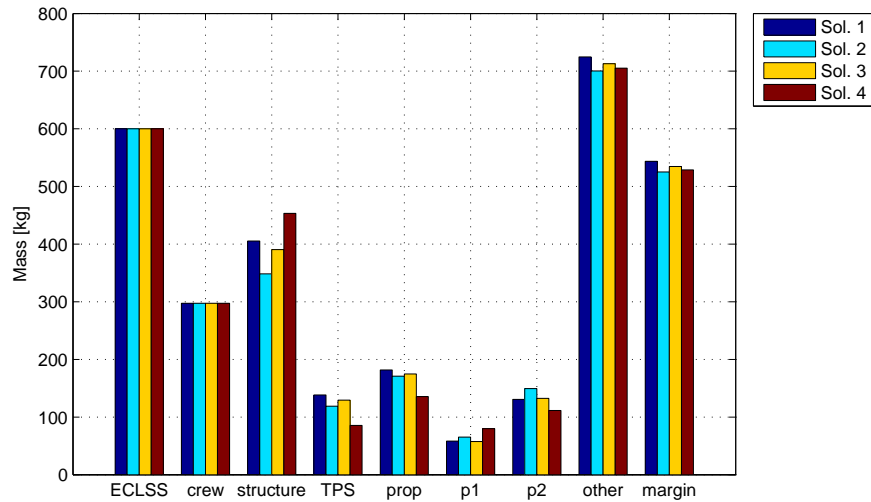


Figure 6.2: Decomposition of the total mass for different simulations.

for the CEV corresponds to the sum of those of the parachutes and the retrorockets in our mass decomposition.

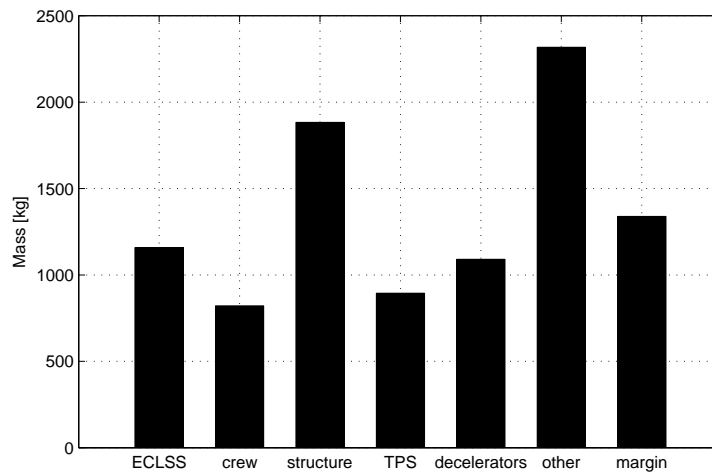


Figure 6.3: Decomposition of the total mass for the CEV.

Table 6.3 collects the optimum solution obtained for each of the executed simulations. The first feature that catches the eye is the similarity among many of the variables. The radius of the capsule is almost exactly the same for all the optimum solutions and takes values very close to the minimum

Table 6.3: Optimum solutions for different simulations.

Variables			Solutions			
			1	2	3	4
Geometry	R	[m]	1.57	1.56	1.56	1.56
Mass	m_{TPS}	[kg]	115.32	99.14	107.88	71.32
	m_s	[kg]	405.45	348.50	390.46	453.25
	m_{prop}	[kg]	181.77	170.85	174.88	135.46
	m_{P1}	[kg]	58.30	65.31	57.54	79.78
	m_{P2}	[kg]	130.73	149.52	132.54	111.32
Initial conditions	V_1^i	[km/s]	6.44	6.12	6.37	6.00
	φ_1^i	[$^\circ$]	-10.32	5.51	12.15	18.23
	θ_1^i	[$^\circ$]	9.60	3.84	10.11	16.67
	γ_1^i	[$^\circ$]	-7.31	-6.95	-7.05	-6.25
	ψ_1^i	[$^\circ$]	9.79	6.99	10.34	19.25
Altitudes of the events	h_2^i	[km]	19.94	20.15	19.94	19.81
	h_3^i	[km]	4.60	4.45	4.59	4.38
	h_4^i	[km]	3.17	3.17	3.19	2.89
	h_5^i	[km]	0.38	0.22	0.40	0.57
	h_6^i	[km]	0.03	0.07	0.03	0.05
Bank angle	σ	[$^\circ$]	12.15	10.14	13.09	22.71
Thrust of the retrorockets	T	[kN]	51.93	37.06	50.36	45.54

allowed to provide sufficient habitable volume. The altitudes of the events are similar too. Entry velocities are low for every solution and coincident to the lower bound for the fourth. The entry flight path angles are always around -6 or -7 degrees. The bank angle is always positive but variable.

Table 6.4 gathers the results obtained by the optimum solutions. A first consideration can be made on the hypersonic ballistic coefficient of the designed vehicles. This quantity, defined as $\beta_v = \frac{m_{TOT}}{C_D A}$, is a measure of the ability of the vehicle to develop aerodynamic resistance in flight. Since the geometry of the vehicle is fixed and the selected radius is practically the same for all the solutions, the only relevant quantity is the mass: the capsule selected by the first optimization (which is the most massive) develops the highest drag in free flight, while that of the second optimization (the lightest one) develops the lowest. From the analysis of the other results some common features of the solutions become manifest. The analysis of the instants of time when the maxima are experienced lets us deduce that the maximum heat rate occurs in the free-fall phase, while the maximum load factor corresponds to a parachute deployment. As far as linear sustained acceleration is concerned, it can be noticed that it is more important in x- than in z-direction; since accelerations for solution number 4 are the lowest, this trajectory would be

Table 6.4: Results of different simulations.

Results		Solutions			
		1	2	3	4
m_{TOT}	[kg]	3054.1	2942.2	2999.9	2964.5
β_v	[kg/m ²]	493.0	482.3	491.8	486.0
$\dot{q}_{tot,max}$	[W/cm ²]	81.7	71.2	78.9	67.1
$t_{q_{tot,max}}$	[s]	87.5	92.5	90.0	100.0
n_{max}	[g]	11.3	13.2	11.6	9.9
$t_{n_{max}}$	[s]	682.1	682.1	682.1	681.9
$a_{x,max}$	[g]	8.1	7.7	7.8	7.5
$a_{z,max}$	[g]	5.3	5.0	5.1	4.8
$t_{ax_{max}}$	[s]	95.0	100.0	100.0	110.0
$t_{az_{max}}$	[s]	95.0	100.0	97.5	107.5
Ma_{max}	[—]	23.8	22.6	23.5	22.1
$t_{Ma_{max}}$	[s]	45.0	50.0	47.5	55.0
V_6^f	[m/s]	2.9	1.8	2.4	2.0
$t_{touchdown}$	[s]	806.9	819.5	807.9	790.5

more convenient for the return of a crew that is deconditioned by the effects of microgravity. For any solution, the maximum of sustained linear acceleration is experienced soon after the heat rate maximum. Moreover, it can be seen that the trajectories causing the highest Mach number peaks cause the capsule to be subject to the highest thermal loads too. Finally, by examining the velocity at the touchdown V_6^f it can be verified that the corresponding constraint is satisfied and the solution entailing the least hard landing is the second.

Figures 6.4 to 6.13 compare the results of the simulations under analysis. Observing figure 6.4 it is evident that there are multiple ways to optimize the descent of a reentry vehicle in an atmosphere. This is true even though the altitudes at which the EDL events occur are similar for all the optimum solutions, as highlighted in table 6.3. All the trajectories begin with a steep descent and are characterized by a portion where the vehicle reclimbs in the atmosphere, before the deployment of the drogue parachute. The trajectory for the first simulation begins in the steepest way, while the fourth starts following the shallowest path. The steeper the trajectory in the first seconds of the flight, the higher the reclimbing.

Figure 6.5 compares the variation of the flight path angle in time for the optimum solutions. The initial value of the flight path angle explains the

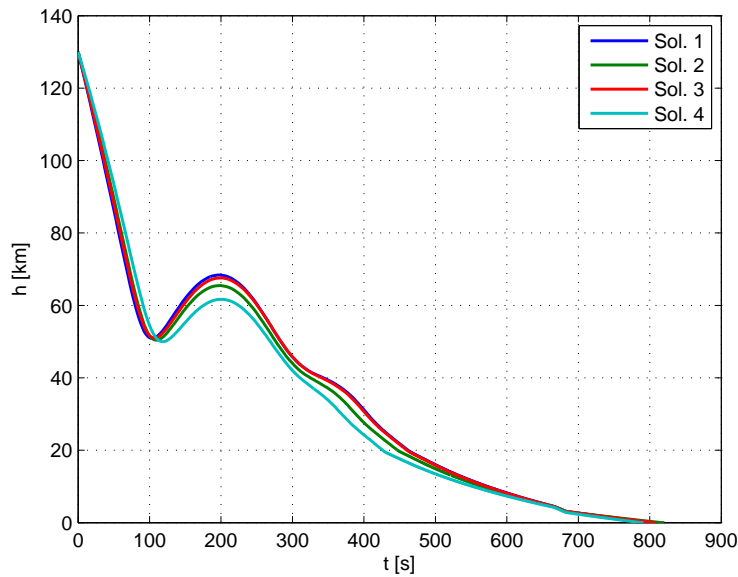


Figure 6.4: Comparison of the trajectory for the optimum solutions.

difference in the inclination of the trajectory in the very first minutes of the flight: the higher the modulus of this angle, the steeper the trajectory. In the case at hand, the initial flight path angle for the fourth solution is the lowest in modulus; the consequence of this is the abovementioned less steep descent. This is reasonable, since the flight path angle is defined as the angle between the velocity vector (the instantaneous direction of motion) and the local horizontal plane. The relationship between the altitude variation and the flight path angle becomes even more explicit if we take into consideration the phases in which the vehicle gains altitude: as it can be seen in the figures, these situations occur when γ is positive. A final consideration is that the flight path angle approaches -90° for every solution, suggesting that in the last phases of the flight the system falls almost vertically toward the planetary surface.

The velocity profile in time is shown in figure 6.6. On the left, we can note a decrease in the slope of the curve, that corresponds to the period of time in which the capsule reclaims in the atmosphere. On the right, the parachute deployments are highlighted with squares and triangles. The most important difference lays in the effect of the drogue parachute deployment: the loss of velocity is always abrupt but higher for the fourth solution. Since the type of the parachute is the same and the altitude and velocity at the deployment are very similar, this discrepancy can be explained only by the

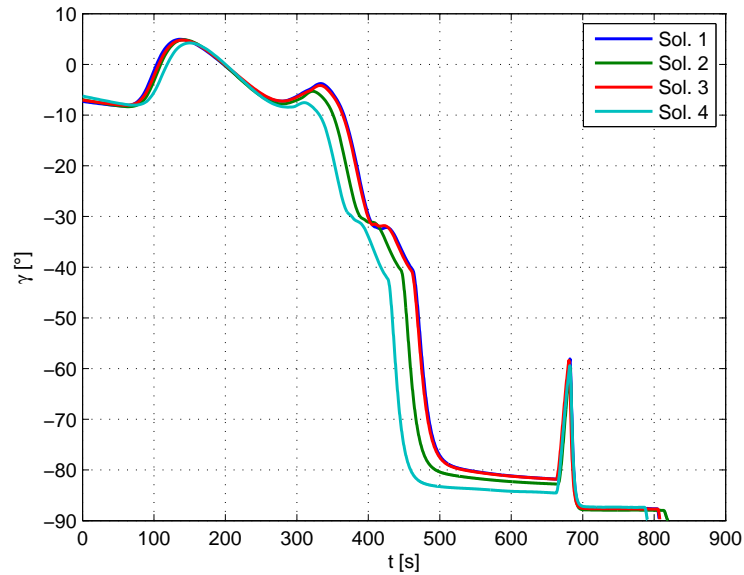


Figure 6.5: Comparison of the flight path angle for the optimum solutions.

difference in the area of the canopy.

The plot in figure 6.7 combines the information on the altitude and the velocity. A characteristic and common feature is the *hill* that corresponds to the reclimbing. In the right-hand plot the detail of the parachute deployments is presented. As it can be seen, for all the solutions the best condition for the deployment of the drogue parachute coincides with the minimum Mach number constraint; even more peculiar is the fact that all the trajectories arrive to this condition with very similar altitude-velocity combinations. As for the main parachute, the best deployment conditions are not identical but once again grouped in a very restricted area of the $h - V$ space. The bottom graph portrays the detail of the last 80 meters of the descent, confirming that solution number two is the one granting the softest landing.

For sake of completeness, figures 6.8 and 6.9 report the variations in time of the latitude, longitude and heading angles. These quantities are of no particular interest in the present study, since no landing precision objective has been defined. The only remark that is worth doing is that the heading angle (defining the orientation of the velocity on the horizon) is of little meaning when the flight path angle approaches the vertical.

The Mach number and total heat rate variation in time are depicted in figurea 6.10 and 6.11. It can be observed that the qualitative position of the lines is the same in the two graphs: solutions characterized by higher peaks

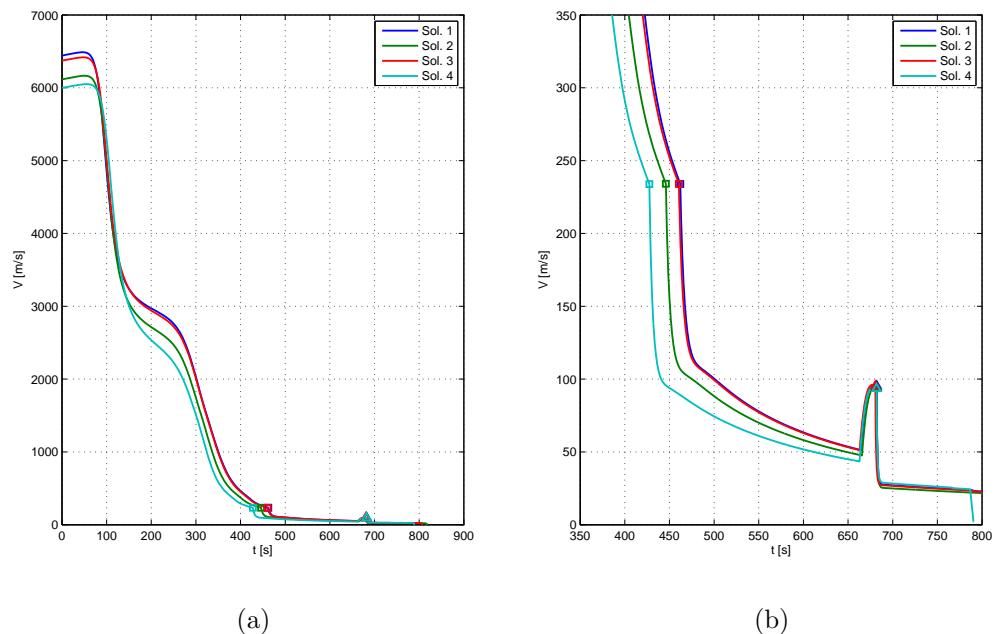


Figure 6.6: Comparison of the velocity for the optimum solutions.

of the Mach number also produce higher stagnation point heat loads. Note also that the heat rate matches the results depicted in figure 6.2, which shows that the first solution heat shield is the heaviest and the last one is the most lightweight.

Another characteristic quantity of the EDL is the load factor. As it can be seen in figure 6.12, the load factor reaches disparate maximum values in the different EDL solutions. The peculiar feature of this profile is the presence of multiple shocks, which are due to variations of the configuration. Particularly evident is the effect of the parachutes deployment, that is also matched by the steep decrease in the velocity that can be seen in figure 6.6. The first solution appears to be the most demanding in the first phase, but the worst load factor for the deployment of the main parachute corresponds to the solution obtained by the second simulation.

Finally, the sustained linear accelerations that the crew would be subject to during the descent are compared in figure 6.13. Only the profiles for the first phase of the descent are reported. First of all, it is important to verify that every profile satisfies the requirements dictated by the human physiology. Both the acceleration along the x-axis, on the left, and along the z-axis, on the right, present well-defined peaks; however, the acceleration is

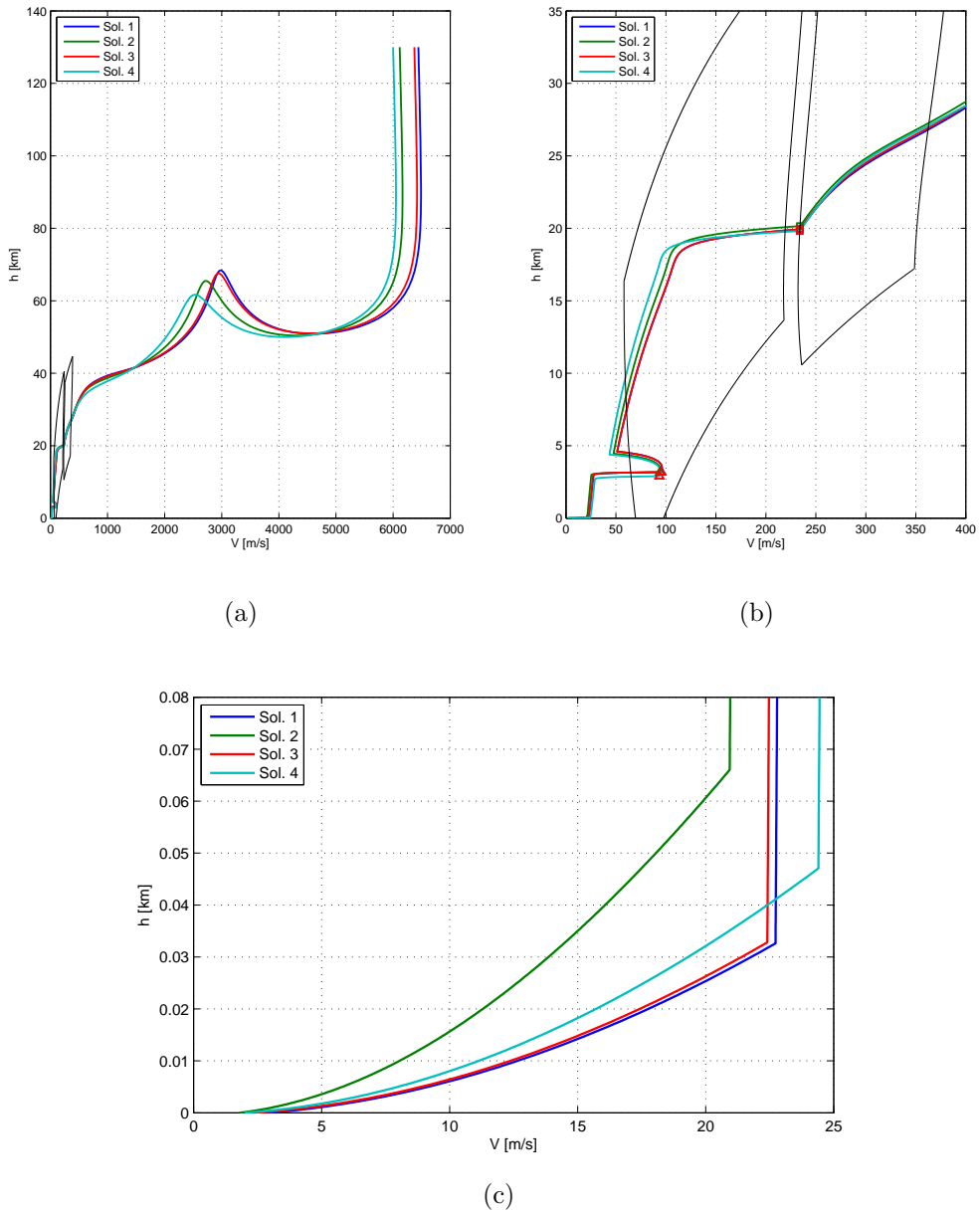


Figure 6.7: Variation of the velocity with altitude for the optimum solutions.

always within the allowed limits. Solution 1 is the most demanding, while solution 4 in the free fall is the most tolerable. As previously said referring to table 6.4, the peak of the acceleration is experienced soon after the total heat rate peak for any solution.

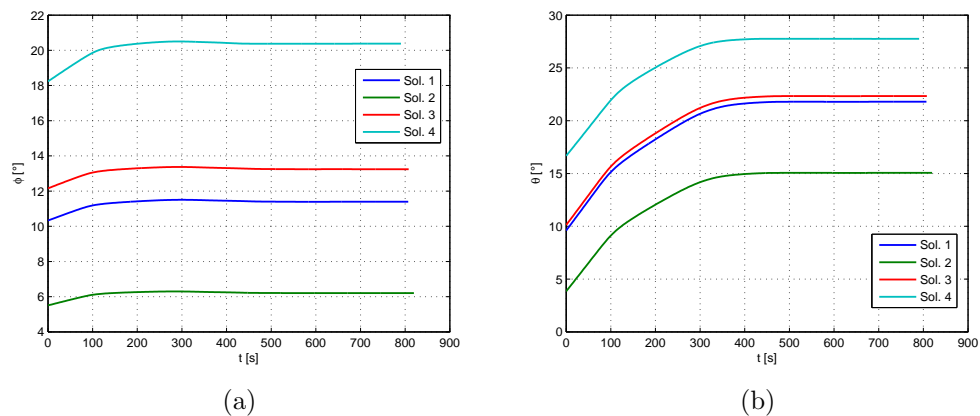


Figure 6.8: Variation of latitude and longitude for the optimum solutions.

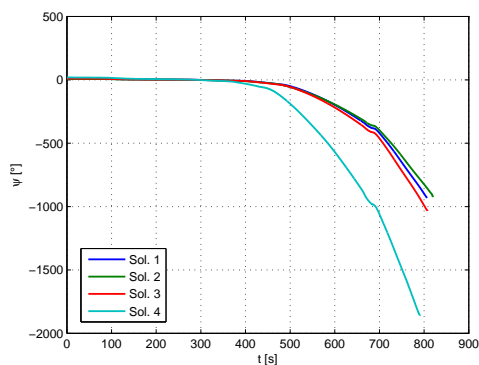


Figure 6.9: Variation of the heading angle for the optimum solutions.

6.2.2 A complete optimization

This section discusses the results of a complete optimization run. The simulation under analysis is the first, which is based on a swarm of 36 particles. The overall results for the PSO optimization are reported and commented; the focus is on the interpretation of the objective function improvement and on the distribution of the particles in the design space. The optimum solution is then detailed, justifying the need to employ decelerators, discriminating the EDL phases and identifying the sequence of the characteristic events.

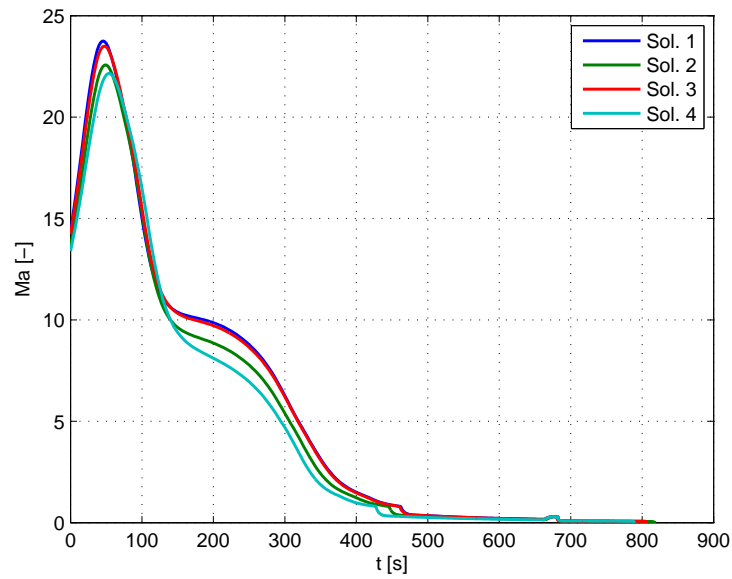


Figure 6.10: Variation of the Mach number for the optimum solutions.

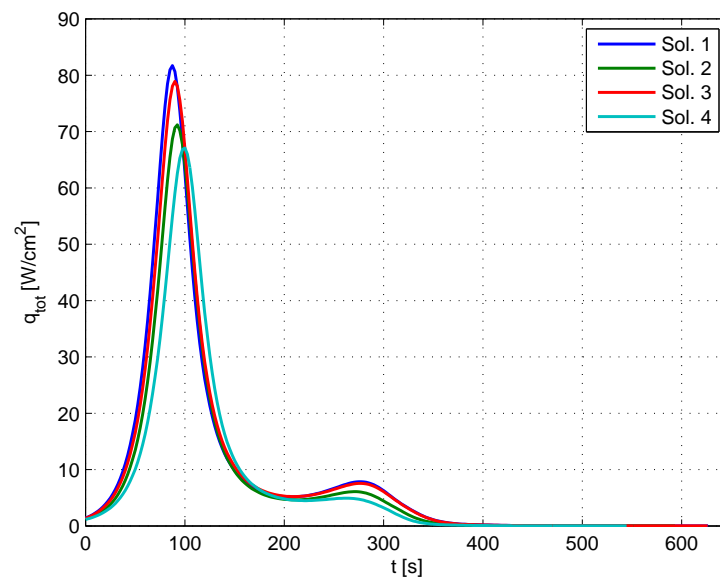


Figure 6.11: Variation of the total heat rate for the optimum solutions.

PSO

Figure 6.14 shows how the objective function varies with the number of generations. The 36 grey lines composing the graph represent the personal

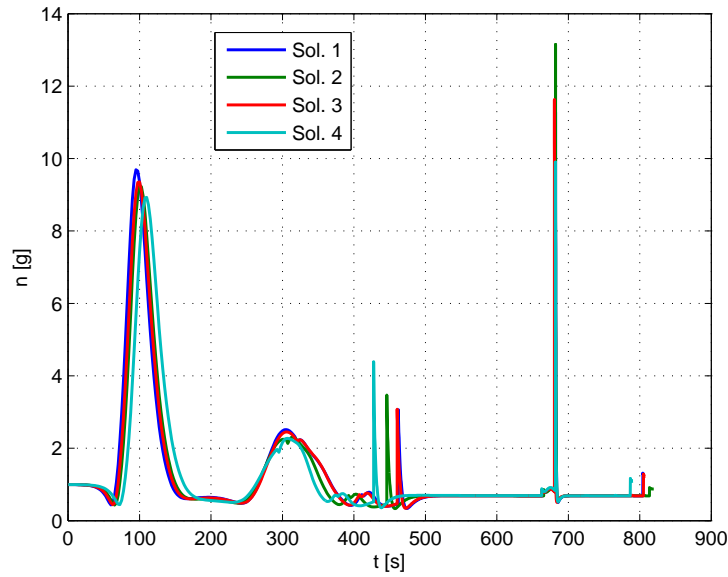


Figure 6.12: Comparison of the load factor for the optimum solutions.

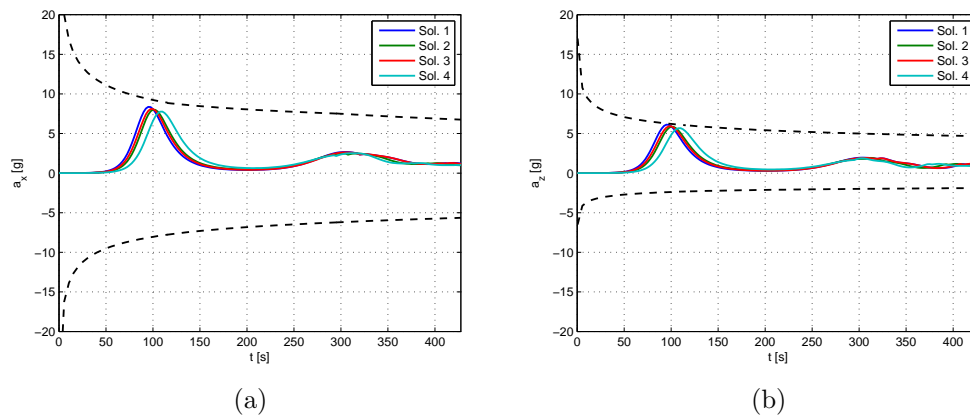


Figure 6.13: Variation of acceleration for the optimum solutions.

best value of the objective for each particle at every generation. The minimum, maximum and mean objectives among the swarm are highlighted. It can be seen that all of these quantities remain constant or diminish as the generations augment. The improvement of the minimum objective value suggests that the swarm is able to explore more convenient regions of the search space as the time passes and information is collected and shared. It can be observed that the maximum value of the objective function remains

constant; this implies that some particles remain in poor quality regions of the search space. The mean of the best personal values of all the particles in the swarm is enhanced as the generations pass, fostering the idea that more and more particles at each generation have approached the minimum. These conclusions are supported by the fact that the grey lines thicken towards the low part of the graph, approaching the minimum; nonetheless, some keep staying in the upper parts of the plot, indicating that a few particles do not move toward better positions during the optimization.

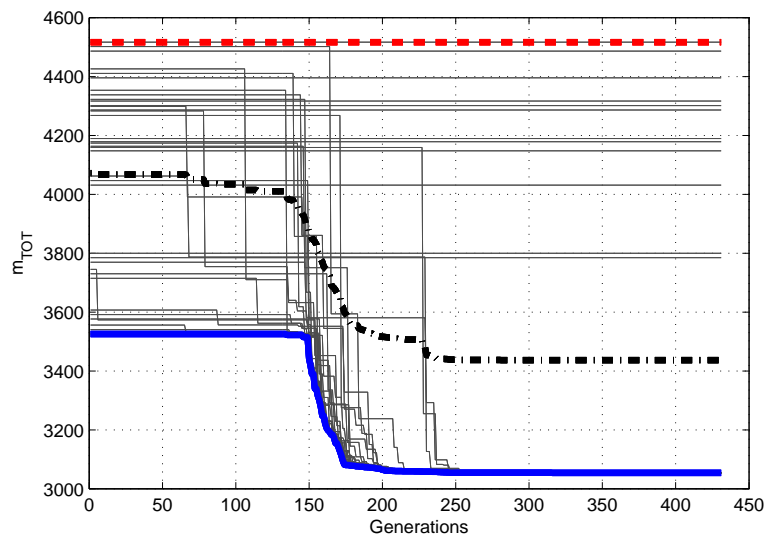


Figure 6.14: Variation of the objective function with the number of generations.

A different way to evaluate the distribution of the objective values in the swarm is proposed in figure 6.15. In this graph, the reader can observe how many particles at each generation provide best personal fitness values in certain ranges. Blue areas indicate low values of the objective, while red ones designate high values. In the first generations the distribution is more or less homogeneous and no particle has experienced particularly low objectives; on the other hand, towards the end of the optimization process most particles are characterized by very low best personal values of the fitness function. Anyway, even in the last few generations many particles exhibit very bad objective values; this suggests that the solution may be improved with a higher number of particles or by allowing a higher number of stall generations.

In order to gain a better insight into the process of optimization it is

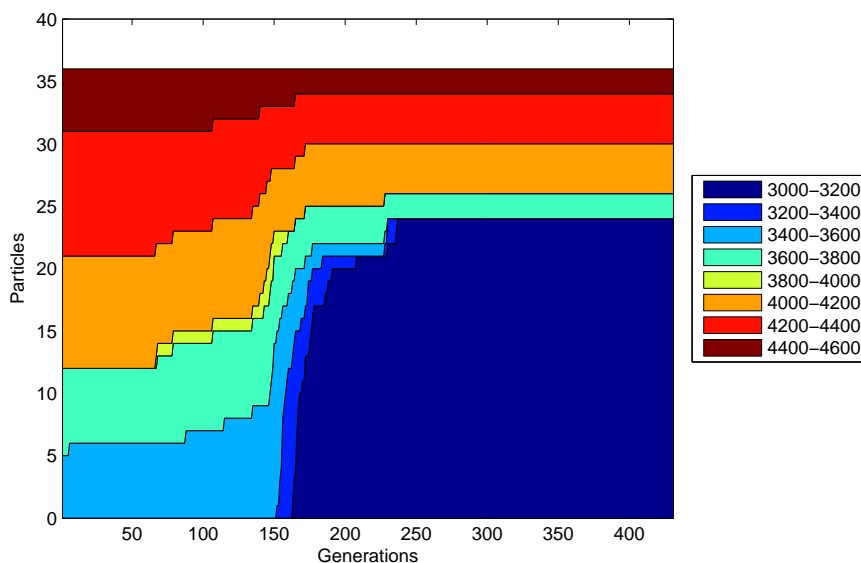


Figure 6.15: Distribution of the fitness function value in the swarm.

important to evaluate the quality of the search of the design space. Figures 6.16 to 6.22 report the distribution of the particles for the majority of the design variables, distinguishing those that satisfy the constraints from those that do not. For sake of clarity, the x-axis of the diagrams is limited by the upper and lower boundary values for each variable.

The module of the entry velocity V_1^i and the radius of the capsule R appear to be clustered at the lower boundary of their domain; however, a sufficient search of the lower part of the search space is granted. A good distribution is obtained for the bank angle σ , the altitude of the retrorockets ignition h_6^i and their thrust T . All the mass quantities offer an acceptable search of the design space, even though most particles are grouped in given portions of it. On the contrary, the explored values for the initial flight path angle γ_1^i and the altitudes for the deployment of the parachutes h_2^i and h_4^i result concentrated in a particularly restricted area of their design space.

From an overall examination of the data it emerges that the search space should be further explored, especially for some of the variables; we expect that to be achievable as the number of particles in the swarm is augmented. Another possibility is to set the velocity of the particles so that they are forced to more distant regions. An additional general consideration is that, thanks to the distinction between feasible and unfeasible particles, the difficulty of the problem becomes even more apparent: the regions where feasible particles were identified are far more restricted than those actually explored.

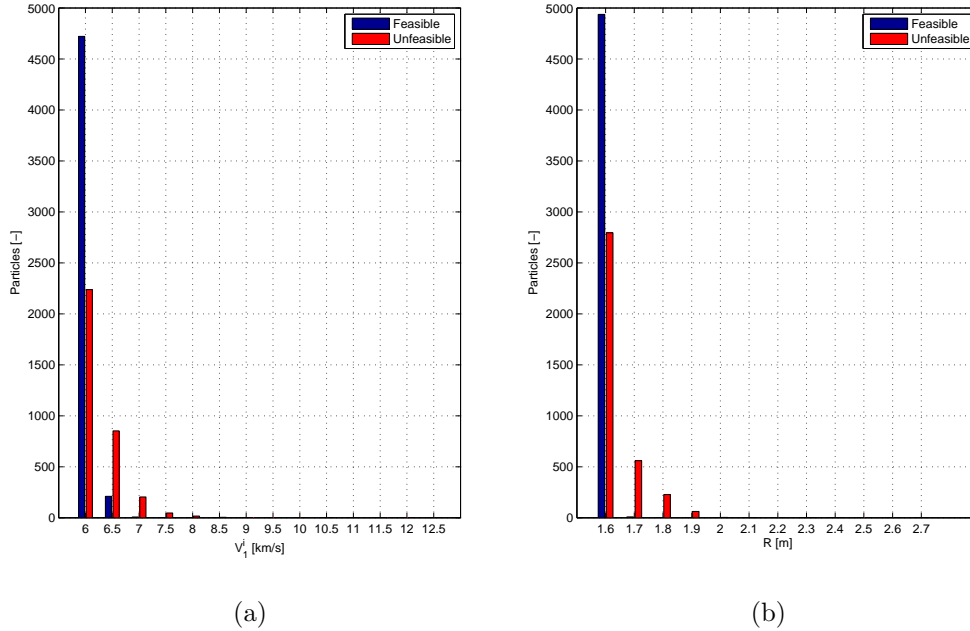


Figure 6.16: Distribution of the particles in the search space for V_1^i and R .

Optimum solution

Figures 6.23 and 6.24 compare the trajectory and velocity profiles of the optimum solution to that corresponding to a free fall. The second descent is computed as the path followed by the same vehicle, starting from the same set of initial conditions, without parachutes or retrorockets. The examination of these curves justifies the claim that it is imperative to use decelerators in the atmospheric EDL of vehicles transporting human beings. In figure 6.23 it is clear that, after the deployment of the first parachute, the capsule loses altitude much more slowly than if it were in free fall. In case no decelerators are employed, the touchdown happens much sooner; at that instant of time the velocity is still too high for the astronauts to withstand the impact with the soil. This is visible in figure 6.24, especially on the right-hand side enlargement of the final phases of the descent: the velocity in free fall would be of about 80 m/s , which is definitely much higher than the aimed 1.5 m/s .

It is interesting to visualize in detail the trajectory of the descent in the atmosphere for the optimum solution found. Figures 6.25, 6.26 and 6.27 show the curves defining the altitude, the velocity and the flight path angle in time. These graphs emphasize the different phases of the descent, which

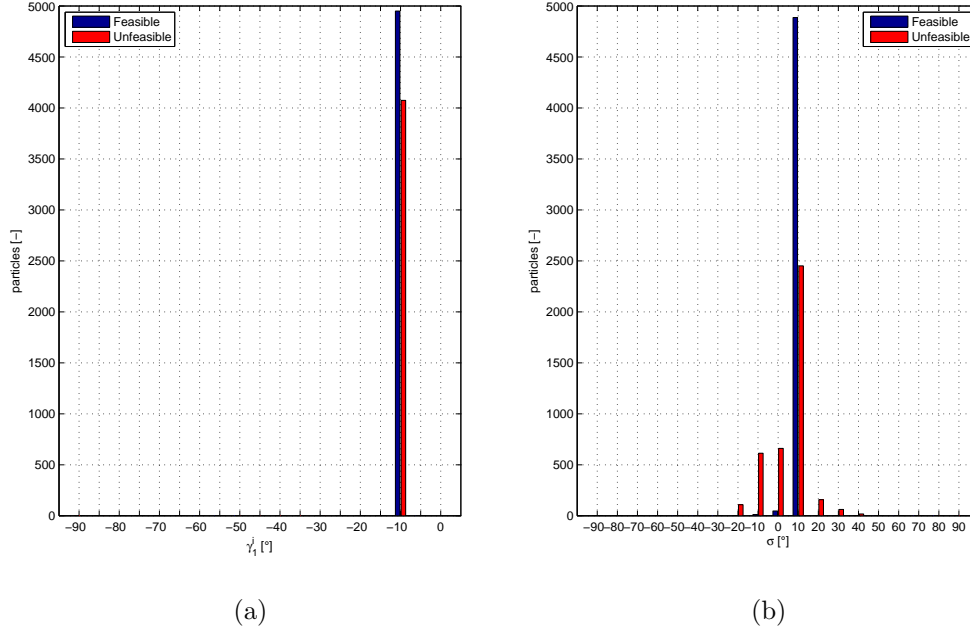


Figure 6.17: Distribution of the particles in the search space for γ_1^i and σ .

are traced with multiple colours. Figures 6.28 to 6.30 display some enlargements of the state variables profiles in time: the graphs to the left specify the occurrence of the characteristic events, while figures to the right detail the last two phases of the descent, soon before the touchdown. In these plots, the effects of the deployment of the parachutes and of the retrorockets ignition is even more evident. When the configuration includes a parachute, the slope of the altitude variation is less pronounced and the velocity falls abruptly; the retrorockets ignition slows the descent and allows for acceptable impact velocities.

Figures 6.31 and 6.32 illustrate the variation of velocity with altitude. In both images the parachute boxes defined in section 4.5 are reproduced. In figure 6.31 it is evident that the conditions for the parachutes deployment correspond to much lower velocities and altitudes with respect to those typical of the entry in the atmosphere; a substantial part of the deceleration takes place in the first phase of the descent, during the free fall of the capsule alone. The expansion of the successive phases of the descent, in figure 6.32, proves the fact that the parachute deployments happen in the feasible subset of the $h - V$ space. In particular, it can be seen that the drogue

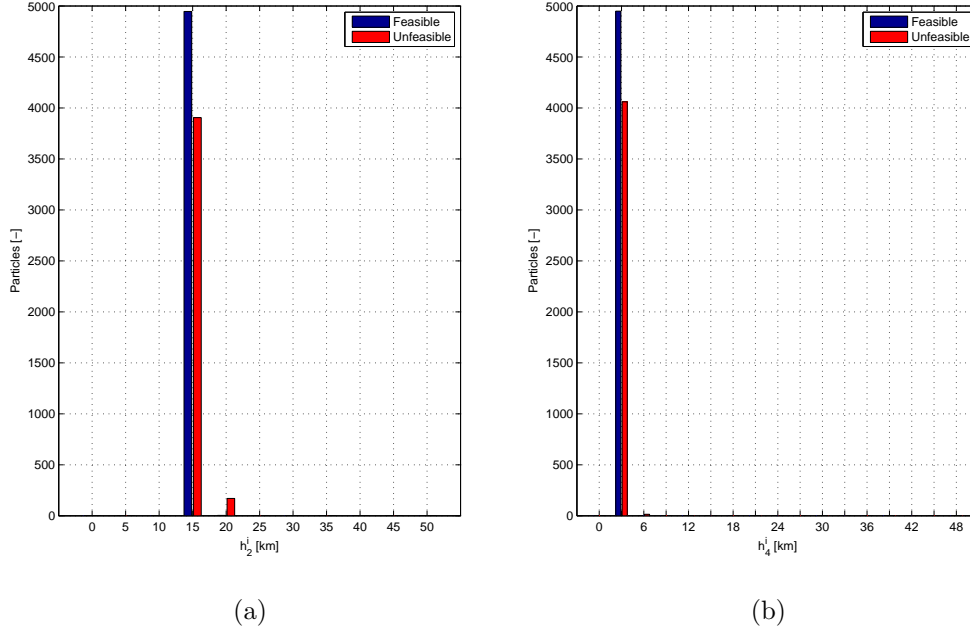


Figure 6.18: Distribution of the particles in the search space for h_2^i and h_4^i .

parachute deployment (marked by a square) happens at the lowest possible Mach number; after that, the trajectory intersects the feasible set for the main parachute and exits from it; when the drogue parachute is released the capsules accelerates and the flight conditions intersect the feasible region again, so that the deployment of the main parachute (marked by a triangle) is possible. Another observation that can be made on these graphs concerns the result of a parachute deployment: it is apparent that just after each of these events the velocity decreases substantially, while the vehicle loses little altitude.

Since acceleration can jeopardize the life of the crew, is worth studying on its profile during the descent. In figure 6.33 the acceleration is decomposed in its x , y , and z components. The same peaks catch the eye for both the x - and z -axis; comparing their magnitudes, it can be observed that all the peaks are more accentuated in the longitudinal direction. The acceleration in y -direction is always null because the sideslip angle, defining the angle between the velocity vector and the $x - z$ plane, always is.

Figure 6.34 provides the plot of the acceleration profile during the whole descent. As it was argued in the previous chapters, it is imperative that the

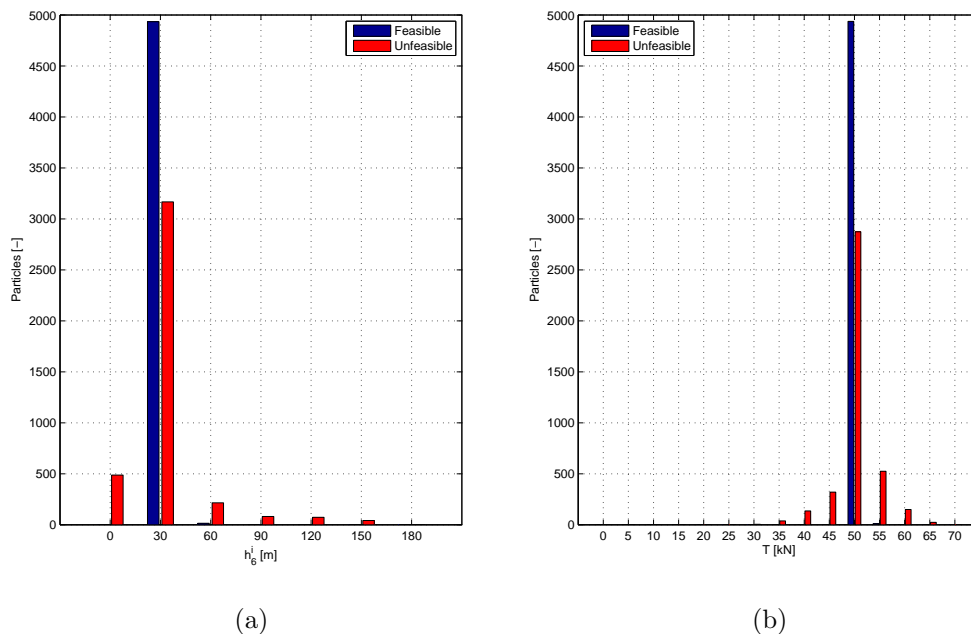


Figure 6.19: Distribution of the particles in the search space for h_6^i and T .

sustained linear accelerations experienced by the astronauts remain below the physiological limits. In reason of considerations made while defining the constraints, the requirements on sustained accelerations are imposed on the first phase only. In the first two figures, it can be verified that these requirements are met by the optimum solution (the solid red curve), which is always within the limits (the dashed black curves). Moreover, we can observe that the maximum sustained acceleration along the x-axis is higher than that in the other direction. This is in agreement with the remark made about the orientation of the astronauts inside the capsule: if they were positioned in such a way that the G_z direction was coincident with the capsule's x-axis, such accelerations could not be tolerated. The plot also depicts the acceleration during the successive phases of the descent. Pronounced peaks are mainly due to abrupt increases and decreases in drag corresponding to changes of configuration. It can be observed that the shock at the deployment of the main parachute exceeds the limits, but its duration is such that human tolerance should be verified separately, with an impact criterion. The last few seconds before the touchdown are enlarged in the bottom figures. Here two interesting details are visible: the heat shield release and the retrorockets burn.

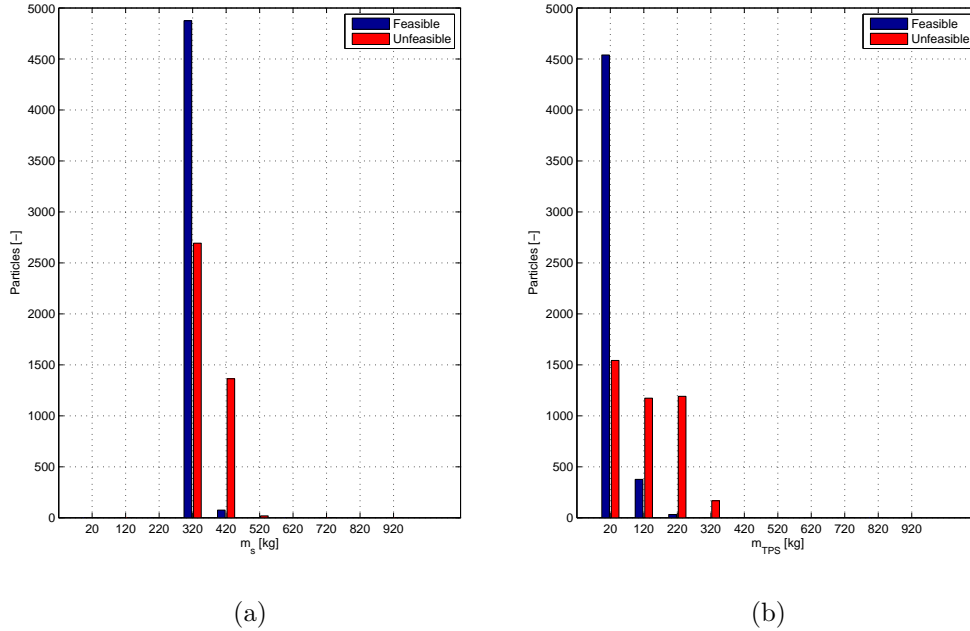


Figure 6.20: Distribution of the particles in the search space for m_s and m_{TPS} .

6.3 Difficulties and achievements

The first difficulty encountered in the research of optimum solutions to the problem at hand concerned the initialization of the swarm for the PSO algorithm. Since the algorithm was not able to select feasible particles autonomously, a procedure for the definition of the first guess swarm had to be conceived. For the first simulation, this problem was solved by manually initializing some of the particles and by creating others through small variations of the design variables vectors. For the following optimizations, the initial swarms included some of the feasible particles of the previous runs. Another limitation was identified while analysing the distribution of the particles in the search of the design space. Because of the limited number of particles that was possible to employ to contain the computational time, the exploration of the search space was not optimal. The particles tend to converge to restricted regions, at least for some variables; to ensure a better exploration of the design space it would be necessary to increase the number

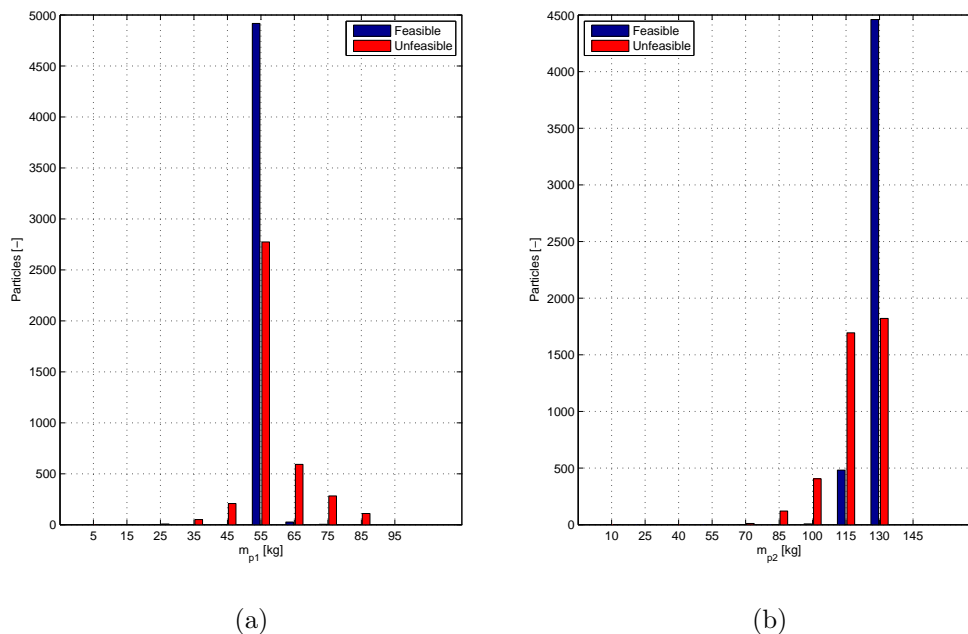


Figure 6.21: Distribution of the particles in the search space for m_{p1} and m_{p2} .

of particles or to impose higher velocities for their displacement in the design space.

Two more considerations can be made on impact accelerations and on the bank angle. The lack of constraints on short duration accelerations deriving from events other than the touchdown can be interpreted as a hazard for the safety of the astronauts; the fact that the bank angle is kept constant during the descent probably limits the possible trajectories. These two weaknesses have opposing effects on the feasibility of the solutions: some trajectories that were found to be feasible could jeopardize the crew survival; on the other hand, the possibility to modulate the bank angle during the descent could enable trajectories that may be characterized by higher accelerations in the first minutes, when the tolerance is higher, and by lower accelerations later.

Whatever the limitations, the results presented in this chapter have demonstrated the validity of the multidisciplinary optimization tool developed for the present research project. The apparatus that was implemented is able to obtain preliminary solutions in a few hours with an average performance laptop. These solutions combine the optimization of the vehicle and of its

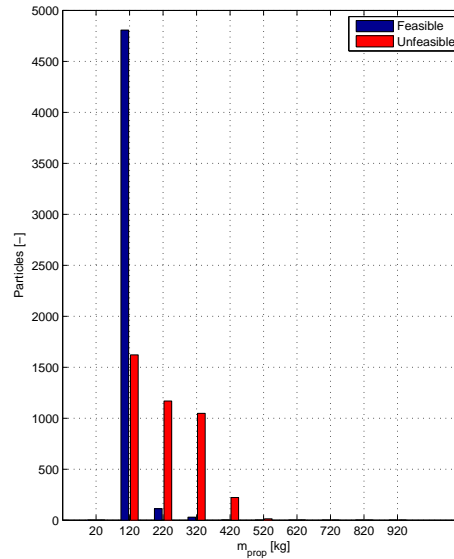


Figure 6.22: Distribution of the particles in the search space for m_{prop} .

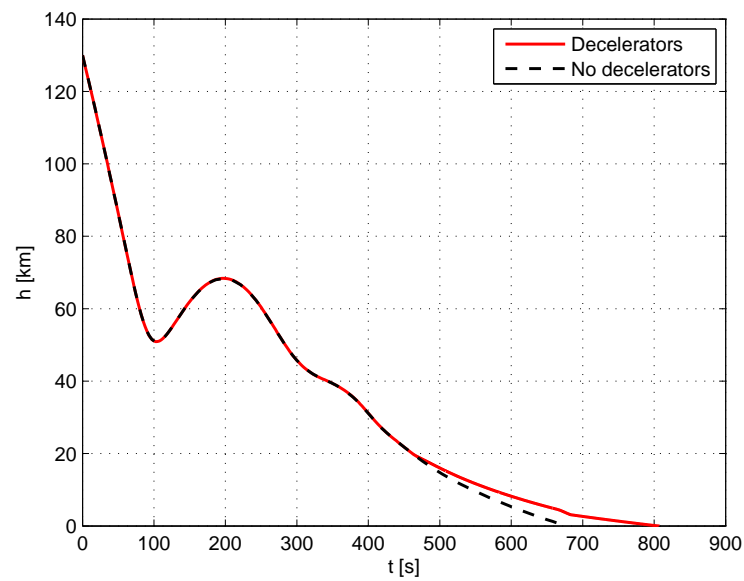


Figure 6.23: Comparison of the trajectory when using decelerators and in free fall.

EDL trajectory and take into account the presence of human beings to some

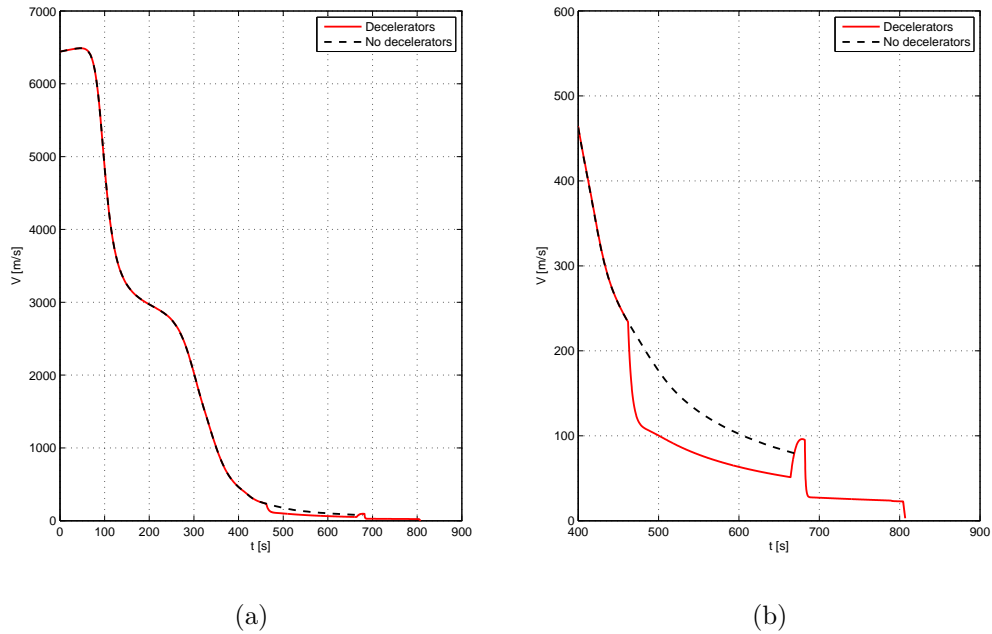


Figure 6.24: Comparison of the velocity when using decelerators and in free fall.

extent.

Multiple distinct solutions for the EDL trajectory were found and permitted a comparative and detailed analysis. Furthermore, even though the performed simulations produced masses substantially different from those reported in a study on the CEV (which assumed bigger dimensions), their distribution and orders of magnitude proved comparable.

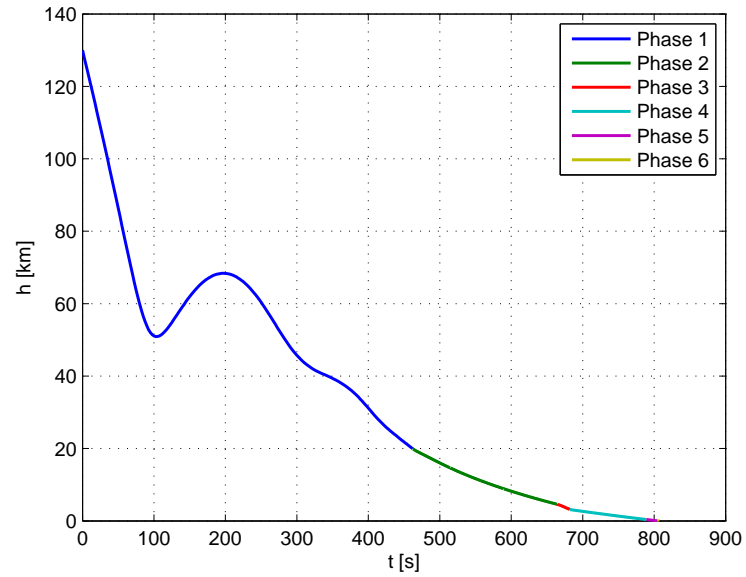


Figure 6.25: Variation of the altitude in time for the optimum solution.

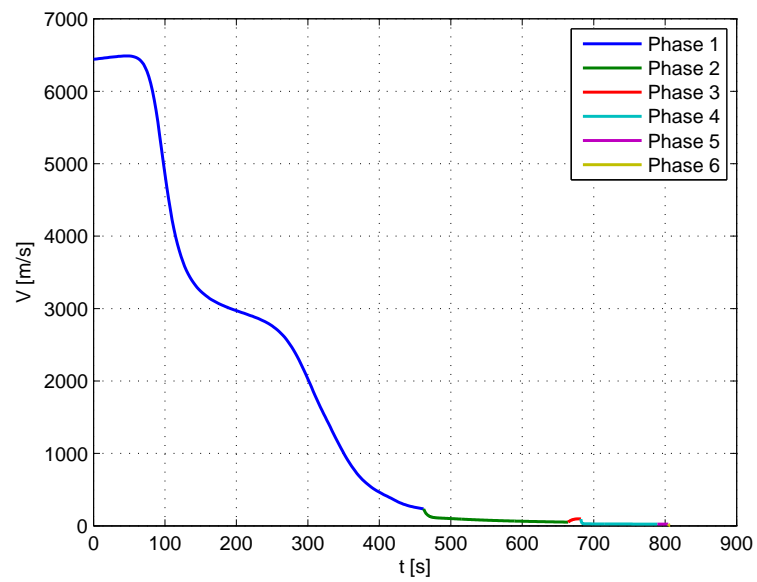


Figure 6.26: Variation of the velocity in time for the optimum solution.

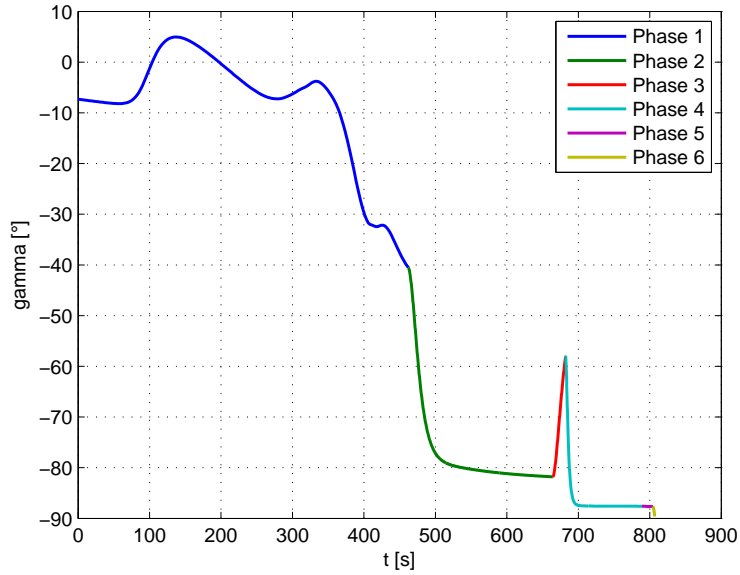


Figure 6.27: Variation of the flight path angle in time for the optimum solution.

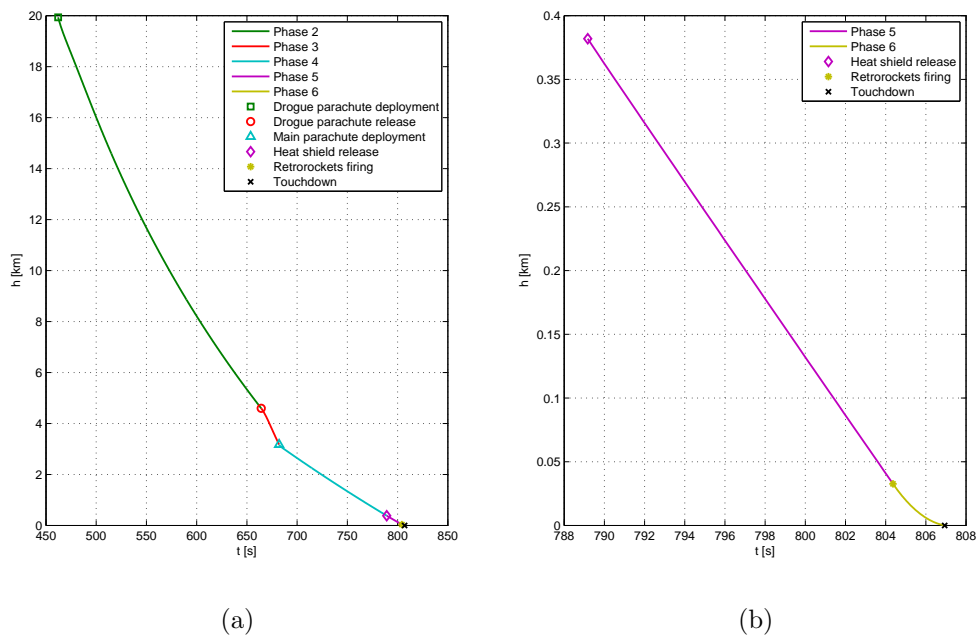


Figure 6.28: Variation of the altitude in time for the optimum solution.

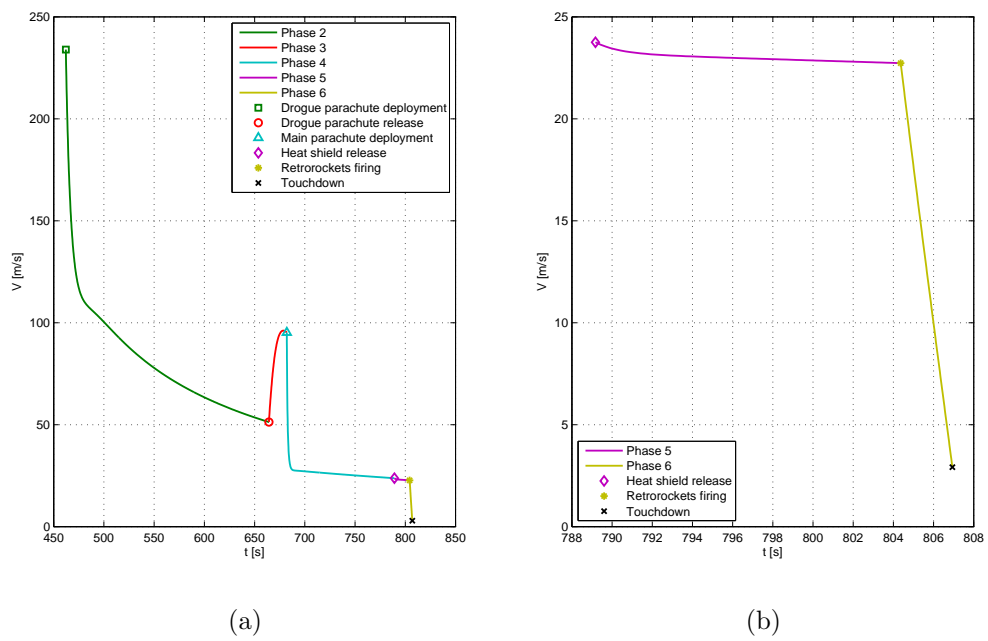


Figure 6.29: Variation of the velocity in time for the optimum solution.

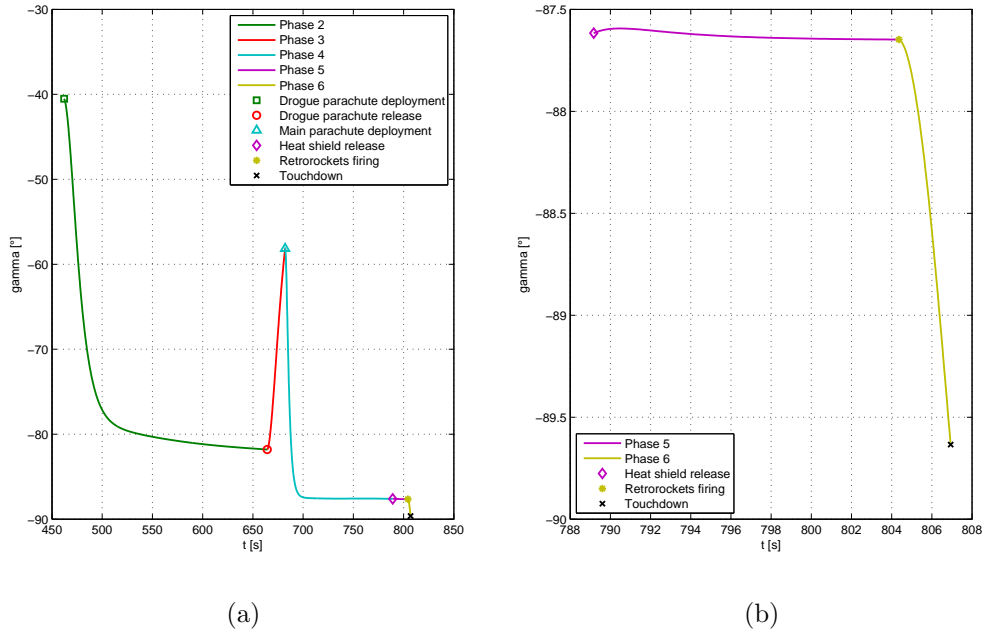


Figure 6.30: Variation of the flight path angle in time for the optimum solution.

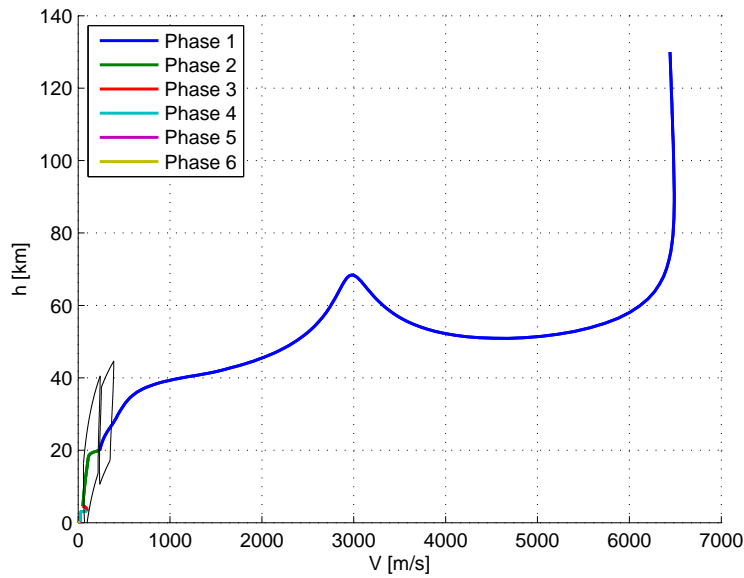


Figure 6.31: Variation of the velocity with altitude for the optimum solution.

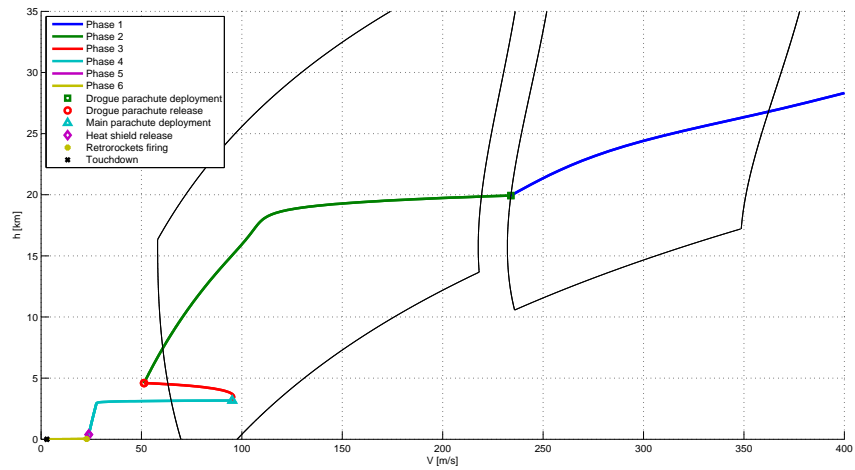


Figure 6.32: Variation of the velocity with altitude for the optimum solution.

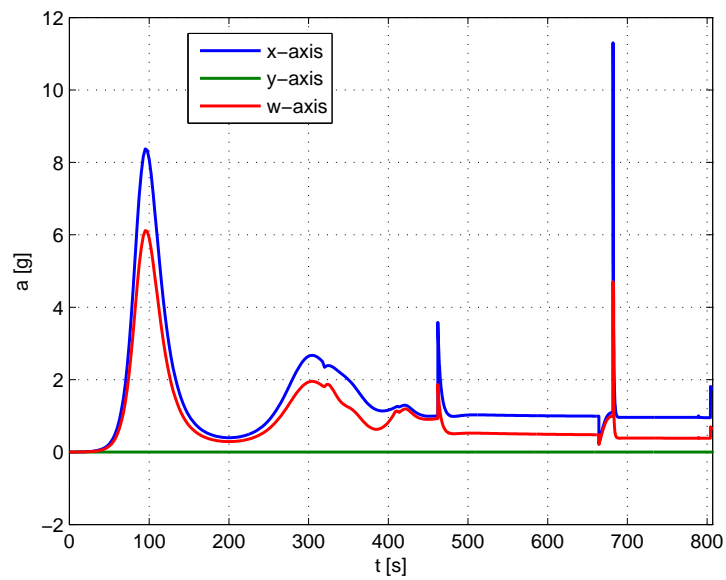
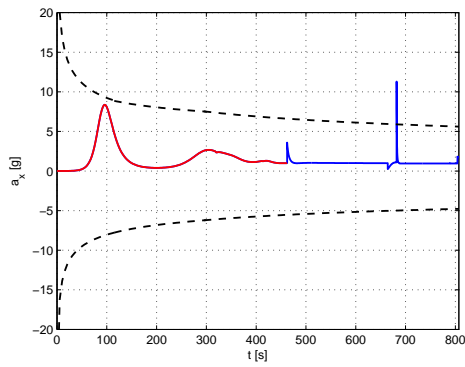
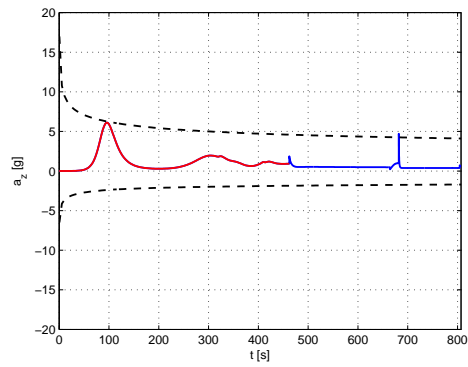


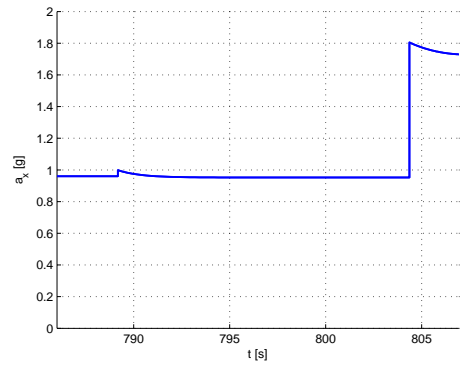
Figure 6.33: Acceleration profile for the optimum solution.



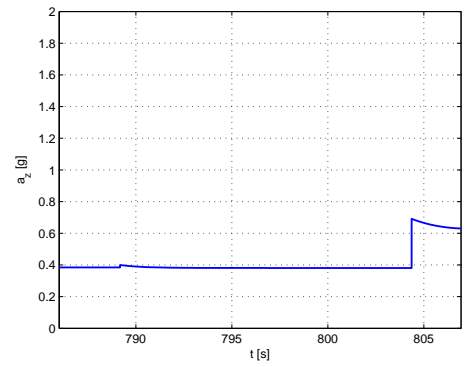
(a) x-direction.



(b) z-direction.



(c) x-direction.



(d) z-direction.

Figure 6.34: Acceleration in body axis.

Chapter 7

Conclusions and future developments

Science is fun. Science is curiosity. We all have natural curiosity. Science is a process of investigating. It's posing questions and coming up with a method. It's delving in.

Sally Ride
STS Astronaut

This chapter reviews the questions addressed by the present project of thesis, recalling all the principal aspects of the research work. The achievements of the proposed implementation are exposed, without concealing its limitations. Only by critically analyzing the results it is possible to suggest future developments and research directions.

7.1 Conclusions

The aim of the project was the creation of an optimization tool that could help the preliminary design of the planetary EDL of a manned vehicle. In particular, the intention was to simultaneously optimize its configuration and trajectory, taking into account the presence of a crew.

To achieve this challenging objective, it was necessary to investigate three different topics: the human physiology, the modeling of the vehicle and its subsystems, the MDO.

First of all, the attention was concentrated on the definition of the requirements due to the presence of man. The resistance to acceleration was especially scrutinized, to address the problems associated with the high accel-

erations that are typically experienced during a planetary EDL. A second aspect that was treated is the need to provide the crew with sufficient habitable volume and with a pressurized environment. It was demonstrated that the presence of human beings aboard a vehicle affects both its atmospheric trajectory and its configuration. Although a complete design should also consider requirements on temperature, radiation, noise and vibration, we can state that the most critical issues related to the EDL phase were considered.

A second demanding activity was the creation of the complete model for the vehicle and for its trajectory. The design of an EDL vehicle is an extensively multidisciplinary subject. The creation of each disciplinary module was addressed adopting a simplifying approach, always guaranteeing the validity of the models. Following this *modus operandi*, it was possible to simulate the entire trajectory in the atmosphere, from the entry to the touchdown. Since the configuration of the system changes many times in the course of the descent, the trajectory was divided in sequential phases triggered by characteristic events. The system was thought as a single body; a change of configuration was denoted by a change in the mass or in the size and aerodynamic characteristics of the object. Although the simplification was conspicuous, the model proved itself sufficiently good to obtain satisfactory results. The main subsystems responsible for a successful landing were sized in first approximation. Parachutes deployment and structural integrity constraints were also defined. Even though it would have been preferable to implement a highly generic model, the impossibility to create a database for multiple OML shapes led the author to select an Apollo-derivative geometry for the capsule, for which aerodynamic database exist.

The construction of the integrated tool was performed in Matlab environment, which provides both the possibility to implement the desired models and some optimization capabilities. The implementation of the integrated framework was enabled by the analysis of the interdependencies among all the involved disciplines. The complexity of the model, comprehensive of the vehicle and its trajectory, caused the assembled optimization tool to be quite articulated. The design variables reflect the multidisciplinary of the problem. The objective of the optimization is to find solutions for which the total mass is as low as possible. The constraints defining the feasibility region of the search space are multiple and convey once again the multidisciplinary idea: the masses of the TPS and of the structure must be sufficient to withstand the thermal and dynamic loads, respectively; the experienced accelerations must be tolerable for human beings; the propellant must provide sufficient thrust for the final deceleration; the velocity at the touchdown must ensure a safe landing. Because of computational time considerations,

Brinkley's model could not be used and constraints on impact accelerations other than the landing were not taken into account. The complexity of the problem suggested that a global optimization method was necessary for the research of the solutions. After a review of the available global optimization methods, the PSO was selected. This algorithm offers good performance and is able to deal with highly nonlinear objective functions and constraints.

The performed optimizations have demonstrated the validity of the integrated tool and the possibility to obtain results in a reasonable amount of time. The implemented model is fairly complete, since it encompasses many of the subsystems, envisages the presence of a crew and considers all of the different configurations assumed by the vehicle during its descent; notwithstanding, some solutions for the coupled vehicle and trajectory design can be found in a few hours only. This capability could be exploited during the preliminary design phase of a manned exploration mission: it is in fact convenient to consider the implications of the presence of man from the very first phases of the design.

A difficulty was confronted in the first attempts to use the PSO algorithm to find optimum solutions. The PSO proved itself unable to initialize the swarm with feasible particles; unfortunately a badly initialized swarm fails to converge to an optimum solution. To overcome this issue, some swarms were initialized partially by hand; others were composed of a combination of particles selected among those found to be feasible by the previous simulations. Thanks to this process, the results of different optimizations could be obtained and compared.

The critical analysis of a complete simulation allowed the identification of another problem: the tendency of the PSO to search restricted regions of the design space, for some of the variables. By distinguishing the feasible and unfeasible particles, it was also possible to have an idea of their distribution. In spite of these difficulties and imperfections, it was demonstrated that some first guess solutions can be obtained without much computational effort. The designed solutions consider the three aspects that we wanted to study: the vehicle, its trajectory and the presence of a crew.

7.2 Future developments

Some suggestions for future developments derive from the analysis of the limitations of the present study.

Further investigation is needed to guarantee a better search of the design space. As already said, a good initialization of the swarm is important for

the success of the optimization. Processes other than that used for this project could enhance the quality of the particles distribution and ease the algorithm convergence.

In order to increase the general validity of the tool, other deceleration strategies (splashdown, airbags, inflatable decelerators) could be introduced in the model; a wider database of parachutes, TPS materials and capsule geometries could also work in this direction. It would be interesting to study the possibility to control the bank angle during the descent, instead of keeping it fixed as in this project; this degree of freedom could enable convenient trajectories and ease the loads experienced by the astronauts.

Some methods should be found to impose constraints on the tolerance to the transient accelerations caused by the parachutes deployment; the integration of any dynamic equations should be avoided to contain the computational effort. Constraints on rotations should also be imposed if the bank and attitude angles are allowed to vary in time.

As it was already mentioned, the minimum mass is not the only significant objective in the optimization of EDL vehicles and trajectories. One may think of optimizing for the landing precision, if a certain point on the surface is targeted. The presence of the astronauts also suggests to minimize the effect of impact accelerations. A particularly interesting subject of investigation could be the combination of these objectives.

Acronyms

CAD	Computer-Aided Design
CEV	Crew Exploration Vehicle
CFD	Computational Fluid Dynamics
CM	Command Module
CNES	Centre National d'Études Spatiales
CNS	Central Nervous System
DNA	Deoxyribonucleic Acid
DSM	Design Structure Matrix
DSMC	Direct Simulation Monte Carlo
ECLS	Environmental Control and Life Support
ECLSS	Environmental Control and Life Support System
EDL	Entry Descent and Landing
ESA	European Space Agency
ESAS	Exploration Systems Architecture Study
ETH	Eidgenössische Technische Hochschule
EVA	Extra-Vehicular Activity
FEM	Finite Element Method
GA	Genetic Algorithm
GCR	Galactic Cosmic Ray
G-LOC	Gravity-induced Loss Of Consciousness
GTO	Geostationary Transfer Orbits
HIDH	Human Integration Design Handbook
ISS	International Space Station

JPL Jet Propulsion Laboratory
LAURA Langley Aerothermodynamic Upwind Relaxation Algorithm
LCG Liquid Cooling Garment
LEO Low Earth Orbits
MDO Multidisciplinary Optimization
MER Mars Exploration Rover
MPF Mars Pathfinder
MSIS Man-Systems Integration Standards
NASA National Aeronautics and Space Administration
NHV Net Habitable Volume
NLP Nonlinear Programming
ODE Ordinary Differential Equation
OML Outer Mold Line
PESST Planetary Entry System Synthesis Tool
PICA Phenolic Impregnated Carbon Ablator
PIDO Process Integration and Design Optimization
PSO Particle Swarm Optimization
QSL Quasi-Static Load
RBE Relative Biological Effectiveness
RCS Reaction Control System
SA Simulated Annealing
SFHSS Space Flight Human System Standard
SM Service Module
SPE Solar Particle Event
TPS Thermal Protection System
ULA United Launch Alliance

Bibliography

- [1] George W. Bush. The Vision for Space Exploration. National Aeronautics and Space Administration, February 2004.
- [2] Charles F. Jr. Bolden. Fiscal Year 2012 Budget Estimates. National Aeronautics and Space Administration.
- [3] Developments of ACTS in 2006. http://www.russianspaceweb.com/soyuz_acts.html.
- [4] NASA. *Space Shuttle Technical Conference*, volume Part 1, Houston, Texas, June 1983.
- [5] Martin Bayer. Hermes: learning from our mistakes. *Space Policy*, 11(3), August 1995.
- [6] HL-20 Model for Personnel Launch System Research: A Lifting-Body Concept. <http://www.nasa.gov/centers/langley/news/factsheets/HL-20.html>.
- [7] X-38 Fact Sheet. <http://www.nasa.gov/centers/dryden/news/FactSheets/FS-038-DFRC.html>.
- [8] Joshua E. Johnson, Ryan P. Starkey, and Mark J. Lewis. Aerodynamic Stability of Reentry Heat Shield Shapes for a Crew Exploration Vehicle. *Journal of Spacecrafts and Rockets*, 43(4), July-August 2006.
- [9] Jamshid A. Samareh. A Multidisciplinary Tool for Systems Analysis of Planetary Entry, Descent, and Landing (SAPE). Technical report, NASA Langley Research Center, Hampton, Virginia, November 2009.
- [10] Brad Johns, Kwok Fan, Tara Tveten, Loreyna Young, Neil Cheatwood, and Garry Qualls. Framework for Analysis and Collaborative Engineering (FACE). In *40th Aerospace Sciences Meeting and Exhibit*, Reno, Nevada, January 2002.

- [11] Gary A. Jr Allen, Peter J. Gage, Ethiraj Venkatapathy, David R. Olynick, and Paul F. Wercinski. A Web-based Analysis System for Planetary Entry Vehicle Design. In *7th AIAA/USAF/NASA/ISSMO Symposium on Multidisciplinary Analysis and Optimization*, September 1998.
- [12] Periklis Papadopoulos and Prabhakar Subrahmanyam. Web-Based Computational Investigation of Aerothermodynamics of Atmospheric Entry Vehicles. *Journal of Spacecraft and Rockets*, 43(6), November-December 2006.
- [13] Richard E. Otero and Robert D. Braun. The Planetary Entry Systems Synthesis Tool: A Conceptual Design and Analysis Tool for EDL Systems. In *IEEE Aerospace Conference Proceedings*, 2010.
- [14] Kristina Alemany, Grant Wells, John Theisinger, Ian Claik, and Robert Braun. Mars entry, descent, and landing parametric sizing and design space visualization trades. In *Collection of Technical Papers - AIAA/AAS Astrodynamics Specialist Conference*, 2006.
- [15] Cristina Parigini, Michèle Lavagna, and Roberto Armellin. Ottimizzazione Multidisciplinare di Veicoli Atmosferici per le Fasi in Ingresso, Discesa e Landing, 2005/2006.
- [16] Roberto Armellin, Michèle Lavagna, Ryan P. Starkey, and Mark J. Lewis. Aerogravity-Assist Maneuvers: Coupled Trajectory and Vehicle Shape Optimization. *Journal of Spacecrafts and Rockets*, 44(5), September-October 2007.
- [17] Francesco Castellini and Michèle Lavagna. Comparative Analysis of Global Techniques for Performance and Design Optimization of Launchers. *Journal of Spacecraft and Rockets*, 49(2):274–285, March-April 2012.
- [18] Robert D. Braun, Arlene A. Moore, and Ilan M. Kroo. Collaborative Approach to Launch Vehicle Design. *Journal of Spacecraft and Rockets*, 34(4), July-August 1997.
- [19] Wiley J. Larson and Linda K. Pranke. *Human Spaceflight: Mission Analysis and Design*. McGraw-Hill Higher Education, 1999.
- [20] A. Pavy-Le Traon, M. Heer, M.V. Narici, J. Rittweger, and J. Vernikos. From space to Earth: advances in human physiology from 20 years of bed rest studies (1986-2006). *European Journal of Applied Physiology*, 101(2), July 2007.

- [21] Bedrest Studies. http://www.esa.int/Our_Activities/Human_Spaceflight/Bedrest_studies.
- [22] Bed Rest Studies. <https://bedreststudy.jsc.nasa.gov/>.
- [23] NASA. Man-Systems Integration Standards, Volume 1, Revision B, NASA-STD-3000-VOL-1-REV-B. Technical report, NASA Johnson Space Center, July 1995.
- [24] NASA. Human Integration Design Handbook (HIDH), NASA/SP-2010-3407. Technical report, NASA, January 2010.
- [25] NASA. Space Flight Human-System Standard, NASA-STD-3001-VOL-1. Technical report, NASA Johnson Space Center, May 2007.
- [26] Arnauld E. Nicogossian, Stanley R. Mohler, Oleg G. Gazenko, and Anatoliy I. Grigoriev. *Space Biology and Medicine*. AIAA and Nauka Press, 1996.
- [27] James W. Brinkley, Lawrence J. Specker, and Stephen E. Mosher. Development of acceleration exposure limits for advanced escape systems. In *AGARD, Implications of Advanced Technologies for Air and Spacecraft Escape 14 p(SEE N 90-20054 13-03)*, 1990.
- [28] Marc M. Cohen. Testing the Celentano Curve: An Empirical Survey of Predictions for Human Spacecraft Pressurized Volume. In *38th International Conference on Environmental Systems*, San Francisco, California, 2008.
- [29] Marianne Rudisill, Robert Howard, Brand Griffin, Jennifer Green, Larry Toups, and Kriss Kennedy. Lunar Architecture Team - Phase 2 Habitat Volume Estimation: “Caution When Using Analogs”. In *ASCE Earth and Space Conference*, Long Beach, California, 2008.
- [30] Arnauld E. Nicogossian, Caroline Leach Huntoon, and Sam L. Pool. *Space Physiology and Medicine*. Lea and Febiger, third edition edition, 1993.
- [31] Enno Brinckmann. *Biology in Space and Life on Earth: Effects of Space-flight on Biological Systems*. Wiley-VCH, 2007.
- [32] Paul O. Wieland. Living Together in Space: The Design and Operation of the Life Support Systems on the International. Technical report, NASA Marshall Space Flight Center, January 1998.

- [33] Sondra A. Perez, John B. Charles, William G. Fortner, Victor IV Hurst, and Janice V. Meck. Cardiovascular Effects of Anti-G Suit and Cooling Garment During Space Shuttle Re-entry and Landing. *Aviation, Space, and Environmental Medicine*, 74(7), 2003.
- [34] Nguyen X. Vinh and Robert D. Culp. *Hypersonic and Planetary Entry Flight Mechanics*. The University of Michigan Press, 1980.
- [35] David A. Spencer, Robert C. Blanchard, Robert D. Braun, Pieter H. Kallemeyn, and Sam W. Thurman. Mars Pathfinder Entry, Descent, and Landing Reconstruction. *Journal of Spacecraft and Rockets*, 36(3), May-June 1999.
- [36] Carl G. Justus and Robert D. Braun. Atmospheric Environments for Entry, Descent and Landing (EDL). Technical report, NASA Marshall Space Flight Center, June 2007.
- [37] NASA Earth Fact Sheet. <http://nssdc.gsfc.nasa.gov/planetary/factsheet/earthfact.html>.
- [38] NASA Mars Fact Sheet. <http://nssdc.gsfc.nasa.gov/planetary/factsheet/marsfact.html>.
- [39] Doug Stanley, Steve Cook, and John Connolly. NASA's Exploration Systems Architecture Study - Final Report, NASA-TM-2005-214062. Technical report, NASA, November 2005.
- [40] *Ariane 5 User's Manual*, issue 5, revision 1 edition, July 2011.
- [41] *Soyuz User's Manual*, issue 2, revision 0 edition, March 2012.
- [42] *VEGA User's Manual*, issue 3, revision 0 edition, March 2006.
- [43] Robert D. Braun, Robert A. Mitcheltree, and F. McNeil Cheatwood. Mars Microprobe Entry Analysis. In *Proceedings of the IEEE Aerospace Conference*, 1997.
- [44] William C. Jr. Moseley, Ralph E. Graham, and Jack E. Hughes. Aerodynamic Stability Characteristics of the Apollo Command Module. Technical report, NASA Manned Spacecraft Center, Houston, Texas, August 1968.
- [45] Giorgio Guglieri. Introduction to parachute subsonic aerodynamics. Notes for a conference in the Aerodynamics course by Professor Bof-fadossi, Politecnico di Milano.

- [46] Anita Sengupta, Rob Sinclair, and Ricardo Machin. Ringsail Parachutes for Planetary Entry Applications. In *2011 IEEE Aerospace Conference*, Big Sky, Montana, 2011.
- [47] E. G. Ewing, H. W. Bixby, and T. W. Knacke. Recovery Systems Design Guide. Technical report, IRVIN INDUSTRIES INC GARDENA CA, December 1978.
- [48] Theo W. Knacke. *Parachute Recovery Systems Design Manual*. Para Publishing, 1992.
- [49] Kenneth E. French. A New Correlation of Parachute Weight Data. *Journal of Spacecrafts and Rockets*, 8(1), January 1971.
- [50] Kenneth Sutton and Randolph A. Graves. A General Stagnation-Point Convective-Heating Equation for Arbitrary Gas Mixtures. Technical report, NASA Langley Research Center, Hampton, Virginia, 1971.
- [51] John A. Dec and Robert D. Braun. An Approximate Ablative Thermal Protection System Sizing Tool for Entry System Design. In *44th AIAA Aerospace Sciences Meeting and Exhibit*, Reno, Nevada, 2006.
- [52] Michael E. Tauber and Kenneth Sutton. Stagnation-Point Radiative Heating Relations for Earth and Mars Entries. *Journal of Spacecraft and Rockets*, 28(1):40–42, January 1991.
- [53] S. D. Williams and Donald M. Curry. Thermal Protection Materials: Thermophysical Property Data. Technical report, NASA, December 1992.
- [54] TPSX Materials Properties Database. <http://tpsx.arc.nasa.gov>.
- [55] William L. Ko, Leslie Gong, and Robert D. Quinn. Reentry Thermal Analysis of a Generic Crew Exploration Vehicle Structure. Technical report, NASA Dryden Flight Research Center, Edwards, California, May 2007.
- [56] Wiley J. Larson and James R. Wertz. *Space Mission Analysis and Design*. Microcosm Press and Kluwer Academic Publishers, 1992.
- [57] Joshua A. St Vaughn, Gurkupal Singh, Ravi Prakash, Robert H. Freisbee, James M. Corliss, and Robin D. Tutterow. Design of a Retro Rocket Earth Landing System for the Orion Spacecraft. In *Aerospace Conference, 2007 IEEE*, 2007.

- [58] *Delta II Payload Planners Guide*, December 2006.
- [59] Jaroslaw Sobieszczanski-Sobieski and Raphael T. Haftka. Multidisciplinary aerospace design optimization: Survey of recent developments. *Structural Optimization*, 14(1), August 1997.
- [60] Natalia M. Alexandrov. Editorial - Multidisciplinary design optimization. *Optimization and Engineering*, 34(4), March 2005.
- [61] Jeremy Agte, Olivier De Weck, Jaroslaw Sobieszczanski-Sobieski, Paul Arendsen, Alan Morris, and Martin Spieck. MDO: Assessment and direction for advancement - an opinion of one international group. *Multidisciplinary Optimization*, 40(1-6), January 2010.
- [62] OpenMDAO: An open-source MDAO framework written in Python. <http://openmdao.org>.
- [63] Lluís Soler, Ahmad Khatiby, and Kenneth D. Mease. Mars Entry Trajectory Planning for Higher Elevation Landing. *Advances in the Astronautical Sciences*, 148.
- [64] Global Optimization Toolbox. <http://www.mathworks.it/it/help/gads/index.html>.
- [65] Scott Kirkpatrick, C. D. Jr. Gelatt, and Mario P. Vecchi. Optimization by Simulated Annealing. *Science*, 220(4598), 1983.
- [66] Marco Locatelli. Simulated Annealing Algorithms for Global Optimization. In Panos M. Pardalos and Romeijn Edwin H., editors, *Handbook of Global Optimization*, volume 2, pages 179–229. Kluwer Academic Publishers, 2002.
- [67] John H. Holland. Genetic Algorithms. *Scientific American*, 267(1):66–72, July 1992.
- [68] James Kennedy and Russell Eberhart. Particle Swarm Optimization. In *IEEE International Conference on Neural Networks - Conference Proceedings, v 4*, 1995.
- [69] Russell C. Eberhart and Yuhui Shi. Comparison between Genetic Algorithms and Particle Swarm Optimization. *Lecture Notes in Computer Science*, 1447, 1998.

- [70] Soren Ebbesen, Pascal Kiwitez, and Lino Guzzella. A Generic Particle Swarm Optimization Matlab Function. In *2012 American Control Conference*, Montréal, Canada, June 2012.
- [71] A generic particle swarm optimization function for Matlab. <http://www.idsc.ethz.ch/Downloads/ps0/index>.